JOINT PHD THESIS

Salford University -Royaume Uni
Institute for Materials Research
School of Computing, Science and Engineering

Université de Poitiers - France
(Faculté des Sciences Fondamentales et Appliquées)
(Diplôme National - Arrêté du 7 août 2006)
Ecole Doctorale : Sciences pour l'Ingénieur et Appliquée
Secteur de Recherche : Milieux denses, matériaux et composants

Présentée par

Amy Sarah GANDY

A transmission electron microscopy study of the interaction between defects in amorphous silicon and a moving crystalline/amorphous interface

Supervisors: **Stephen E. Donnelly**
Marie-France Beaufort

****

Submitted in partial fulfilment of the Requirements for the degree of
Doctor of Philosophy

19 December 2008

JURY

Jaap Van Den BERG	Professor, Salford University, UK	Reporter
Esidor NTSOENZOK	Professeur, Université d'Orléans, F	Reporter
Andrew BLELOCH	Reader, Liverpool University, UK	Examiner
Marie-Laure DAVID	Maître de Conférences, Université de Poitiers, F	Examiner
Stephen E. DONNELLY	Professor, Salford University, Manchester, UK	Supervisor
Marie-France BEAUFORT	DR - CNRS, Université de Poitiers, F	Supervisor

Contents

List of Figure vii

List of Tables x

Acknowledgments xi

Declaration xiii

Abbreviations xiv

Abstract xv

Résumé xvi

Publications xvii

1. Introduction 2

1.1 History 2

1.2 Motivation 7

1.3 References 9

2. Literature Review 11

2.1 Introduction 12

2.2 Ion implantation 14

2.2.1 The interatomic potential 16

2.2.2 Ion stopping 17

2.2.3 Nuclear stopping 17

2.2.4 Electronic stopping 19

2.2.5 Ion Ranges **19**
2.2.6 Channelling **21**
2.2.7 Radiation damage **21**
2.2.8 Displacement spike **22**
2.2.9 Thermal spike **23**
2.2.10 Computer simulations **23**
2.3 Radiation Damage **24**
2.3.1 Overview **24**
2.4 Defects **25**
2.4.1 Vacancies **28**
2.4.2 Vacancy clusters **29**
2.4.3 Interstitials **30**
2.4.4 I-V pair **33**
2.4.5 Dynamical Annealing **34**
2.5 Ion beam induced amorphisation of Si **35**
2.5.1 Amorphous Si **35**
2.5.2 Defect accumulation in c-Si **38**
2.5.3 Models of amorphisation **39**
2.5.3.1 Homogenous amorphisation **39**
2.5.3.2 Heterogeneous amorphisation **41**
2.5.3.3 Nucleation limited model **43**
2.5.3.4 The I-V pair **44**
2.6 Secondary interstitial-type defects **45**
2.6.1 Ostwald Ripening **49**
2.6.2 {113} rod-like and ribbon like defects **50**
2.6.3 Dislocation loops **51**
2.7 Noble gas implantation **52**
2.7.1 Bubble formation in Si **54**
2.7.2 The effects of implantation and annealing temperature **56**
2.8 Solid Phase Re-growth of a-Si **58**
2.8.1 Substrate orientation dependence **60**
2.8.2 Impurity dependence **61**

2.9 Models of SPEG 67
2.10 References 75

3. Experimental Techniques 85
3.1 Introduction 86
3.2 Specimen production 88
3.3 TEM Specimen Preparation Methods 90
3.3.1 Bulk Sample Cutting 91
3.3.2 Cross-sectional Sample preparation 91
3.3.3 Mechanical Polishing 92
3.3.4 Final Thinning of Specimens 94
3.3.5 Ion beam milling (IBM) techniques 94
3.3.6 The Effects of IBM Techniques on Vacancy-Type Defects in Silicon 96
3.3.7 The Small Angle Cleavage Technique (SACT) 99
3.4 The Transmission Electron Microscope 102
3.4.1 The Illumination System 104
3.4.1.1 The electron gun 104
3.4.1.2 Electron sources 104
3.4.1.3 TEM Lenses 106
3.4.1.3.1 Spherical Aberration 108
3.4.1.3.2 Chromatic aberration 108
3.4.1.3.3 Astigmatism 108
3.4.1.4 Condenser Lenses and aperture 109
3.4.1.5 Moving and tilting the beam 109
3.4.1.6 Alignment 110
3.4.2 The Objective Lens 110
3.4.3 The Imaging System 111
3.5 Transmission Electron Microscopy 112
3.5.1 Electron Interactions 113
3.5.1.1 Elastic Scattering 114
3.5.1.2 Inelastic Scattering 115
3.5.2 Electron Diffraction 115

3.5.2.1 Real Diffraction patterns 120
3.5.3 TEM Image production 124
3.5.3.1 Amplitude Contrast 125
3.5.3.1.1 Mass-thickness contrast 125
3.5.3.1.2 Z Contrast 126
3.5.3.2 Diffraction Contrast 126
3.5.3.2.1 Weak Beam Dark-Field (WBDF) images 127
3.5.4 Phase Contrast 128
3.5.4.1 Moiré Fringes 128
3.5.4.2 Fresnel Contrast 129
3.5.4.3 High Resolution TEM (HRTEM) 129
3.5.5 *In-situ* experiments 130
3.6 Image analysis 131
3.7 References 132

4. Characterisation of Xe implantation damage in Si 134
4.1 Introduction 135
4.2 Experimental procedure 136
4.3 Results 138
4.3.1 Room temperature implantation 138
4.3.2 High temperature implantation 138
5 x 1015 Xe ions/cm2 (as-implanted) 140
5 x 1015 Xe ions/cm2 (800°C) 140
1 x 10^{16} Xe ions/cm^2 (as-implanted) 142
1 x 1016 Xe ions/cm2 (600°C anneal) 143
1 x 1016 Xe ions/cm2 (800°C anneal) 144
1 x 1016 Xe ions/cm2 (as-implanted) 145
1 x 1016 Xe ions/cm2 (800°C anneal) 146
2 x 1016 Xe ions/cm2(as-implanted) 150
2 x 1016 Xe ions/cm2 (800°C anneal) 151
5 x 1016 Xe ions/cm2(as-implanted) 153

5 x 1016 Xe ions/cm2 (600°C anneal) 155
5 x 1016 Xe ions/cm2 (800°C anneal) 156
5 x 1016 Xe ions/cm2(as-implanted) 157
5 x 1016 Xe ions/cm2(800°C anneal) 158
Summary of results 161
4.4 Discussion 164
4.5 Conclusion 168
4.6 References 169

5. SPEG of He implanted buried amorphous layers in Si 170
5.1 Introduction 171
5.2 Results 172
5.2.1 Li implantation 172
5.2.1.1 Experiment 172
5.2.1.2 As-implanted Results 173
5.2.1.3 Results after annealing 174
5.2.2 He implantation 175
5.2.2.1 Experiment 176
5.2.2.2 Results 176
5.2.2.3 Results after annealing 177
5.2.3 Discussion 178
5.2.4 Re-crystallisation without the influence of excess interstitials 182
5.2.4.1 Experiment 183
5.2.4.1 Results 183
5.2.5 In-situ investigations 184
5.2.5.1 *In-situ* XTEM experiment 1 – re-crystallisation of a buried a-layer 185
5.2.5.2 *In-situ* XTEM experiment 2 – bubble mobility,sweeping of gas by the c/a interfaces and microtwin nucleation during SPEG 187

5.2.5.3 Bubble mobility 187
5.2.5.4 Microtwin Formation 187
5.2.5.5 Sweeping of bubbles by the a/c Interfaces 192
5.2.6 Conclusion 194
5.3 References 196

6. Summary and Conclusions 198
6.1 Summary 199
6.1.1 Characterisation of Xe Implantation damage in Si 199
6.1.2 SPEG of He implanted buried amorphous layers in Si 200
6.2 Conclusions 201
6.3 Further Work 202

List of Figures

Figure 1.1: *Image comparing the vacuum tube and the transistor* 3
Figure 1.2: *Schematic of a p-n junction, also known as a diode* 4
Figure 1.3: *Schematic showing the Smart-Cut© process of producing…* 6
Figure 2.1: *Diagram illustrating the differences between…* 15
Figure 2.2: *The interatomic potential-energy function…* 16
Figure 2.3: *Elastic collision between two hard spheres of radius* r_o*…* 19
Figure 2.4: *The line* R *describes the actual path traversed…* 20
Figure 2.5: *Light ion implantation into silicon…* 21
Figure 2.6: *Diagram showing intrinsic and extrinsic point defects…* 28
Figure 2.7: *Diagram depicting the thermal stability of…* 30
Figure 2.8: *Diagram showing theoretical interstitial positions in Si…* 31
Figure 2.9*: Diagram showing the thermal stability of various…* 32
Figure 2.10: Proposed a*tomic structure of the I-V pair…* 34
Figure 2.11: *Diagram showing the results from computer simulations...* 36
Figure 2.12: *Diagram showing the heterogeneous model…* 43
Figure 2.13: *Schematics depicting the classification system as…* 47
Figure 2.14: *Diagram depicting the secondary defects…* 48
Figure 2.15: *Computational representation of the atomic structure…* 51
Figure 2.16: *Schematic describing the motions of the c/a interfaces…* 58
Figure 2.17: *Graph illustrating the temperature dependence…* 60
Figure 2.18: *Graph illustrating difference in a-layer re-growth rates…* 61
Figure 2.19: *Graph illustrating the re-growth rate dependence…* 63
Figure 2.20: *Diagram illustrating the typical a-layer re-growth…* 64
Figure 2.21: *Diagram illustrating the microtwin nucleation model…* 67
Figure 2.22: *Diagram taken from Drosd and Washburn illustrating…* 68
Figure 2.23: *Diagram taken from Csepregi illustrating that…* 70
Figure 2.24: *Diagram, illustrating the a-symmetric nature of…* 71
Figure 2.25: *Diagram illustrating SPEG via the movement of kinks…* 72
Figure 2.26: *Simulation showing the possible mechanisms by which…* 74
Figure 3.1: *Diagram showing the simple method employed…* 92
Figure 3.2: *Picture of 2 tripod polishers…* 93

Figure 3.3: *Schematic, taken from [1] showing the basic principle…* 95
Figure 3.4: *A composite picture of three TEM micrographs depicting…* 98
Figure 3.5: *Schematic depicting the SACT method…* 100
Figure 3.6: *Schematic diagram showing the basic components…* 103
Figure 3.7: *Diagram of a typical electron gun. Electrons are produced…* 105
Figure 3.8: *Ray diagram for a finite object, indicative of what occurs…* 107
Figure 3.9: *Diagram showing the different types of scattering…* 114
Figure 3.10: *Diffraction pattern produced from (001) Si…* 116
Figure 3.11: *Diagram showing a plane wave incident on two parallel…* 117
Figure 3.12: *This diagram shows electron beam diffraction off a plane…* 118
Figure 3.13: *This diagram shows parallel planes of atoms orientated…* 120
Figure 3.14: *The diffraction patterns indicative of the three lowest…* 121
Figure 3.15: *Construction of the reciprocal lattice and the Ewald…* 122
Figure 3.16: *A diffraction pattern taken from a defected area of…* 123
Figure 3.17: *Diffraction pattern taken from amorphous Si.* 124
Figure 3.18: *Diagram illustrating how planes of atoms surrounding…* 128
Figure 3.19: *A WBDF image showing the Moiré fringes produced…* 129
Figure 3.20: *HRTEM micrograph of microtwin lamellae in a…* 130
Figure 4.1: *[110] cross-section, bright field TEM micrograph…* 138
Figure 4.2: *Graph showing results of TRIM calculations for 250keV…* 139
Figure 4.3: *[110] cross-section, bright field TEM micrograph…* 140
Figure 4.4: *Bright field TEM images and corresponding schematics…* 142
Figure 4.5: *[110] cross-section, bright field TEM micrograph…* 143
Figure 4.6: *[110] cross-section, 2-beam, TEM micrograph of the …* 144
Figure 4.7 *[110] cross-section, bright-field TEM micrograph…* 145
Figure 4.8: *[110] cross-section, bright-field TEM micrograph…* 146
Figure 4.9: *[110] cross-section, bright-field TEM micrograph…* 147
Figure 4.10: *[110] cross-section, WBDF TEM micrographs…* 148
Figure 4.11: *2-beam using [-111] TEM micrograph…* 148
Figure 4.12: *Z- contrast images of the above sample. The light…* 149
Figure 4.13: *High resolution TEM image showing the…* 150
Figure 4.14: *[110] cross-section, bright-field TEM micrographs…* 151
Figure 4.15: *[110] cross-section, bright-field TEM micrographs…* 151

Figure 4.16: *Bright-field TEM images and corresponding schematics…* 152
Figure 4.17: *[110] cross-section, bright field TEM micrograph…* 154
Figure 4.18: *[110] cross-section, bright field TEM micrograph…* 154
Figure 4.19: *[110] cross-section, bright field TEM micrograph…* 155
Figure 4.20: *[110] cross-section, bright field TEM micrograph…* 156
Figure 4.21: *[110] cross-section, bright field TEM micrograph…* 156
Figure 4.22: *[110] cross-section, bright field TEM micrograph…* 157
Figure 4.23: *[110] cross-section, low magnification TEM micrograph…* 158
Figure 4.24: *[110] cross-section, TEM micrograph of the damaged…* 159
Figure 4.25: *The left hand image is a WBDF image, produced…* 159
Figure 4.26: *Schematic showing the defect morphologies produced…* 163
Figure 4.27: *Scanning electron microscope (SEM) images…* 165
Figure 5.1: *[011] cross-section, bright field TEM micrograph…* 173
Figure 5.2: *[110] cross-section, bright field TEM micrograph…* 174
Figure 5.3: *[110] cross-section, bright field TEM micrograph…* 175
Figure 5.4: *[110] cross-section, bright field TEM image…* 176
Figure 5.5: *Bright field TEM images of bubbles…* 177
Figure 5.6: *[110] cross-section, bright field TEM…* 177
Figure 5.7: *[110] cross-section, dark field TEM micrograph…* 178
Figure 5.8: *[110] cross-section, TEM images…* 179
Figure 5.9: *Results from TRIM calculations of 80Kev He…* 180
Figure 5.10: *(a) is a [110] cross-section, bright field TEM…* 182
Figure 5.11: *All images are [110] cross-sections…* 184
Figure 5.12: *[110] bright field image of sample…* 186
Figure 5.13: *6 screen shots, taken 200 seconds apart…* 188
Figure 5.14: *High-resolution phase contrast image of microtwins…* 189
Figure 5.15: *Ball-stick representation, projected on (110)…* 191
Figure 5.16: *3 screen shots taken 70 seconds apart…* 192
Figure 5.17: *Screen shots clearly showing bubble mobility in the …* 193

List of Tables

Table 1.1: *This table gives the complete implantation, annealing…* 89
Table 4.1: *Summary of results obtained from TEM images…* 161
Table 4.2: *Summary of results obtained from TEM images…* 161
Table 4.3: *Summary of results obtained from TEM images…* 161

Acknowledgments

There are so many people that I would like to thank for their help and support. Firstly I would like to thank both of my supervisors, Professor Steve Donnelly and Dr Marie-France Beaufort, for their continued encouragement and support throughout my PhD. I would especially like to thank Marie for all the guidance she gave me whilst I was living in France and for making my time away from home a thoroughly enjoyable one. And to Steve, thank you so much for believing in me, especially during this final year.

I would like to thank Dr. Jacques Chevalier, Scientific Counsellor at the French Embassy in London, both for his assistance in establishing the "Joint Doctorate Programme" at Salford and for the support that he provided to me during my extended visits to Poitiers.

I would also like to thank everyone else who helped, and looked after, me during my visit to the Laboratoire de Métallurgie Physique in Poitiers, France.

I would like to thank Kerry, Jon, Phil, Graeme and Simon for making the last few years in the office and lab such educational fun. An extra special thank you goes to Jon for saving me on the numerous occasions when the computer and I fell out.

Thank you to Neil, for being my best friend who never stopped trying to make me believe in myself.

To Katy and Kate, who have been amazing friends and supportive through-out, no matter how stressed out I was with them. You both kept me sane.

Thank you to mum, dad, Lorna and Grandma Vera.

Thank you to Andy for putting up with me through thick and thin, and never giving up on me. I love you to pieces.

And finally to Grandma Margery. You never doubted me and you never stopped encouraging me. I will always love you.

Declaration

The research described in this thesis is the work of the author with the following exceptions. High resolution transmission electron microscopy and Z contrast imaging were carried out by D. Eyidi. Video capture of bubble mobility, as detailed in Figure 5.17, was carried out by S. E. Donnelly. Conventional transmission electron microscopy was performed by M F Beaufort on samples shown in Figure 5.11. All implantations were carried out either at the Laboratoire de Métallurgie Physique, Poitiers, or at the Universidade Federai do Rio Grande do Sul (UFRGS) in Brazil.

Abbreviations

Central processing unit (CPU)

Integrated circuit (IC)

Silicon-on-insulator (SOI)

Separation by implantation of oxygen (SIMOX)

Transmission Electron Microscopy (TEM)

Rutherford Backscattering spectroscopy (RBS)

Crystalline/amorphous (c/a)

Electron paramagnetic resonance (EPR),

Positron annihilation spectroscopy (PAS)

Transient enhanced diffusion (TED)

Deep level transient spectroscopy (DLTS)

Local vibrational mode spectroscopy (LVM)

Solid phase epitaxial re-growth (SPEG)

Threshold damage density (TDD)

Room temperature (RT)

Liquid Nitrogen temperature (LN_2)

Cross Sectional Transmission Electron Microscopy (XTEM)

Ion beam milling (IBM)

Precision Ion Polishing System (PIPS)

Duo Mill (DM)

Scanning Electron Microscope (SEM)

Small Angle Cleavage Technique (SACT)

Electron Energy Loss Spectroscopy (EELS)

Universidade Federai do Rio Grande do Sul (UFRGS)

Selected Area Diffraction (SAD)

Abstract

Transmission electron microscopy (TEM) has been used to investigate the damage produced following high temperature (350˚C) Xe implantation into (100) Si at fluence (>1x10^{16} Xe ions/cm^2) and energy (250keV) which produce a buried amorphous layer; and the defect structures produced following thermal anneals of 400˚C, 600˚C or 800˚C for 30 minutes. Analysis of these samples yielded results which suggested that the Xe gas contained within the amorphous layers was swept by the amorphous/crystalline interfaces during solid phase epitaxial re-crystallisation (SPEG) into large bubbles elongated along a direction perpendicular to the interfaces. In order to further investigate this sweeping effect, buried amorphous layers were produced in Si by implanting Li at liquid nitrogen temperature and post implanting the layers with 1x10^{16} He ions/cm^2. Contrary to the spherical bubbles produced under similar conditions in crystalline Si, irregular shaped bubbles were formed in the amorphous layer. Results from *in-situ* TEM studies showed that these bubbles are mobile at temperatures lower than expected in crystalline Si. Thus, upon reaching the moving interfaces between amorphous and crystalline Si, the bubbles are forced back into the amorphous material which ultimately results in coalescence of the gas into larger bubbles once the two interfaces combine. In addition, microtwins have been shown to form in regions of the re-crystallising layer where there exists an excess of interstitial-type defects. This is contrary to previous microtwin nucleation models which suggested that microtwins are either formed on [111] planes or on bubbles.

Résumé

L'endommagement induit par implantation de xénon dans le silicium a été étudié par microscopie électronique à transmission (MET). Les implantations réalisées à 350°C, à une énergie de 250keV et pour des fluences supérieures à >1x10^{16} Xe ions/cm^2 conduisent à la formation d'une couche amorphe enterrée. Les observations effectuées sur les échantillons recuits montrent la présence d`une rangée de grandes cavités allongées dans la direction perpendiculaire à l'interface. Ceci suggère que, lors de la recristallisation du silicium, le déplacement simultané des deux interfaces entraîne le déplacement du gaz jusqu' à son confinement dans de larges bulles. Afin de mieux appréhender les mécanismes qui conduisent au mouvement des bulles, de l'hélium à faible dose a été implanté dans du silicium préalablement amorphisé par implantation de Li à basse température. L'implantation d'hélium dans le silicium amorphe conduit à la formation de bulles de forme irrégulière. Ce résultat diffère du silicium cristallin où des bulles sphériques sont obtenues pour des conditions d'implantation identiques. Les expériences réalisées '*in situ*' dans le MET montrent clairement d'une part que les bulles sont poussées par l'interface, et d'autre part la nucléation de micromacles. Il a été mis en évidence au cours de cette étude que les bulles sont mobiles à plus basse température dans le silicium amorphe que dans la phase cristalline. Lors de la recristallisation, les bulles se trouvent alors confinées dans le matériau amorphe, ce qui cadiut à leur coalescence et à la formation de larges bulles une fois que les deux fronts de recristallisation se sont rejoints. De plus, il a été établi que la formation de micromacles dans la région recristallisée est liée à un excès de défauts de type interstitiels dans la zone amorphe. Ce résultat est contraire aux modèles de la littérature qui suggèrent que les micromacles se forment soit sur des plans {111} soit sur les bulles.

Mots clés : Silicium, implantation, amorphisation, recristallisation, bulles, micromacles, xénon, hélium, MET.

Publications

1. Beaufort, M. F., Pizzagalli, L., Gandy, A. S., Oliviero, E., Eyidi, D., and Donnelly S. E. *Solid-phase epitaxial regrowth of amorphous silicon containing helium bubbles* J. Appl. Phys. **104** (2008) 094905

2. Gandy. A.S., Donnelly, S.E., Beaufort, M.F, Oliviero, E., Fichtner P.F.P. *The interaction of cavities in silicon with moving amorphous–crystalline interfaces* Nuclear Instruments and Methods in Physics Research Section B: Beam Interactions with Materials and Atoms, **257**, Issues 1-2, April (2007), Pages 177-180

Chapter 1

Introduction

1. Introduction

1.1 History

Almost all modern electronic devices, such as computers, televisions, mobile telephones and cars, etc, contain a number of integrated circuits. These integrated circuits consist of various electrical components, including transistors, resistors, capacitors and diodes, on a semiconductor substrate. Different combinations and numbers of these components result in the production of different circuits to carry out different functions. The integrated circuit in a computer is called a microprocessor. Also known as a central processing unit (CPU), the microprocessor consists of a number of transistors and it processes the information in a computer allowing it to perform complex functions.

A transistor can be thought of as a switch as it can be used to turn a current on or off. It can also be used to amplify current. Before the invention of the transistor vacuum tubes were used to amplify or switch a current. A simple vacuum tube consists of a filament under vacuum inside a glass tube. Also inside the tube is a metal plate which is positively charged relative to the filament. When a current is passed through the filament it heats up until a process known as thermionic emission occurs (see Section 3.4.1.2). At this point electrons are released into the tube and are attracted to the positive plate. This arrangement is known as a diode as the current is only ever conducted in one direction; from the plate to the filament. Vacuum tubes are power in-efficient due to the amount of heat lost through the tube required for thermionic emission. Transistors are much smaller, more efficient and reliable, and much cheaper to make than vacuum tubes.

Figure 1.1: *Image comparing the vacuum tube and the transistor [1]*

The first transistor based circuit boards contained only a few transistors as discrete elements. Figure 1.1 shows a transistor as a discrete element. Due to their size and the fact that they had to be individually wired to each other, limitations on the number of transistors that could be used in a circuit were quickly realised. This limitation was overcome by the invention of the integrated circuit, where many transistors were produced at the same time on the same board using semiconductor material. Modern-day IC's contain several billion transistors due to the continued miniaturization of transistors.

Doped Si is used as the substrate for the majority of integrated circuits. Si is a group IV element with a face-centred cubic crystallographic structure. It has a lattice spacing of 5.43Å and each atom has four nearest neighbours. Intrinsic Si is a very poor conductor; however, by doping it with either group III or V elements, Si can conduct up to very high temperatures. Phosphorus, a group V element, has 5 electrons in its outer shell. Doping using phosphorus results in the introduction of extra valence electrons which move under an electric field. This type of compound is called an n-type semiconductor and the phosphorus is called a donor as it donates electrons to the semiconductor. Conversely to this situation, doping Si with group III elements, such as boron, results in broken bonds called "holes" existing in

the semiconductor. These "holes" can be thought of as moving under the application of an electrical field. In fact it is the movement of electrons combining with the broken bonds which creates the impression of "hole" mobility. Boron in known as an accepter element and the combination of this and Si is called a p-type semiconductor.

Transistors are produced using a combination of both p-type and n-type semiconductors. A diode can be produced by combing n-type and p-type Si as shown in Figure 1.2.

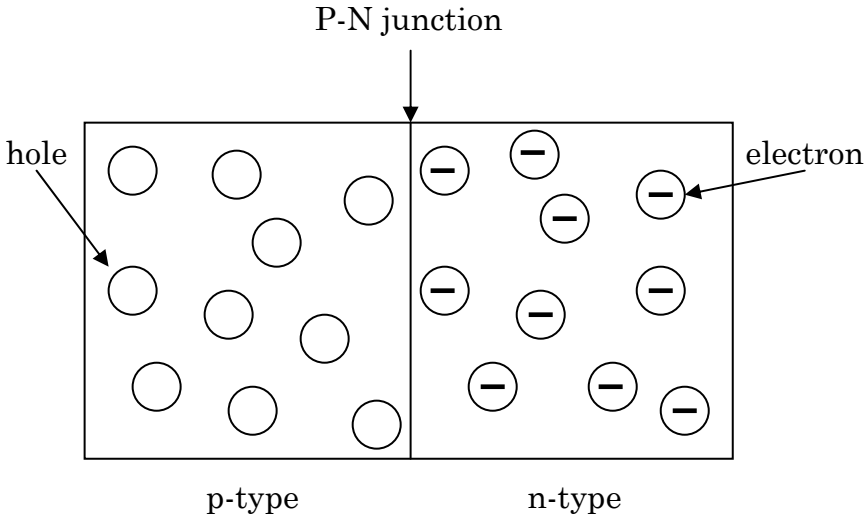

Figure 1.2: *Schematic of a p-n junction, also known as a diode.*

As with the simple vacuum tube, this structure only allows current to flow in one direction, if an electric field is applied in a direction which results in the holes and electrons combining at the P-N junction. Transistors used in integrated circuits are generally produced by sandwiching a p-type semiconductor between two layers of n-type semiconductor material.

The increase in the number of transistors can be described by Moore's Law, which states that the number of transistors used in IC's increases exponentially by doubling approximately every two years[2]. The miniaturisation of transistors is advantageous in that the cost per unit area and switching power consumption decreases, and the memory capacity,

processing speed and resolution of digital cameras increases, to name a few. However there are disadvantages to miniaturisation such as current leakage. Silicon-on-insulator (SOI) structures are in development in order to minimise this loss and aid further miniaturisation[3]. These structures isolate the silicon junction using an electrical insulator. The Separation by implantation of oxygen (SIMOX)[4] [5] process uses implantation of oxygen and high temperature annealing to produce a buried silicon dioxide (SiO_2) layer. The Smart-cut© [3] method utilises hydrogen implantation, wafer binding and exfoliation to produce SOI structures. Figure 1.3 illustrates this method.

A Si wafer is oxidised to produce an oxide layer of defined thickness. Hydrogen ions are implanted into the Si wafer through the oxide layer. Ion implantation allows the H to be implanted a precise distance from the surface and with a specific fluence of H ions. Another Si wafer, known as the handling wafer, is bonded onto the oxide layer. The structure is then subject to a high temperature anneal. This causes the implanted hydrogen to form a band of bubbles. It also removes some of the radiation damaged caused by the implantation of H ions. The presence of the bubble layer allows the SOI structure to be removed from the rest of the initial Si wafer by exfoliation. This method produces a thin, well defined, piece of Si on an insulating base. Unfortunately, some of the defects produced during ion implantation remain even following the high temperature anneal, resulting in a decrease in performance of the semiconductor component. In addition, the surface of the exfoliated wafer is relatively uneven which requires an extra polishing stage im order to achieve the smoothness required for IC production.

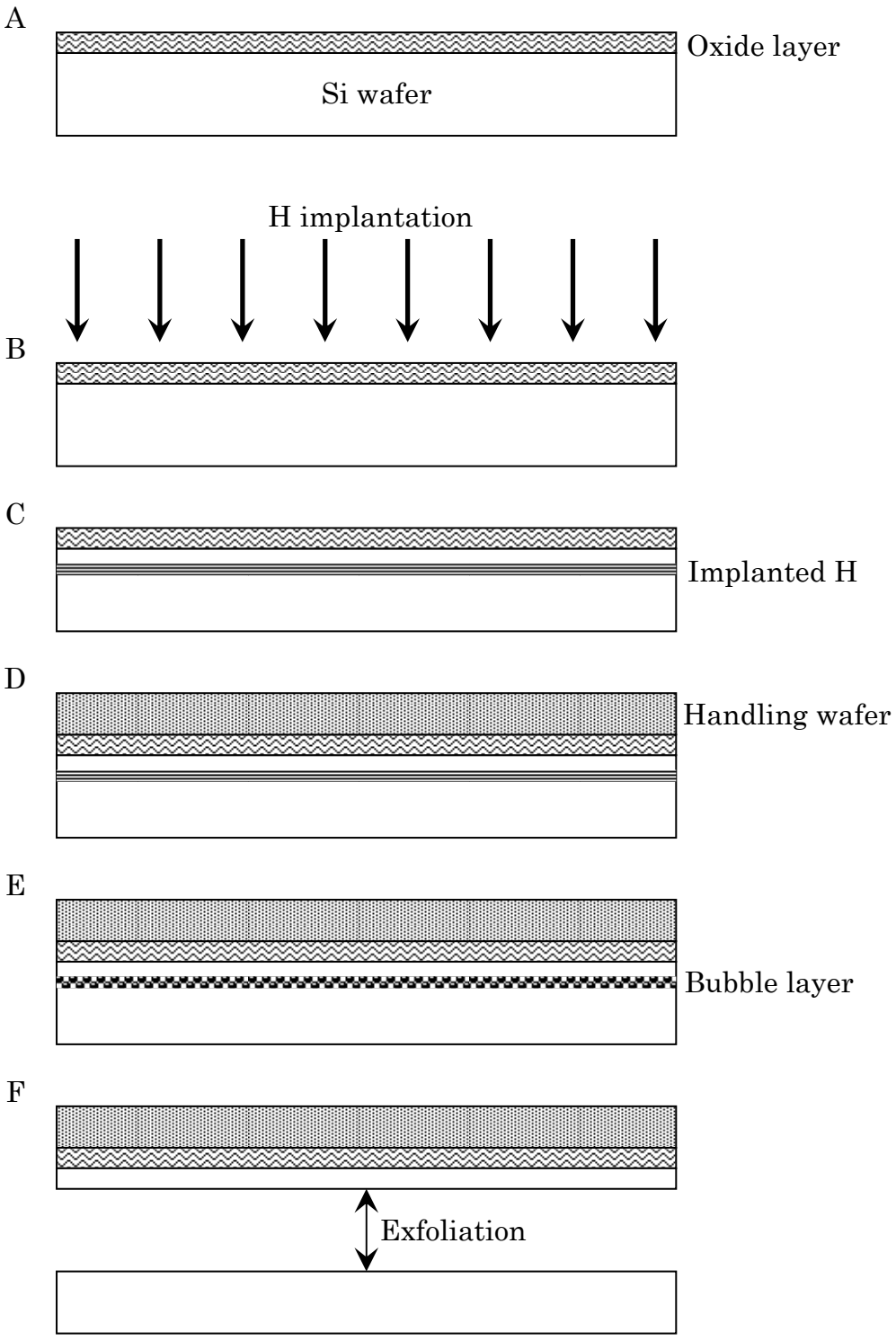

Fig 1.3: *Schematic showing the Smart-Cut© process of producing Silicon-on-insulator structures.*

In order for Moore's Law to be followed, and miniaturisation of IC's and transistors to continue, development of these SIO structures is necessary. The initial aim of this study was to produce a technique which minimised residual defect concentration and surface roughness of the exfoliated wafer.

1.2 Motivation

He in Si has been extensively studied. Cavities in Si, which are created following He implantation and annealing, have been found to be excellent sinks for mobile interstitials during annealing [6]. These cavities have been found to trap metal impurities and, if implanted near to the active region of an integrated circuit, reduce the impurity concentration in that area. This process is known as proximity gettering [7-10].

Other noble gas implantations into Si have also been investigated, although not as extensively as He in Si. Transmission Electron Microscopy (TEM) studies have been carried out on Ne implanted Si [11]. A recent study of Ne implantation into crystalline Si at high temperatures has found that a buried amorphous layer containing Ne is produced [12]. Xe implantation in Si has received less attention. In order to gain a further fundamental understanding of defect processes following inert-gas implantation, Chapter 4 of this thesis details an investigation into high temperature (350˚C) Xe implantation, carried out using TEM.

TEM also allows for specific defects to be investigated *in-situ* during experimentation. Results of previous work [13] suggested that, during thermal annealing of pre-damaged Si by He implantation, the moving interface between the amorphous and crystalline phases swept He bubbles and vacancies giving rise to the formation of large cavities. Following this research it was envisaged that the re-crystallisation of a buried amorphous layer containing gas might give rise to a discrete linear band of small bubbles due to this "sweeping" process. It was proposed that this process could be developed into a novel process for the production of SOI structures.

It was found during this study that Xe implanted into crystalline Si at high temperatures results in a Xe gas filled buried amorphous layer. It was envisaged that re-crystallisation of this layer may produce a similar effect to that reported in [13], and thus could be used in the production of SOI structure production. However, it was found that following re-crystallisation of the layer, the required structure for SOI was not produced as a large number of defects remained in the sample following re-crystallisation. However the experiments yielded interesting results about defect production following high temperature implantation of Xe into crystalline Si and subsequent recovery of the resultant amorphous layer by thermal annealing.

Research using Rutherford Backscattering spectroscopy techniques [14] indicated that a buried amorphous layer can be produced in Si by implanting Li ions at liquid nitrogen temperature. The results suggested that the interfaces between the crystalline and amorphous phases were relatively sharp. He was implanted into this layer as the distribution of this gas is well known and definable, therefore it was possible to produce a band of bubbles in the centre of the layer. The results of the re-crystallisation of this layer are detailed in Chapter 5. Once again, the necessary structure for SOI was not produced. However, results leading to further fundamental understanding of defect production and evolution were obtained, specifically the production of microtwins. Further, the "sweeping" effect of bubbles by the moving crystalline/amorphous (c/a) interfaces was investigated in more detail using *in-situ* TEM.

1.3 References

1. http://nobelprize.org/educational_games/physics/integrated_circuit/history Accessed October 2008
2. Moore, G.E. IEEE Technical Diges, 1975. **11**.
3. Bruel. M, Electronics Letters 31 (1995) 1201
4. Feng, X.-Q. and Huang, Y. *Mechanics of Smart-Cut® technology*. International Journal of Solids and Structures, 2004. **41**(16-17): p.4299.
5. Yankov, R.A., Kaschny, J.R., Fichtner, P.F.P., Mucklich, A., Kreiig, U., and Skorupa, W. *Impurity gettering effects in separation-by-implanted-oxygen (SIMOX) wafers: what getters what, where and how*. Microelectronic Engineering, 1997. **36**(1-4): p.129-132.
6. Williams, J.S., Ridgway, M.C., Conway, M.J., Wong-Leung, J., Zhu, X.F., Petravic, M., Fortuna, F., Ruault, M.O., Bernas, H., Kinomura, A., Nakano, Y., and Hayashi, Y. *Interaction of defects and metals with nanocavities in silicon*. Nuclear Instruments & Methods in Physics Research Section B-Beam Interactions with Materials and Atoms, 2001. **362**: p.33-43.
7. Donnelly, S.E., Vishnyakov, V.M., Carter, G., Terry, J., Haworth, L.I., Sermanni, P., and Birtcher, R.C. *The use of cavities for gettering in silicon microelectronic devices*. Nuclear Instruments and Methods in Physics Research Section B: Beam Interactions with Materials and Atoms, 2003. **206**: p.422-426.
8. Raineri, V., Battaglia, A., and Rimini, E. *Gettering of Metals by He Induced Voids in Silicon*. Nuclear Instruments & Methods in Physics Research Section B-Beam Interactions with Materials and Atoms, 1995. **96**(1-2): p.249-252.
9. Petersen, G.A., Myers, S.M., and Follstaedt, D.M. *Gettering of transition metals by cavities in silicon formed by helium ion implantation*. Nuclear Instruments & Methods in Physics Research

Section B-Beam Interactions with Materials and Atoms, 1997. **127**: p.301-306.

10. Raineri, V., Fallica, P.G., Percolla, G., Battaglia, A., Barbagallo, M., and Campisano, S.U. *Gettering of Metals by Voids in Silicon.* Journal of Applied Physics, 1995. **78**(6): p.3727-3735.
11. Oliviero, E., Peripolli, S., Fichtner, P.F.P., and Amaral, L. *Characterization of neon implantation damage in silicon.* Materials Science and Engineering B, 2004. **112**(2-3): p.111-115.
12. Oliviero, E., Peripolli, S., Amaral, L., Fichtner, P.F.P., Neaufort, M.F., FJ.F Barbot, and Donnelly, S.E. *Damage accumulation in neon implanted silicon.* Journal of Applied Physics, 2006. **043505**.
13. Vishnyakov, V.M., Donnelly, S.E., and Carter, G. *The influence of impurities on the growth of helium-induced cavities in silicon.* Journal of Applied Physics, 2003: p.238.
14. Oliviero, E., *Personal Communication*. 2005.

Chapter 2

Literature Review

2.1 Introduction

The primary focus of this study is the investigation of radiation induced damage formed in Si by ion implantation, and its evolution during thermal annealing. Implantation of ions into Si at sufficient energies results in displacement of the Si atoms and damage to the single crystal structure. Depending on the ion species, the temperature of the substrate, and the fluence and energy of the ions, this damage can manifest itself in many ways. A relatively low fluence implantation for a given ion species (for example, for He at room temperature about $1x10^{15}$ He ions/cm^2) results in small clusters of point defects being produced, where the size and density of the clusters increases with increasing fluence. For a given energy, temperature and ion species, there exists a *threshold fluence* where the amount of damage produced is so large that the crystalline silicon (c-Si) becomes amorphous. Increasing the ion fluence results in an increase in the width of the a-layer, as well as an increase in defect size and density. Heating of the sample post-implantation may impart sufficient energy to these defects so that they become mobile. These mobile defects can interact with other defects and combine to either annihilate or form different defects. This type of defect interaction and coalescence is of major interest in the current work, specifically between the defects in an a-layer and those situated at the interface between the layer and the remaining single crystal. Samples that have only been implanted are termed *as-implanted* samples, and those that have been subjected to a post-implantation thermal treatment are called *annealed* samples.

Many processes occur during ion implantation and thermal annealing. This chapter discusses these processes and describes the defects that are consequently produced, initially looking at general defect production in all materials. As all the implantation experiments carried out in this study were performed in Si, much of the discussion is specific to this material. Section 2.2 concentrates on the physics of ion implantation and the processes which lead to the formation of defects. Sections 2.4, 2.6 and 2.7 describe the defects which are produced via low fluence (sub-amorphising) implantation and their evolution into other defects during thermal annealing. Special consideration is given to the effects of implanting Si with the noble gases, as He and Xe were implanted into Si throughout the course

of this study. Section 2.5 is concerned with the production of amorphous silicon (a-Si). Section 2.8 describes the possible processes involved in the re-crystallisation of a-layers which occur during thermal annealing, as well as the defects produced as a consequence of the re-crystallisation of these layers.

2.2 Ion implantation

Ion implantation is a means of introducing impurities into materials. It is extensively used in the doping of semiconductors, but an unavoidable consequence of this process is the production of lattice defects known as *radiation damage*. This damage occurs when an implanted ion interacts with a lattice atom and displaces it from its position, resulting in a vacant lattice site and the atom residing at some other position in the material. The displaced atom is called an *interstitial* and the vacant site is known as a *vacancy,* and together they are described as a Frenkel pair. Most Frenkel pairs annihilate during implantation. Sufficient heating of the material post-implantation may result in the recombination of these defects and restoration of the lattice. For a dopant to be electrically active in the material it must reside on a lattice site (i.e. be substitutional). Thermal annealing post-implantation may therefore lead not only to the recovery of the damaged lattice, but also to the activation of the dopant ions.

Due to the continued miniaturization of microprocessor circuit elements, it is essential that the concentration of dopants being introduced and their position in the material is known and is precisely controllable. Several techniques have been developed for the introduction of foreign ions into a material, but none achieves the specific controllability required for commercial use better than ion implantation. Fig 2.1 is a schematic describing ion implantation and diffusion (an alternative doping method). In the diffusion method, the sample is heated in a gas comprising the dopants. Under such conditions the gas diffuses from the region of high concentration and though the surface of the sample where the concentration of dopants is low. Diffusion of dopants through the sample in this way also results in lateral diffusion of the dopants, as is illustrated in Figure 2.1.

In ion implantation, the dopant atoms are ionised and accelerated in an electric field. A magnetic field is used to accurately select ions of the required species which are then directed onto the surface of the sample. The ions collide with the atoms in the sample producing lattice damage. The final resting place of the ions

can be accurately predicted for a given ion species with known implantation energy.

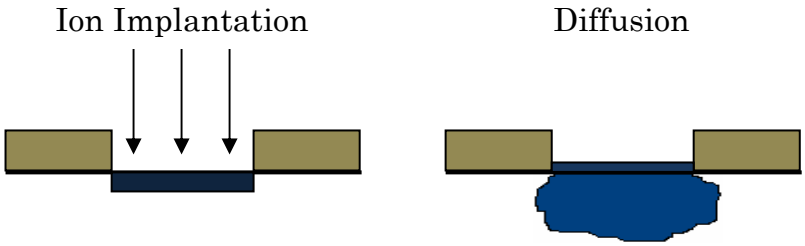

Figure 2.1: *Diagram illustrating the differences between ion implantation and diffusion techniques in their controllability of implanted ion profiles. Ion implantation gives a better means of ion introduction to accurate depths.*

The production of defects during implantation may result in a modification of the diffusivity of the dopant ions. For instance, they may give rise to a broadening of the spatial distribution of B in Si resulting from the diffusion of Si interstitials (Transient Enhanced Diffusion) [1]. This and other effects resulting from ion implantation can be explained if one has an understanding of the mechanisms of defect production and interaction during ion implantation, and subsequent annealing. The following section describes the basic physical processes involved during ion implantation and the mechanisms of ion stopping which govern damage production.

2.2.1 The interatomic potential

In a solid, whether crystalline or amorphous, there exists an equilibrium position for the atoms such that there are no net forces acting on the atoms and the potential energy of the system is at a minimum. Under these conditions the distance between nearest neighbour atoms, known as the equilibrium interatomic distance, is of the order of 10^{-8} cm [2]. It is convenient to use a potential-energy function $V(r)$, when explaining interactions between atoms, electrons or ions as it describes the forces between particles as a function of distance. Fig 2.2 gives an example of an interatomic potential function where the minimum of the potential-well corresponds to the equilibrium interatomic distance $r = r_0$.

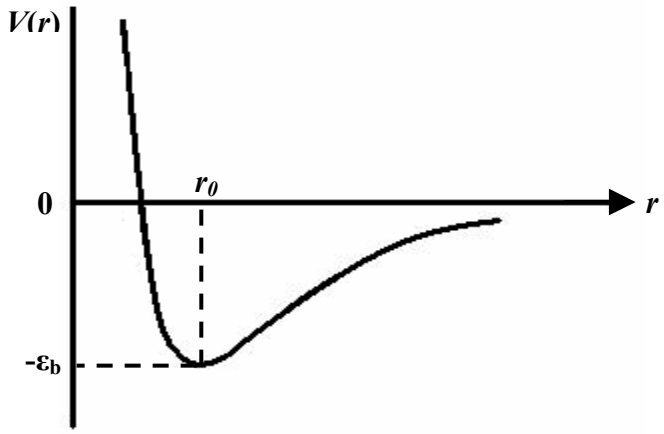

Figure 2.2: *The interatomic potential-energy function. The equilibrium interatomic distance r_0 corresponds to the minimum potential energy $-\varepsilon_b$ of the system. Energy is required to displace the atom from the bottom of the potential well.*

The shape of the potential-well is determined by the type of bonding between the atoms, and the energy binding the atoms together E_b is related to the depth of the well at r_0. Above -273°C all atoms vibrate about their equilibrium position with a thermal energy proportional to $k_B T$ where k_B is Boltzmann's constant [2]. An increase in temperature results in an increase in the atoms' vibrational amplitude which, due to the asymmetrical nature of the potential-well, causes the atoms to move apart. At a certain temperature the atoms will posses

sufficient energy to move out of the potential well and diffuse through the lattice. This process occurs during thermal annealing of the implanted material.

2.2.2 Ion stopping

During implantation, ions collide with atoms with energies well in excess of those required for thermal diffusion, and at distances less than the equilibrium interatomic separation r_0. The way in which energy is transferred from the incident ion to the atom determines the damage produced, and the rate of energy-loss determines the distance that the ions ultimately travel. If energy is transferred from the incident ion to electrons then the result will be the promotion of the electrons to a higher energy state or even ionization of the atom. This process is called electronic stopping. This type of interaction (although the atom is not displaced from its position) is known as an inelastic collision. An ion can also impart its energy to the atom as a whole. If sufficient energy is transferred then the atom can be displaced from its position. These types of collisions are elastic and the process is known as nuclear stopping and results in damage production. In general, for heavy and light ions at low energies nuclear stopping dominates. However for light ions (e.g. H, He) travelling in the keV to MeV energy range, electronic stopping is the predominant stopping mechanism. For the energies used in the experiments reported in this thesis, nuclear stopping dominates.

2.2.3 Nuclear stopping

Nuclear stopping may result in sufficient amounts of energy being transferred to the atom so that it is displaced from its position and the trajectory of the ion is significantly altered. The following describes a simple but useful model by which to describe such collisions.

Energetic ions interact with the atoms in the solid through forces which are described by an interatomic potential. Consider two atoms with atomic numbers Z_1 and Z_2 separated by a distance r. If the atoms interact at distances of less than the Bohr radius a_0 = 0.053nm [2] then the collision can be thought of as being

between the two positive nuclei and is described by the Coulomb potential such that:

$$V(r) = \frac{Z_1 Z_2 e^2}{r} \qquad [2.1]$$

When $a_0 < r \leq r_0$ then the nuclei are screened by the electrons in the inner shells, and collisions at these distances are described by the screened Coulomb potential:

$$V(r) = \frac{Z_1 Z_2 e^2}{r} \chi(r) \qquad [2.2]$$

Where $\chi(r)$ is the screening function which acts to reduce the potential. Ions with energies in the keV to MeV range experience collisions at these distances [2].

A simple interatomic potential is one where is it assumed that $V(r)$ is infinite from $r = 0$ to $r = r_0$ and then falls as a step function to zero at $r > r_0$. This allows for simplifications to be made such that the atom can be thought of as a hard sphere of radius r_0, and that the collision is totally elastic whereby kinetic energy and momentum are conserved. This simplification, as described in Fig 2.3 from Carter and Grant (page 14) [1], only holds for near head on collisions. However it is useful in calculating energies and velocities of the atom and ion as well as the range of scattering angles possible during the collision event, but in general more realistic potentials are used.

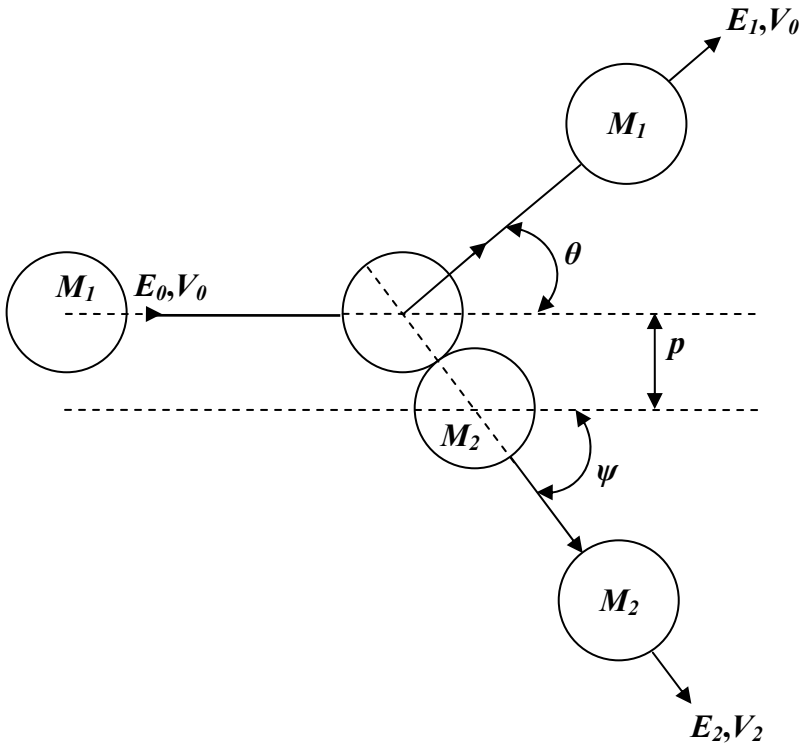

Figure 2.3: *Elastic collision between two hard spheres of radius r_o. Sphere of mass M_1 which initially has energy E_0 and velocity v_0, collides with sphere of mass M_2 which is initially at rest. As energy is conserved, after the collision M_1 has energy E_1 and M_2 has energy E_2, the sum of which equates to E_0. P is the perpendicular distance between the initial direction of motion of the incident ion and the parallel line through the initial position of the centre of the struck atom, known as the impact parameter [1].*

2.2.4 Electronic stopping

Unlike nuclear stopping, loss of the ions' energy to the atomic electrons does not result in a significant alteration in its trajectory. This inelastic energy loss generally dominates for light ions such as He. The majority of radiation damage occurs at the end-of-range of an ions' trajectory where its energy has decreased such that nuclear stopping dominates.

2.2.5 Ion Ranges

As the ion travels through the material it undergoes as series of collisions with the atoms in the material until it comes to rest. Atoms which have been displaced

by the incident ion are called primary knock-ons [2]. As nuclear stopping of the ion during a single collision event will generally result in a dramatic alteration in the ion's trajectory, after many collisions the ion will have travelled along a convoluted path determined by the outcome of each collision. The path length between collisions decreases as does the ion's energy. The overall distance travelled by the ion is measured as a vector parallel to the ion's initial trajectory and is called the projected ion range R', shown in Fig 2.4. During the implantation process many ions with the same mass and initial energy and will undergo numerous collisions which, as the parameter of each collision varies, will result in different projected ranges for each ion. For light ions such as He, the overall ion distribution tends to a Gaussian distribution whereas implantation with heavier ions such as Xe results in a skewed distribution. The most probable projected ion range, corresponding to the peaks of these curves, is called the mean projected ion range R_p. The range of the ion depends on the energy and atomic number of the ion as well as the atomic number of the substrate.

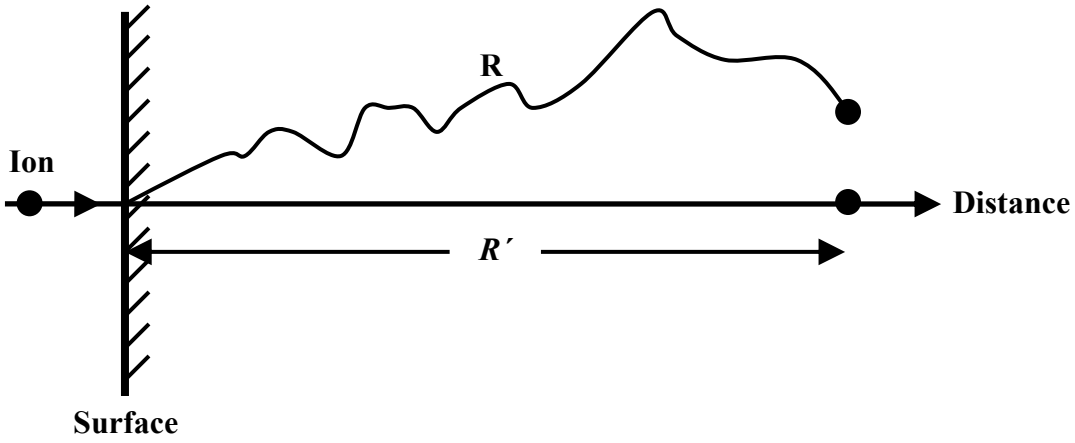

Figure 2.4: *The line* R *describes the actual path traversed by an ion in a solid. The projected range R' is denoted by the line parallel to the incident ion's trajectory.*

The mass of the incident ion is instrumental in determining the type of damage produced around its path. Nuclear stopping dominates for heavy ions throughout the entirety of the ions passage. In the energy range of interest here (up to 100's of keV) electronic stopping is the dominant process when implanting with light ions and so atomic displacements are unlikely until the ion's velocity has reached

one where nuclear stopping becomes more dominant. This results in a long ion track with minimal damage surrounding it, until at the end-of-range of the ion where atomic displacements take place. This is illustrated for a Si substrate in Fig 2.5 taken from Gibbons [3].

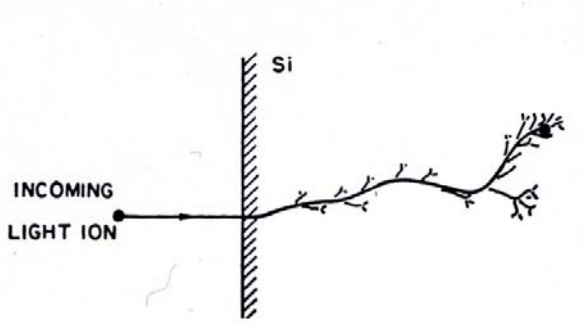

Figure 2.5: *Light ion implantation into silicon. The majority of atomic displacements only occur at the end-of-range of the ions path where nuclear stopping dominates [4].*

2.2.6 Channelling

Throughout this section, the descriptions of ion and atomic trajectories have been made on the assumption that the material is an amorphous solid. Commonly used Monte-Carlo type computer simulations, which accurately determine the range of ions in solids, have been produced by assuming that the material is amorphous. However, with crystalline materials there exist orientations of the substrate where the atoms are aligned in rows resulting in channels free of atoms. An energetic ion directed down such a channel is less likely to undergo collisions with the atomic nuclei. The ion experiences a repulsion due to the screened coulomb fields, steering it back into the centre of the channel [2]. This is known as channelling and it results in ranges longer than those calculated in Monte-Carlo models. To avoid channelling in Si during implantation, ions are incident on the surface of crystalline samples at an angle of about 7° from a major crystallographic direction.

2.2.7 Radiation damage

Radiation damage is the result of atoms being displaced from their lattice positions by implanted ions and energetic recoils. The energy required to displace an atom is called the displacement energy E_d. If the energy transferred to the

atom during the collision is less than E_d then the atom will not be displaced but will vibrate with increased amplitude about its lattice position. If the energy imparted is greater than E_d then the atom will be knocked off its site and travel through the lattice. The result of this displacement is a Frenkel pair defect which as previously stated, consists of a vacancy and an interstitial atom. In Si, the amount of energy required to create a Frenkel pair is 15-20eV [4]. If the primary knock-ons possess enough energy they themselves may displace other atoms from their lattice positions, which in turn may do the same to other atoms. This process is known as a collision cascade. A single ion may cause numerous collision cascades which are situated around the path of the ion. These collision cascades can be broken down into sequential two-body collisions. For a primary knock-on to displace another atom, the ion must transfer at least $2E_d$ to the initial target atom. If the primary knock-on imparts energy between E_d and $2E_d$ to another atom then, although this atom will be displaced, the primary knock-on does not have enough energy for another displacement. This atom will then occupy the vacant site and its excess kinetic energy be dissipated as heat. This entire process is known as a replacement collision. Following transfer of energy in elastic collisions, E, Kinchin and Pease [5] showed that:

$$N_d = 0.42\frac{E}{E_d} \qquad [2.3]$$

Where N_d is the number of atoms displaced into interstitial sites and so N_d vacancies have also been produced. The constant 0.42 takes account of the electronic energy loss which occurs during implantation.

2.2.8 Displacement spike

The distance between defect producing collisions is known as the mean free path λ_d. For heavy ion collisions, as the ion slows down more primary knock-ons are produced until a point where one is produced at every lattice site that the ion has traversed. This results in a highly damaged region where the centre, corresponding to the ion or primary knock-on path, consists of a high concentration of vacancies. The atoms from inside this area have been displaced

into interstitial positions surrounding the vacancy core. The entire damages region is known as a *displacement spike* and was suggested by Brinkman in 1956 [6].

2.2.9 Thermal spike

At the end of a displacement spike, all the atoms and ions will have insufficient energy to produce further displacements. The excess kinetic energy is then in the form of lattice vibrations resulting in localized heating. At some point during this process, the range of energies may be describable using a Maxwell-Boltzmann distribution function and the heating of the disordered region may be sufficient to cause melting [7]. This is known as a thermal spike, and it can last up to a few picoseconds [2].

2.2.10 Computer simulations

Computer simulations have been developed which can accurately calculate the amount of damage produced, the range of the ions and knock-on atoms, and the amount of energy imparted to the material per unit volume during ion implantation. As previously mentioned, these calculations assume that the implanted material is amorphous. For use throughout this study the TRIM [8] computer simulation package was used. TRIM uses statistical algorithms to calculate the numerous collisions which occur during ion implantation, and presents the results either as tables of values which can be used for post simulation quantitative analysis, or as distribution graphs which can be viewed as the simulation is running. Collision calculations performed using TRIM use a screened Coulomb potential and take into account exchange and correlation interaction between the overlapping electron shells [8]. The substrate material and thickness, and the ion species and energy can all be easily altered making TRIM an extremely powerful technique for the prediction of the stopping distances of ions in solids.

2.3 Radiation Damage

This section discusses the types of damage produced in Si as a consequence of keV ion implantation.

2.3.1 Overview

Section 2.2 described the basic processes involved in the production of radiation damage due to the implantation of energetic ions into solids. A collision cascade was described during which lattice atoms are displaced from their sites producing Frenkel defects (a vacancy and an interstitial). The quantity of vacancies and interstitials produced is determined by the mass and energy of the ion, where heavier ions (Xe compared to He) or slower ions (He towards the end of the ion track) result in an increase in damage. For heavy ions in silicon, it is generally believed that each collision cascade results in an amorphous volume [4] although this has recently been disputed with some authors reporting that these volumes are, in the main, highly damaged sub-amorphous regions [9]. As the fluence of the implanted ion is increased, so are the numbers of these damaged zones until a continuous amorphous layer is produced. For lighter ions where it is believed the purported amorphous zones are not created in a collision cascade [4], an overlapping of many cascades results in an increase in the density of the damage. At a critical fluence the damage density is so great that the crystalline material becomes amorphous. Both processes are described in more detail in Section 2.5.3.

Many factors affect the quantity and type of defects produced due to ion implantation. For example, substrate temperature and ion flux during implantation have an effect on damage formation through a process known as *dynamical annealing*, which is explained in Section 2.4.5.

After implantation an excess of interstitials generally exists in the material. This occurs when the implanted species occupies substitutional positions in the lattice. If after thermal annealing, all the vacancies produced have been filled by the implanted ions and displaced Si atoms, then a number of Si interstitials corresponding to the number of implanted ions will exist in the solid. This is known as the "+1" model, [10], and is the accepted model for low fluence

implantations of substitutional impurities into Si. Sufficient post-implantation thermal annealing of the material enables this Si excess to condense into small interstitial clusters which can grow into larger clusters by a process known as Ostwald ripening. This process is explained in Section 2.6.1. These larger clusters are generally more stable, requiring more energy in order to dissociate and form further *extended* defects such as {113} defects and dislocations. Therefore, a period of defect evolution can be envisaged in which defects migrate, grow and develop as a function of annealing time and temperature. The +1 model does not hold however when implanting Si with an inert gas, where significant numbers of vacancies remain locked into inert-gas/vacancy agglomerates or bubbles post-implantation. Both of these regimes, the subsequent thermal evolution into extended defects and descriptions of these extended defects are discussed below. Defects which are native to the material are known as *intrinsic defects*. For implanted materials, defects involving the implanted ion are termed *extrinsic defects*.

2.4 Defects

The following section describes the different types of defects which can be found in Si before and following ion implantation, and resulting from thermal annealing. Defects which constitute the as-implanted damage will be termed *primary defects* throughout this study and those created following thermal annealing are called *secondary defects*.

Vacancies and interstitials are known as *point defects*. Resolution limitations of the transmission electron microscope (TEM) (see Chapter 3) means that isolated vacancies, interstitials and small defect clusters containing a few tens of atoms cannot be imaged. Investigations into the nature of these defects have however been carried out using other techniques; mainly electron paramagnetic resonance (EPR), positron annihilation spectroscopy (PAS) and by using computational studies.

Point defects exist in un-implanted materials. Atoms in a solid in thermodynamic equilibrium occupy energetically favourable sites. Temperatures above absolute

zero cause the atoms to vibrate about these positions with a frequency, υ_0, of the order of 10^{13}Hz [11]. An increase in the temperature corresponds to greater oscillatory amplitudes until enough energy is imparted to the atom for it to escape its equilibrium position thus creating a vacancy. The atom can therefore be thought of as initially residing in a potential well of depth E_{vf}, where E_{vf} corresponds to the amount of energy required to produce a vacancy. For such an atom at any given finite temperature T, the frequency υ_f of its success in escaping the potential well is given by Maxwell-Boltmann statistics, such that:

$$\nu_f = \nu_0 \exp\frac{-E_{vf}}{kT} \qquad [2.4]$$

where k is Boltzmann's constant, and. If enough energy is supplied then the vacancy can migrate through the material. This occurs by way of a place exchange with a neighbouring atom, which requires energy to break the bonds of the atom with its neighbouring atom. Repetition of this process results in vacancy motion through-out the material. The rate of vacancy migration υ_m at a specific temperature is related to the energy required for migration E_{vm} by:

$$\nu_m = \nu_0 \exp\frac{-E_{vm}}{kT} \qquad [2.5]$$

The production of a vacancy causes the surrounding atoms to relax and their bonds to re-arrange in order to minimise the energy of the material. The introduction of an extra atom from the surface to a non-normal lattice position (the creation of an interstitial), produces considerable strain in the surrounding lattice and as a consequence much more thermal energy is required to form an interstitial from the surface than a vacancy. Because of this, there exists a higher concentration of vacancies than interstitials in intrinsic materials.

Diffusion of point defects in such a system can also be described in terms of concentration gradients, according to Fick's Laws [11]. If the atoms are distributed inhomogenously in a material, a concentration gradient will exist

causing the overall atomic motion in the direction of decreasing concentration. In ion-implanted materials, diffusion of the implanted species may be affected by the presence of point defects. As an example, a significant consequence of interstitial-type defects is the enhanced diffusion of dopants such as boron during post-implantation annealing, leading to a broadening of the dopants distribution. This is undesirable as it restricts further miniaturization of the lateral size of microprocessor components and is known as transient enhanced diffusion (TED)[1, 12, 13] It has been found that TED and the evolution and growth of interstitial-type defects during thermal annealing are related and will be explained in later sections.

The different types of point defects which are either native to the material (intrinsic) or created after implantation (extrinsic) are shown in Fig 2.6, taken from [14] (page 7). The removal of an atom results in a vacancy as shown in Fig 2.6a). The relaxation of the lattice surrounding the vacancy is necessary in order to minimise the energy of the system. A complex of two vacancies, called di-vacancy, is shown in Fig 2.6b). The simplest point defect associated with Si atoms is the self-interstitial which is situated on well-defined locations as shown in Fig 2.6c). The arrangement shown in Fig 2.6d) is termed an *intersticialcy*. It consists of two silicon atoms associated with the same lattice site. As with the di-vacancy, a di-interstitial has been identified, though is not shown in Fig 2.6. Figs 2.6e), f), g) and h) show extrinsic defects. Impurity atoms can reside in interstitial positions shown in Fig 2.6e). They can also take the form shown in Fig 2.6f). Here the impurity is in a *substitutional* position and is very important in semiconductors. In order for the dopant to be electrically active it must adopt such a position. Figs 2.6g) and h) show the vacancy-impurity and self-interstitial-impurity pairs respectively which are associated with the enhanced diffusion of impurities.

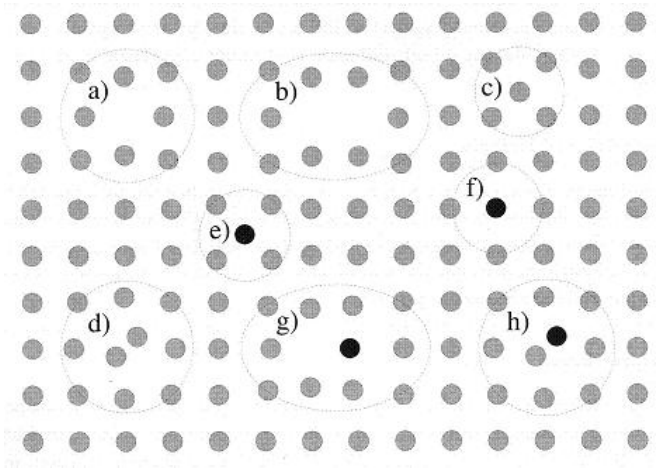

Figure 2.6: *Diagram showing intrinsic and extrinsic point defects in silicon; a) vacancy, b) di-vacancy, c) self-interstitial, d) interstitialcy, e) interstitial impurity, f) substitutional impurity, g) vacancy-impurity pair, h) self-interstitial-impurity pair [15].*

More specific information regarding the primary defects is given below.

2.4.1 Vacancies

It is known that a vacancy is created during energetic ion implantation when a lattice atom is displaced from its site and the vacancy and resultant interstitial do not recombine. Currently it is only possible to produce isolated vacancies and interstitials without creating more complex defects in Si via ~1-3MeV electron irradiation at cryogenic temperatures [15]. Comprehensive studies have been carried out by Watkins on the nature of the intrinsic point defects produced in this way using electron paramagnetic resonance (EPR) spectroscopy. Deep level transient spectroscopy (DLTS), which detects deep electronic energy levels in the Si band gap, positron annihilation spectroscopy (PAS) and local vibrational mode spectroscopy (LVM) have also been employed by other authors [15].

In Si, the removal of an atom results in 4 dangling bonds from the nearest-neighbour atoms residing in the vacancy. The vacancy can then either lose or gain charge carriers resulting in a reconstruction of the lattice around the vacancy. The way in which these dangling bonds rearrange themselves determines the charge state of the vacancy, which in turns affects the vacancy's

diffusivity and its interaction with other charged defects. EPR results have shown that the isolated vacancy in Si can exist with 5 different charge states (V^{2+}, V^{+}, V^{0}, V^{-}, V^{2-}), with the single positive (V^{+}) and single negative (V^{-}) charge states being observed immediately after electron irradiation at 4.2K [15]. Because of the charge states associated with isolated vacancies, electronic energy levels are introduced into the Si band gap. This can also occur due to the creation of isolated interstitials, vacancy-impurity pairs and self-interstitial-impurity pairs.

A vacancy is highly mobile, irrespective of its charge state. Watkins found that the monovacancy spectrum disappeared after a 15min isochronal anneal at ~70K in n-type Si and ~150K in p-type Si [15]. With the disappearance of these spectra came the simultaneous growth of new spectra associated with various defect-vacancy complexes. The activation energies for the migration of V^{0}, V^{2+} and V^{2-} in Si are given as 0.45, 0.32 and 0.18eV respectively [15] [16]. It is believed that V^{2+} and V^{2-} represent the dominant charge states in p-type and n-type Si respectively. As a consequence of the small migration energies, isolated vacancies are not likely to exist at room temperature.

2.4.2 Vacancy clusters

Vacancies can cluster together to form more stable defects. The di-vacancy, resulting from the combination of two vacancies (Fig 2.6(b)), is immobile at room temperature. At temperatures around 250°C [16] the di-vacancy starts to diffuse through Si, and dissociates at temperatures higher than 350°C [17]. Four charge states of the di-vacancy have been identified; $(VV)^{+}$, $(VV)^{0}$, $(VV)^{-}$ and $(VV)^{2-}$ [15]. Computer simulations [18] have shown that by increasing the number of vacancies in a cluster the stability of the defect is increased. At elevated temperatures these clusters may dissociate, becoming a source of vacancies for further interactions. The hexavacancy corresponds to a missing hexagonal ring of Si atoms. It is calculated to be the most stable configuration of the small vacancy clusters and has a calculated formation enthalpy of 1.9eV [16] but, to this authors knowledge, has yet to be experimentally identified.

As depicted in Fig 2.6(g), vacancies can combine with impurity atoms. Depending on the type of impurity atom, the vacancy-impurity pair can exist in a variety of charge states, introducing different energy levels into the Si band gap compared to the isolated vacancy. As a consequence, the thermal stability of the defect is altered. Fig 2.7, taken from [15] shows the thermal stability of a variety of vacancy-defect pairs observed during ~15-30min isochronal annealing studies. An enhanced diffusion of the impurities has been found due to pairing with vacancies.

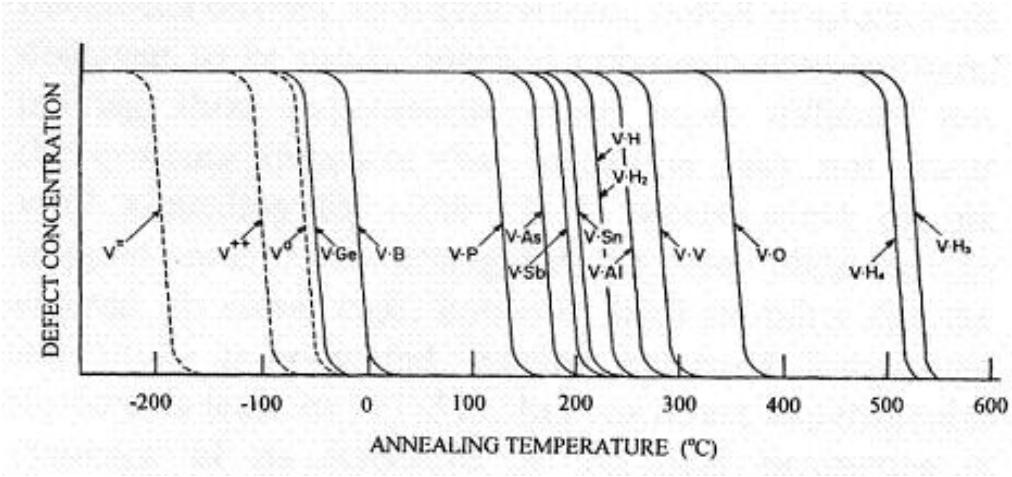

Figure 2.7: *Diagram depicting the thermal stability of vacancy-related defects after ~15-30min isochronal annealing [16].*

2.4.3 Interstitials

As previously described, an *interstitial* is either a displaced atom or implanted ion which does not reside on a lattice site. Much of the information about interstitials has been born out of theoretical research as there is little experimental evidence of their behaviour. Such theoretical work has suggested possible locations of the isolated interstitial and examples are given in Fig 2.8. This diagram shows an interstitial located at a) a tetrahedral site, b) a hexagonal site, c) a bond-centred site and d) an anti-bond site [14].

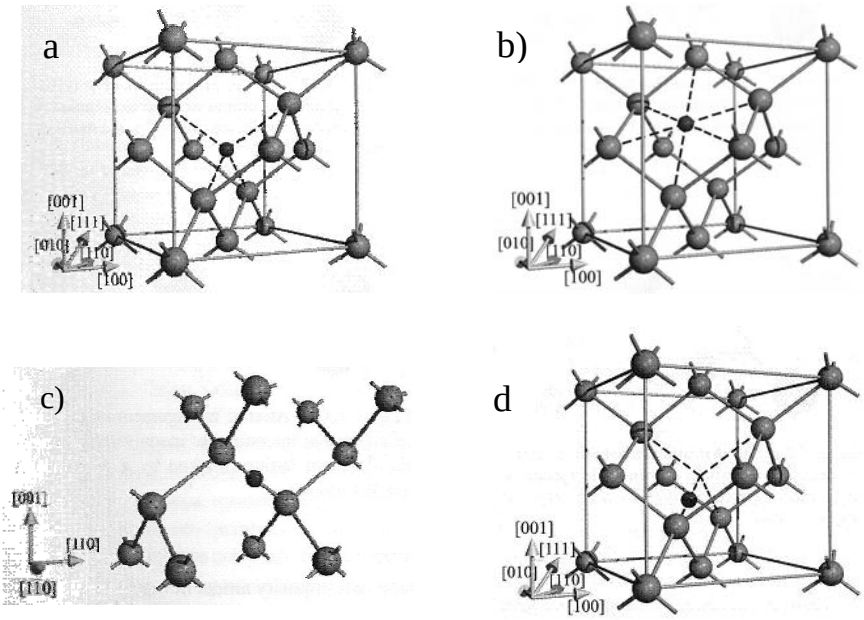

Figure 2.8: *Diagram showing theoretical interstitial positions in Si, a) tetrahedral interstitial site, b) hexagonal interstitial site, c) bond-centred interstitial site, d) anti-bond interstitial site [15].*

EPR experiments have attempted to investigate isolated interstitials. However, after electron irradiation at cryogenic temperatures, no EPR spectrum was found for the isolated interstitial in p-type Si. Spectra were produced corresponding to self-interstitial-impurity pairs. These defects were found to be in exact proportion to the isolated vacancies in the material. It was deduced from this that isolated interstitials are mobile even at 4.2K [15, 19]. Isolated interstitials have yet to be observed in n-type Si, however self-interstitial-impurity complexes were found to form at around about 140-175K [15], indicating the existence of the isolated interstitial. The difficulty with the identification of the isolated interstitial in n-type Si is that defect production is observed to be much lower than in p-type Si.

The structures of a variety of self-interstitial-impurity pairs have been identified experimentally by DLTS, EPR and LVM spectroscopy [15]. A substitutional Al atom trades places with a Si interstitial causing the Al atom to reside in the tetrahedral site as depicted in Figure 2.8 a). Boron assumes a position slightly off a bond-centred position, shown in Figure 2.8 c), whereas a C atom shares a lattice site with a Si atom as Figure 2.8 d) depicts [15].

During a ~15-30min isochronal anneal the annealing and formation temperatures of various interstitial related defects were found and are give in Figure 2.9, taken from [15].

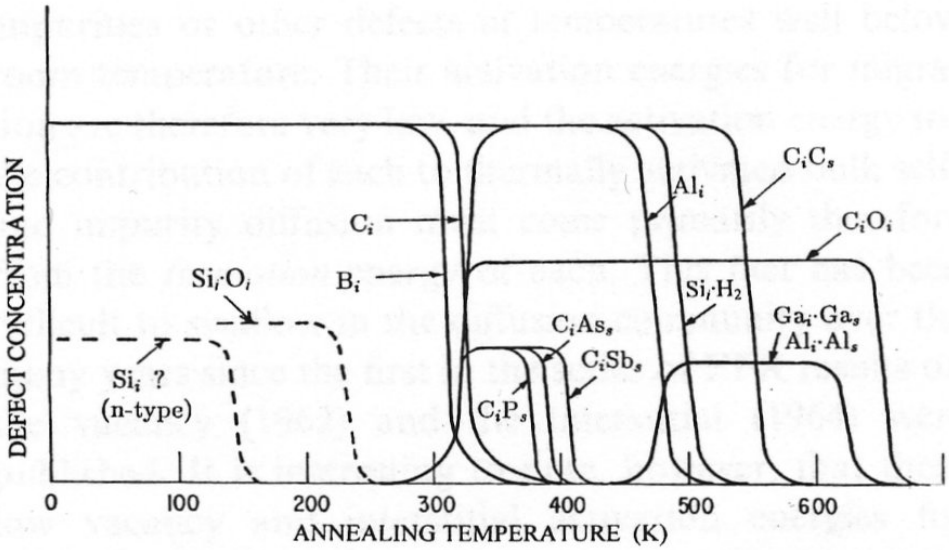

Figure 2.9: *Diagram showing the thermal stability of various interstitial-related defects during ~15-30min isochronal annealing [16].*

Other interstitial-related defects include interstitial carbon (C_i), interstitial boron (B_i), carbon interstitial-oxygen (C_iO), phosphorous-carbon interstitial (PC_i), boron interstitial-oxygen (B_iO) and boron interstitial-carbon (B_iC) complexes [20]. C_i and B_i are mobile at room temperature allowing them to migrate and form the aforementioned carbon and boron related defects [20].

EPR spectroscopy results of neutron-irradiated Si indicates the existence of di-interstitials. Theoretical studies combining tight-binding molecular dynamics, real-time multi-resolution analysis and *ab initio* calculations have reported several variations of the di-interstitial and tri-interstitial structures [21]. Other theoretical studies have investigated the 4-interstitial cluster [22]. Experimental investigations on interstitial clusters have yielded less information, however as interstitial clusters introduce deep levels into the Si band gap, DLTS has been used to investigate them [23]. Such studies have detected the Ostwald ripening of small interstitial clusters [24]. It is generally accepted that these small interstitial clusters are precursors to the formation of {113} defects. It is also believed that these clusters play an important role in TED [25, 26].

2.4.4 I-V pair

The existence of the I-V pair was first suggested by Tang *et al* [27] who used tight-binding simulation techniques to study the self-diffusion and interstitial-vacancy recombination in Si [4]. It was determined that a vacancy and interstitial can exist on a split interstitial site without recombination, similar to that depicted in Fig 2.8 d). This metastable defect structure consists of a "local rearrangement of bonds in the crystal with no excess or deficit of atoms" [4]. Fig 2.10 taken from [4] depicts the proposed atomic structure of the I-V pair. This bond arrangement gives rise to the five- and seven membered rings associated with amorphous Si, which is described in Section 2.5.1. The stability of I-V pairs was studied by Tang *et al* and by Cargnoni *et al* who used *ab* initio Hartree-Fock calculations [28]. From these studies the formation energy of the I-V pair was reported to be similar and possibly lower compared to other typical point defects found in Si. At room temperature, I-V pairs are expected to exist for several hours, with equilibrium concentrations again comparable to the other point defects [4]. However, as no dangling bonds exist the band structure of the material containing the I-V pair remains largely unaltered, making it difficult of even impossible to detect using EPR or DLTS. Therefore I-V pairs have yet to be observed experimentally.

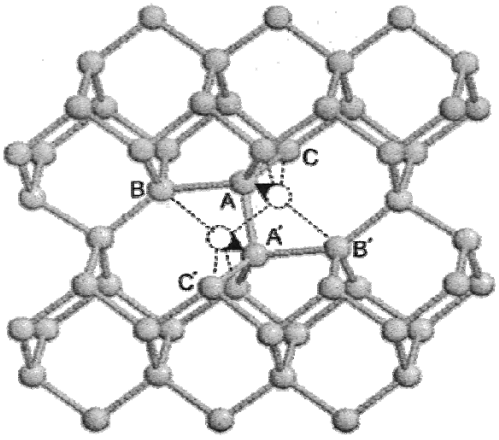

Figure 2.10: Proposed a*tomic structure of the I-V pair as given in Pelaz [5]. The atoms and bonds associated with the perfect Si lattice are represented by the dashed lines. Atoms A and A' have moved to positions along directions denoted by the arrows. They have swapped bonds with atoms B and B' thus forming an I-V pair.*

2.4.5 Dynamical Annealing

As a consequence of the thermally activated migration of vacancies and interstitials, recovery of the defected lattice during implantation can occur. This is known as *dynamical annealing* and it depends on the temperature of the material as well as the ion flux. Increasing the substrate temperature increases the thermal mobility of defects and consequently increases the probability that the defects will recombine. Dynamical annealing occurs due to the competition between arrival rate and removal rate through thermal mobility. It is possible therefore to increase the temperature to such a degree that amorphisation of the material is not possible. Conversely, if the material is kept at liquid nitrogen (LN_2) temperature during implantation, then little dynamical annealing occurs. Cryogenic temperatures therefore act to "freeze in" the damage produced where higher temperatures aid the recovery of the structure of the material.

2.5 Ion beam induced amorphisation of Si

Ion implantation is the primary technique used for the introduction of dopants into Si integrated circuits. As has already been discussed, ion implantation leads to the formation of various types of damage, from point defects or defect clusters surrounded by crystalline material, to complete amorphisation of a layer of Si. Such damage must be removed by thermal annealing so that only the effects of the dopants are experienced. Amorphisation may occur during fabrication of the circuits due to the large dopant concentration required and therefore the high fluences employed. Alternatively, ultra shallow junctions can be produced by implanting a lower concentration of dopants into a pre-amorphised layer, which suppresses the effects of channelling. Unfortunately, upon re-crystallisation of amorphous layers, defects remain behind at the original crystalline/amorphous (c/a) interface which may thermally evolve to form larger clusters and extended defects and also may lead to the transient-enhanced diffusion of dopants. Re-crystallisation of buried a-layers not only leads to the formation of these end-of-range defects, but also to defects located where the two c/a interfaces combine. Because amorphisation is an inevitable consequence of some of the techniques used in the manufacture of microprocessors, numerous studies have been performed in order to understand the process. As amorphisation occurs on an atomistic level, computer simulations have been extensively used, not only to determine the structure of a-Si but in an attempt to also understand the defect accumulation which leads ultimately to amorphisation. However, there is still a debate surrounding the mechanisms involved and a number of amorphisation models have been proposed. The following section describes a-Si and the nature of defects which may exist within it, as well as the most common models proposed for the amorphisation of Si due to energetic ion implantation.

2.5.1 Amorphous Si

The atomic structure of un-doped (virgin) crystalline silicon is described as two interpenetrating face centred cubic (fcc) structures with the second fcc structure displaced by x = ¼a, y= ¼b, z = ¼c with respect to the origin atom of the first structure. Each Si atom is covalently bonded to four other Si atoms, with these four nearest-neighbour atoms residing at the vertices of a tetrahedron. The

typical bond length at 300K is 2.35Å with the angle subtended between two adjacent bonds being approximately 109º [11]. This configuration of Si atoms leads to the formation of 6-membered ring structures indicative of crystalline Si (c-Si).

In 1973, using computer generated information, Polk and Boudreux described the structure of amorphous Si (a-Si) as a continuous tetrahedrally coordinated random-network of atoms [29]. The lack of crystallinity observed experimentally in a-Si, was therefore determined to be due to distortions of the bond angles and lengths produced after bond breaking and recombination, resulting in rotations of the tetrahedra. Such perturbations enable the formation of 5-, 6- and 7-membered rings resulting in a loss of long-range order, although four-fold coordination is maintained. Fig 2.11 shows the results from computer simulations illustrating the 6-membered rings indicative of c-Si as well as the 5- and 7-membered rings found in a-Si [4].

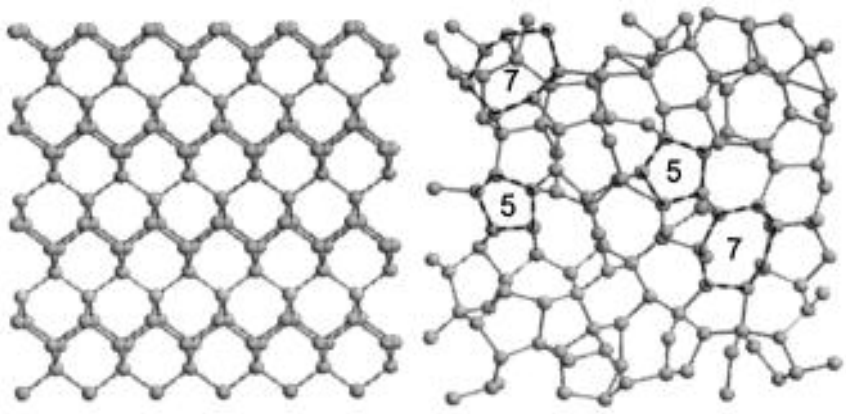

Figure 2.11: *Diagram showing the results from computer simulations illustrating the 6-membered rings indicative of c-Si, and the 5- and 7-membered rings found in a-Si, taken from Pelaz [5]. Viewing direction [110]*

In addition to the ring structures, many studies, both experimental and theoretical, have suggested the possibility of several types of defect present in as-implanted a-Si. Results from molecular dynamics simulations [30, 31] electron paramagnetic resonance (EPR) experiments [32] and theoretical techniques [33] imply the existence of 5-fold (floating bond) and 3-fold (dangling bond) coordinated atoms, although which defect dominates is as yet undecided. Further theoretical work [34] has suggested that a combination of both the dangling and

floating bond may be the dominant defect in a-Si, where it is thought the two atoms may form a weak bond to produce a configuration termed a frustrated bond. More recently, reverse Monte Carlo simulations, produced to aid the interpretation of experimental data on evaporated a-Si, yielded results which suggest that small bond angles of the order of 75º may exist [35]. A consequence of such small bond angles is the formation of square and triangular structures, which were determined to be new defects. Experiments have also indicated the existence of other defects, for example vacancy-type defects have been detected by those using Mössbauer measurements on Sn implanted into a-Si [36]. Results from *in-situ* conductivity measurements used to investigate defect accumulation during ion-implantation, and the structural relaxation which subsequently follows, suggest that highly strained Si bonds also exist in a-Si [37].

Unlike c-Si, the properties of a-Si such as vibrational, electrical and optical properties, are found to be dependant on the thermal history of the material as well as on the method of production, a fact confirmed by X-ray diffraction, ESR, optical-absorption and index-of-refraction measurements and room-temperature electrical conductivity data [38]. It has been found that a-Si, formed after energetic ion implantation has an intrinsic atomic density 1.76% less than c-Si, whereas a-Si produced by vapour deposition on a cold substrate has been reported to be more than 10% less dense than c-Si [38].

The recovery of an amorphous layer in Si can be achieved by heating the sample to temperatures upwards of 500°C. This process is called solid phase epitaxial re-growth (SPEG) and is explained in detail in Section 2.8. At temperatures below that required for SPEG, structural relaxation of the amorphous phase occurs which also results in a modification of its properties. There has been some debate as to the processes involved during this relaxation phase and many experimental studies have been conducted. Some authors report that during annealing, relaxation occurs due to a decrease in the bond-angle distortion which in turn reduces the elastic strain energy stored in the a-Si [39], while others believe that a combination of this and defect annihilation is responsible [40]. Relaxed a-Si can be “de-relaxed” by re-implanting with energetic ions, thus returning it to the as-

implanted state. Studies using calorimetry to investigate the defects in de-relaxed a-Si and highly damaged, ion-implanted c-Si found that the annealing behaviour was similar in both cases [40]. The highly damaged c-Si was found, by RBS and TEM, to contain point defects and small defect clusters. The measured heat flow curves during annealing of the c-Si and de-relaxed a-Si were found to be extremely similar, indicating that the processes involved in defect annihilation in c-Si and structural relaxation in de-relaxed a-Si are comparable. This leads to the conclusion that similar defects, ie vacancy-type and interstitial-type defects, are very likely to exist in both c-Si and a-Si. This was further confirmed by the same authors who detected a range of activation energies during annealing of a-Si which they attributed to different complexes of point defects [40]. The reduction in bond-angle distortion suggested in previous studies as the mechanism for structural relaxation [39] can also be interpreted in a way which corroborates the defect annihilation theory. It is known that defects in c-Si have an associated strain field causing distortion of the surrounding bonds, with calculations showing that atoms surrounding a monovacancy may be displaced 3% of a bond length inwards [40]. This leads to the possible conclusion that the annihilation of defects in a-Si will therefore also reduce the bond-angle distortion of the neighbouring atoms. Further studies on the diffusivity of Cu [41] and the gettering of Pd [42] in a-Si also confirm the presence of interstitial-type defects in the amorphous material. It is therefore the opinion of this author that the defect annihilation theory, as proposed by Roorda *et al* explains well the structural relaxation mechanism occurring in a-Si, with some of the results obtained being in good agreement with those found in this study.

2.5.2 Defect accumulation in c-Si

Various experimental techniques have been used to investigate the damage accumulation during ion implantation of c-Si. Due to dynamical annealing during the ballistic phase of implantation, fluence, flux and substrate temperature all have an effect on damage formation. Implantation at cryogenic temperatures largely freezes in the damage produced with very little annealing of this sort taking place, therefore only the fluence determines the type of resultant damage produced. For a constant fluence and ion flux, increasing the implant

temperature results in greater mobility of defects and therefore increased annihilation. This increased dynamical annealing can be counteracted by increasing the rate at which the ions are implanted (the flux), so that as more damage is introduced into the material per unit time there is an increased probability that a defect diffusing away from its collision cascade will interact with another defect from a different cascade resulting in the formation of a more stable defect complex.

Experimental studies have shown that under implantation conditions where defect production and dynamical annealing are close to balancing each other, the damage accumulation exhibits a superlinearity with increasing fluence [43].

Studies using Molecular Dynamic simulations and TEM have shown that the damage accumulation in Si also depends on the mass of the implanted ion. It has been found that higher mass ions produce more damage per unit volume because their nuclear energy deposition density is greater than for lighter ions.

To summarize, implantations with light ions, low fluences or high implantation temperatures result in highly damaged but crystalline Si. For heavier ion implants or those with greater fluence or decreased implantation temperature, damaged zones which are purported to be amorphous or a continuous a-layer may be formed. Extensive studies have been carried out with the aim of formulating a unified theory which explains the damage accumulation and amorphisation in the two regimes and which also agrees with experimental observations.

2.5.3 Models of amorphisation

The following describes the most common models developed to explain the amorphisation mechanism in Si.

2.5.3.1 Homogenous amorphisation

The homogeneous amorphisation model is concerned with the amount of energy deposited into the material per unit volume as a consequence of the nuclear

collisions during implantation. Depending on implantation temperature and fluence, the deposited energy gives rise to a particular point defect concentration spread homogeneously throughout the material. In this model it is the point defect concentration which is believed to lead to amorphisation. The Gibbs free energy of a system increases as more damage is introduced. At some critical defect concentration, the free energy of the highly damaged crystalline material is greater than that of the amorphous phase. At this point it becomes energetically favourable for amorphisation to occur and the lattice collapses into a-Si [44].

Dynamical annealing has a large influence on obtaining the defect concentrations necessary for amorphisation, as increased defect mobility during implantation results in increased annihilation of the defects, reducing the overall defect concentration. For implants at cryogenic temperatures where the damage produced is largely "frozen in", the critical energy density is not greatly dependant on the mass of the implanted ions. For low temperature implants where dynamical annealing is inhibited, some authors determined the critical energy density for all ion species to be $5x10^{20}$ keV cm^{-3} [44], which was later suggested by Gibbons to be about 10^{21} keV/cm^3 [3] At higher temperatures, the critical energy density is increased as dynamical annealing of defects causes a reduction in the energy stored in the lattice. For lighter ions, where the amount of damage produced per cascade is less than for heavier ions, the recovery effects of dynamical annealing are more prominent and so a greater critical energy density, or threshold damage density (TDD) is required. Prussin *et al* [44] determined experimentaly the TDD of arsenic, phosphorous and boron at room temperatures to be $2.5x10^{20}$ keV/cm^3, $1.0x10^{21}$ keV/cm^3 and $5x10^{21}$ keV/cm^3 respectively. Using the homogenous amorphisation model, a critical fluence for amorphisation can also be determined for each ion species. At a given energy, light ions produce dilute collision cascades with the damage spread over a larger area compared to the damage formation from heavy ion implantation. Therefore the amount of energy deposited per unit volume by a light ion is less than for a heavier ion. Irrespective of any dynamical annealing which may take place, a

greater fluence is therefore required for light ions to obtain the critical energy density, relative to heavy ion implantation.

This model would appear to be appropriate to light ion implantation at temperatures at RT or above. Here low density cascades are produced which contain simple point defects. These defects can diffuse away from the cascade and spread homogeneously throughout the material. After a period of point defect accumulation, the critical energy density and defect concentration is reached causing spontaneous collapse into the amorphous phase. Molecular dynamics (MD) simulations employed by Motooka [45] indicated that the accumulation of di-vacancy and di-interstitial pairs gave rise to the homogenous amorphisation in Si. Agglomeration of these into larger defects (or the production of amorphous zones) lowers the energy of the system compared to that which contains individual point defects. High resolution TEM (HRTEM) by the same author also observed sharp c/a interfaces produced by Si implantations at room temperature into Si. This result is in agreement with the homogenous, sudden transformation, mechanism which shows that there either exists a sufficient concentration of point defects for amorphisation to occur, or not. For heavy ion implantation, it is generally believed that another mechanism of amorphisation occurs.

2.5.3.2 Heterogeneous amorphisation

In the heterogeneous amorphisation model, the Si is amorphized locally to produce amorphous zones of the order of 1-10nm in diameter. This may occur as the result of single ion or multiple ion impacts. The overlapping of these zones at higher fluences eventually gives rise to complete amorphisation of a layer. During the thermal spike regime of a collision cascade, localised heating occurs which can lead to the melting of the material within the cascade volume. Due to the rapid rate at which this thermal energy dissipates, the damage is quenched resulting in a highly disordered region surrounding the ion track. For heavy ions, a single ion impact is purported to lead to the production of isolated amorphous zones due to this process. Amorphisation in this way can also be described in terms of the energy deposited per unit volume, where local defect concentrations within a collision cascade can exceed that which is necessary for amorphisation.

For lighter ions where amorphous zones are not produced following each cascade, an overlap of several cascades is required for the local energy density to reach the critical value.

A more quantitative model was proposed by Morehead and Crowder [46] which describes a cylindrical damaged region of radius R_0 surrounding the ion track as shown in Fig 2.12. In this model, point defects escape the region via thermal diffusion resulting in a stable amorphous core of reduced radius R_0-δR. Dynamical annealing therefore acts to shrink the zones in this situation. R_0 is larger for heavier ions due to the increased energy deposition density. The decrease in the effect of dynamical annealing on heavy ion implants results in a reduced value for δR. Gibbons [3] further developed this model so as to derive an expression for the number of cascades required to overlap in order to produce an isolated amorphous zone of a certain area. He showed that a decrease in ion mass resulted in an increase in the number of cascades required. Many authors have reported the existence of discrete amorphous areas, specifically after heavy ion implants or Si implants at cryogenic temperatures [47, 48].

It has been suggested that the actual mechanism through which amorphisation occurs will depend on the ion mass, with homogenous amorphisation occurring due to light ion implantations and the heterogeneous amorphisation resulting from heavy ion implants. It has also been reported that both mechanisms can describe the result of implanting with the same ion species but at different temperatures. Motooka [45] compared self-implantation at cryogenic and room temperatures. High resolution TEM analysis of the cryogenic implant showed a rough c/a interface attributed to the overlap of damage from many cascades, whereas a sharp c/a interface typical of homogenous amorphisation was found in the sample implanted at room temperature.

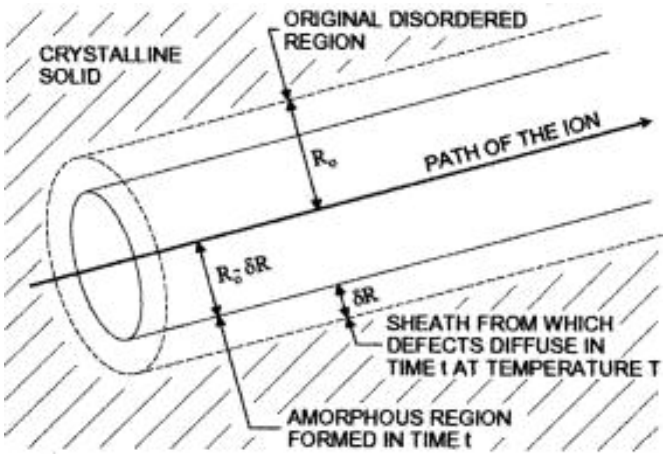

Figure 2.12: *Diagram showing the heterogeneous model as proposed by Morehead and Crowder [47]. In this model a single ion impact results in a highly damaged region surrounding the path of the ion which, during a time t, reduces in size due to the diffusion of defects from the volume leaving behind a stable amorphous core.*

2.5.3.3 Nucleation limited model

It is known, from TEM observation [49] that pre-existing amorphous zones and c/a interfaces act as preferential nucleation sites for further amorphisation. The nucleation limited model (also known as nucleation and growth) extends this fact by suggesting that amorphisation occurs via a two stage process; the accumulation of damage results in the production of amorphous zones which then grow (or shrink) due to the interaction with simple defect complexes [50]. These defects originate at the end-of-range (EOR) of the ion track. It is believed that after the initial collision cascade, the residual EOR damage agglomerates to form clusters and larger extended defects. Increasing the fluence results in the formation of more complex defects which increases the local defect density and free energy of the material until amorphisation occurs. This model states that the defects responsible for amorphisation are similar in nature, independent of ion species and that nucleation occurs at the end of range of the ions. However a range of activation energies has been found [50] corresponding to the defects believed to be responsible for amorphisation, which do depend on implanted ion species as well as substrate temperature. The superlinearity of damage accumulation observed by Goldberg *et al* [50] suggests that amorphisation is more effective when the material is already damaged, as this model describes.

2.5.3.4 The I-V pair

Some authors believe that the I-V pair is the defect responsible for amorphisation. Results from computational studies [51] have suggested that this defect is formed during ballistic processes . It is also a characteristic feature of the interface between a-Si and (001) c-Si [52].

MD simulations by Marqués *et al* [52] investigated the effect of I-V pair accumulation on the amorphisation process is Si. They reported that the effective energy barrier for recombination is 0.43eV which leads to the life-time of I-V pairs at room temperature to be in fact only about 3 microseconds [52], which gives a possible explanation as to why they have yet to be identified experimentally. By introducing varying amounts of I-V pairs into their simulations, they were able to observe the subsequent damage accumulation during ion implantation. They found that a 30% concentration of I-V pairs leads to homogenous amorphisation, while concentrations of 25% subjected to various implantation temperatures, resulted in an amorphisation process resembling that explained by the nucleation and growth model; at T=1000K recrystallisation occurred, for T=1200K polycrystalline material was produced and for T=1600K amorphisation was observed [52]. More importantly it was found that although for relatively low concentrations (about 10%) re-crystallisation occurs by recombination of the interstitial and vacancy in the pair, higher concentrations lead to the agglomeration of I-V pairs, or a grouping with Si self-interstitials into more stable defects. As, during irradiation, these may then evolve into extended defects, these complexes could therefore be thought of as the embryos for amorphisation envisaged in the nucleation and growth model.

2.6 Secondary interstitial-type defects

Defect formation, migration and dissociation are thermally activated processes. As previously described, vacancies and interstitials are mobile at very low temperatures, so it is generally thought that at room temperature and above, such isolated defects do not exist as they have diffused through the material and combined with other isolated defects either to annihilate or form larger clusters. The larger the cluster the more stable it is and so more energy is required to cause it to dissociate. In general, the formation of more complicated, stable defect structures occurs during thermal annealing. As the annealing temperature is increased, interstitial-type defects can evolve into interstitial clusters about 2nm in size, then into {113} defects and finally into two types of dislocation loops [26].

The type of secondary defect which is produced depends on the nature of the as-implanted damage, annealing temperature and implanted ion species. In order for certain interstitial-type, extended defects to form, an initial critical concentration of interstitials must be reached. For example, implanting 1MeV B with a fluence of $4x10^{13}$ ions/cm^2 results in some primary damage. After a 900ºC anneal for 15mins no secondary defects are formed. However implanting 1MeV B with a fluence of $1x10^{14}$ ions/cm^2, results in a greater excess of interstitials in the as-implanted material. Annealing of this sample at 900ºC for 15mins results in the formation of dislocation loops and lines [19].

Because of the many factors governing the thermal evolution of defects, Jones *et al* [53] devised a classification system which describes the types of extended defects produced in Si after annealing, with respect to the as-implanted damage. Fig 2.13 depicts this system. Category I damage refers to all secondary defects that are produced from non-amorphising implants, for example defect clusters, dislocations, {311} stacking faults and other rod-like defects. When an amorphous layer is produced there exist small defects behind the c/a interface in the crystalline material. These defects will develop into dislocation loops if appropriate annealing conditions are satisfied, for example 900ºC for 30mins [53]. and are classified as category II damage. Category III damage result after the imperfect re-growth of an amorphous layer. The main types are hairpin

dislocations and microtwins which are located in the region of the original amorphous layer. Under specific implantation conditions, a buried amorphous layer can be formed. Re-growth of such a layer occurs by the two c/a interfaces advancing towards each other. Category IV damage is formed where the two interfaces combine and depending on the annealing conditions can evolve into dislocation loops. The final category of damage, category V damage, consists of precipitates of the implanted ion species. They form when the solid solubility of the impurity is exceeded during annealing. All these defects are described in the following sections.

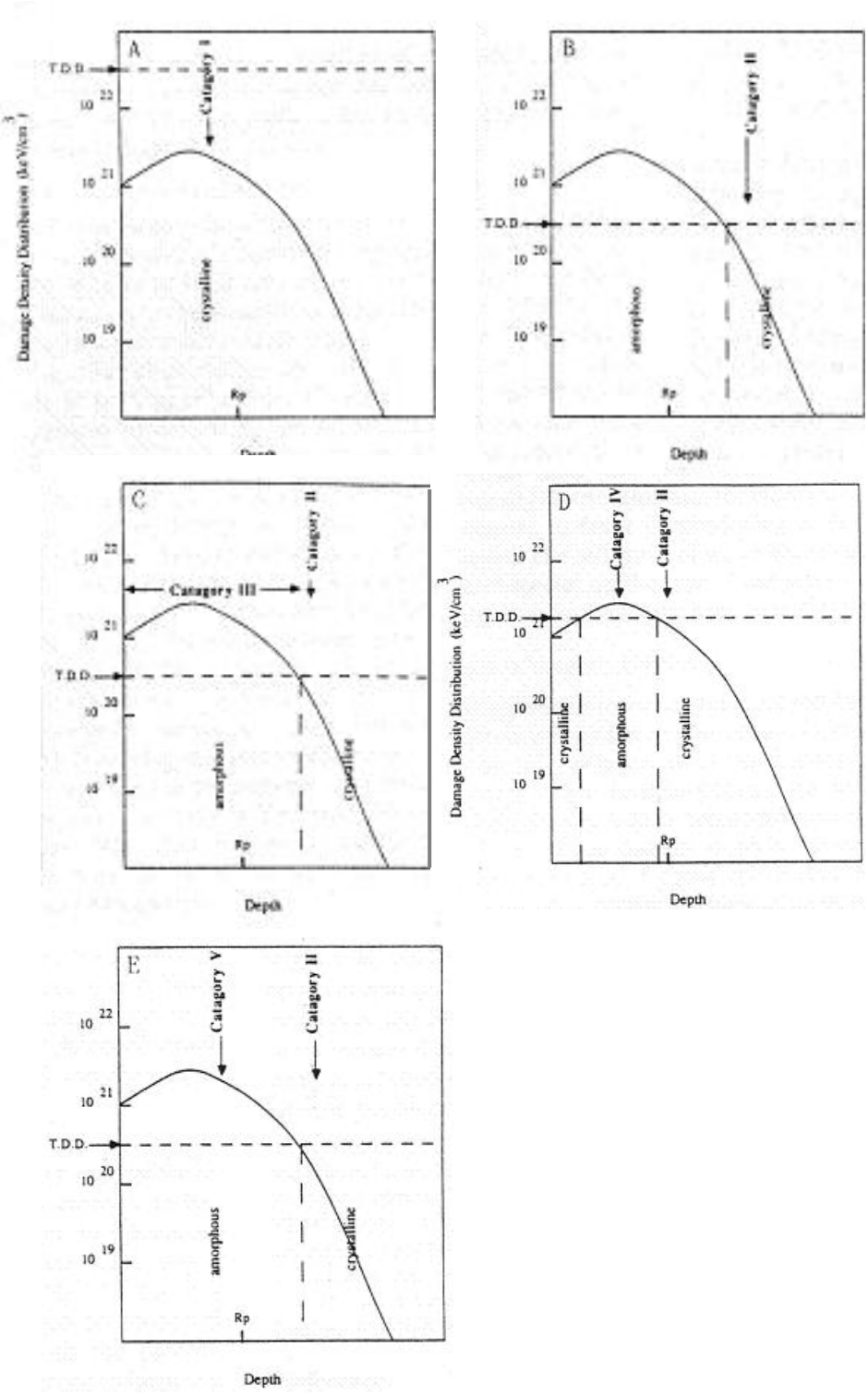

Figure 2.13: Schematics depicting the classification system as developed by Jones *et al [52]*. The curves represent the damage density distribution and the dotted horizontal lines depict the effective threshold damage density associated with production of an amorphous layer.

The evolution of non-amorphising implants as a function of annealing temperature was investigated by Seshan and Washburn [54]. They found that between 200 and 350°C di-vacancies, di-interstitials and small point defects were formed. From 350 to 650°C the small clusters increase in size and decrease in density. Between 650 and 800°C dislocation loops were found to form and above 800°C only circular dislocation loops remain [19].

Goldberg *et al* [55] used TEM to report the secondary defect structures produced in Si after annealing at temperatures between 600 and 1000°C. The as-implanted damage was produced by implanting at about 90°C with $2x10^{15}$ ions/cm^2 Si and energy of 540keV. Fig 2.14 depicts their findings after 20min anneals. Below 600 °C there exist very few defect structures resolvable by TEM. Above 600 °C clusters are found to dissolve or develop into dislocation loops or lines. Defects which form at about 750 °C have been found using TEM to be almost always interstitial in nature. Annealing above 900 °C causes all defects to disassociate whilst at 1000 °C relatively few defects remain [55].

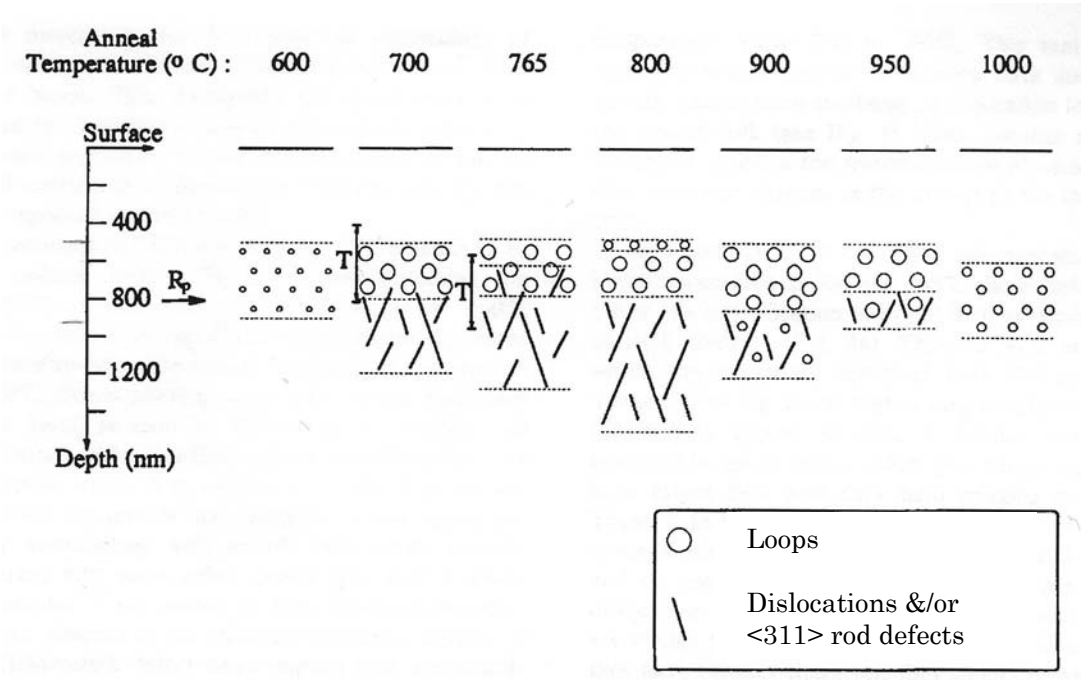

Figure 2.14: *Diagram depicting the secondary defects formed in self-implanted (100) Si of fluence $2x10^{15}$ions/cm^2 and energy of 540 keV. Annealing was performed in the temperature range of 600 to 1000 °C, for 20mins [54].*

The following section describes the interstitial-type defects formed during thermal annealing and the proposed mechanisms of their formation.

2.6.1 Ostwald Ripening

All interstitial-type defects are believed to thermally evolve by a competitive growth mechanism called Ostwald Ripening. This mechanism was originally devised in order to describe the growth of liquid droplets in equilibrium with their vapour [26]. Since then, much experimental [56] and theoretical [26] research has successfully used this model to describe the thermal evolution of interstitial defects in Si. Depending on the defects' formation energy and ability to capture Si atoms, an exchange if Si atoms occurs between the defects by diffusion. The volume between the defects is therefore oversaturated with free Si interstitial atoms. The energy required to add an extra atom to the defect is smaller for larger defects compared to smaller defects. Therefore interstitial gradients occur between the different sized defects and smaller defects decrease in size as larger defects grow.

Many experiments [1] [57] have found that the diffusivity of B in Si is greatly enhanced by the presence of interstitial-type defects. This enhanced diffusivity is known as transient enhanced diffusion (TED). The annealing process required for B to become electrically active once implanted into c-Si results in an excess of Si interstitials of the same number of substitutional B atoms. The excess Si atoms clusters together to form extended defects such as {113} defects or dislocation loops. The Ostwald Ripening model of interstitial-defect growth has been successfully used to explain the experimental results of TED of B [1], as the supersaturation of Si atoms located in the vicinity of the defects combine with B to form mobile Si-B pairs.

Small interstitial defect clusters are thought to be precursors to the formation of {113} defects. Interstitials after implantation agglomerate into di-interstitials [25]. During the low temperature annealing regime (less than 600°C) these di-interstitals evolve into larger defect clusters and eventually, at higher temperatures, form {113} defects by Ostwald Ripening. Theoretical models have

also successfully used the Ostwald Ripening model to described the dissolution of {113} defects and their transformation into dislocation loops [58].

2.6.2 {113} rod-like and ribbon like defects

{113} rod-like and ribbon-like defects have been observed experimentally in Si and Ge [25]. Computer modelling and TEM of these defects have deduced their composition to be agglomerates of <110> rows of Si self-interstitials [25] Their structures are found to differ depending on how they are produced. Ion implantation and subsequent thermal annealing result in very thin "rod-like defects" being formed. Wider "planar" {113} defects are produced via electron and ion irradiation.

Results from high resolution TEM (HRTEM) studies of {113} planar defects, produced in Si by 2 MeV electron irradiation at 450°C, gave an estimation of the defects relative displacement vector **R** to be $a/25$ <116>, which is almost perpendicular to the defect plane [25]. In this experiment, the Si chains were found to extend in the <110> direction [25]. Fig 2.15 is a computer generated model of the likely structure of a {113} defect, taken from [25]. This figure shows that the planar defect is made up chains of 5-, 6-, 7- and 8-membred rings and that there are no dangling bonds in the {110} cross-section. The 6-membred ring is different to that found in the non-perturbed c-Si lattice and it is classed as a hexagonal-type structure. The width of each chain differs. Each chain is connected with an 8-membered ring, and the connected chains extend along the <332> direction. The chains at the edge of the structure bond with the c-Si lattice via 5- and 7-membered rings. Although the {113} planar defect is not a true stacking fault, TEM images reveal fringe contrast due to phase contrast. For an explanation of phase contrast see Chapter 3.

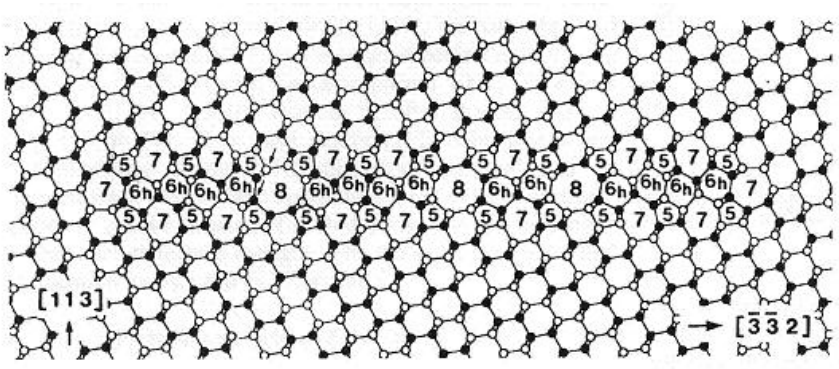

Figure 2.15: *Computational representation of the atomic structure of a planar {113} defect as viewed along a <110> direction [26].*

The rod-like defects produced after ion implantation have been observed by TEM to be elongated in the <110> direction. Theoretical studies have determined that, as with the planar defect, the width of the rod-like defect is along the <332> direction with 5- and 7-membred rings at its edges. Similar theoretical studies have indicated and HRTEM [25] has confirmed the existence of a defect consisting of a single line of di-interstitials along the <110> direction with dangling bonds at its ends. This defect is known as a "line interstitial defect" (LID). Small {113} defects, about 2nm in size have been found to contain about 40 atoms [25, 59].

2.6.3 Dislocation loops

The strain introduced by the existence of defect clusters or {113}'s can be relaxed by the collapse of these defects into "sheets" or planes of interstitials. Such a "sheet" of defects can be contained completely in the material and as such are known as dislocation loops. They tend to form in crystallographic planes where the energy required to do so is a minimum. A dislocation can be described as either an extra plane of atoms added to the crystalline material, known as an extrinsic dislocation, or the removal of a plane of atoms from the lattice, called an intrinsic dislocation. Dislocations formed as a consequence of the implantations resulting in an excess of Si atoms are extrinsic. Dislocations generally also introduce stacking faults into the material. It is convenient to think of two types of extrinsic dislocations. An *edge dislocation* can be thought of as an extra plane of atoms introduced into the material in a manner that maintains the regularity

of the perfect crystal. The bottom of the extra plane of atoms defines the boundary of the dislocation and is called the dislocation line. In an edge dislocation this is always perpendicular to the Burgers vector which defines the magnitude and direction of the slip caused by the defect. In a *screw dislocation*, the Burgers vector is parallel to the dislocation line. Such a defect can be imagined by first cutting along a plane perpendicular to the surface, some distance into the material. The material on one side of this cut is then displaced in an upwards direction one atomic displacement, thus causing a stacking fault until the end of the cut line. Dislocations in real materials may be a mixture of both edge and crew type. Many TEM and theoretical investigations have studied the formation of dislocation loops during post-implantation annealing.

Dislocations can be found in self-irradiated Si after annealing at temperatures above 600ºC. They can also evolve from the defects which reside behind an a-layer (category II defects). Upon re-crystallisation of the layer, these defects remain around their original position corresponding to the EOR of the ion track, and at sufficient annealing temperatures develop into dislocation loops. The maximum annealing temperature throughout this study was 600 ºC which, for the implanted species used, was not sufficient for dislocations to be formed.

2.7 Noble gas implantation

Numerous investigations have been undertaken to study noble gases in solids. A large amount of this research was to determine the affects of these gases on nuclear reactor materials. He is produced in large amounts in fusion reactors, and the heavier gases such as Kr and Xe may be produced as bi-products of nuclear reactions [60]. All the inert gases have a very low solid solubility in metals and semiconductors which leads to the formation of He gas bubbles. Research [60-62] has shown that, because of the low permeability of He in metals, the majority of gas in the bubbles is retained during thermal annealing. These bubbles grow in size and decrease in density by migration and coalescence. This growth mechanism is different to that of interstitial-type defects and it results from the motion of the bubbles through the material, and is explained below. He is only released from metals when the bubbles intersect the surface

causing blistering and, in some cases, exfoliation of the surface. In Si, He has a high permeability and so at annealing temperatures upwards of 400°C the gas begins to dissociate from the bubbles and diffuse through the material, and is eventually lost to the surface. He is readily lost at temperatures of around 700°C. Therefore blistering does not occur during the annealing of He implanted Si and stable empty cavities remain in the Si following He diffusion. These stable cavities may be used as a means of trapping metal impurities, a technique known as gettering and which is envisaged as having technological applications. The permeability of the heavier gases in Si is lower compared to He and so, much of the gas is retained during annealing.

Chapter 5 of this study details an investigation which was performed to determine the effects of vacancy and interstitial-type defects on a moving c/a interface during the thermally activated re-growth of the a-layer. As a consequence of the numerous studies which have been undertaken, much is known about He gas implantation in Si. The as-implanted distribution of He is well defined and can be accurately determined for a given energy using TRIM. Analysis of the as-implanted and annealed defect structures can be successfully carried out using TEM. In addition, noble gas implantation will not result in an alteration in the chemistry of the Si. Taking these factors into account, it was determined that He implantation was the most appropriate for the investigation detailed in Chapter 5.

The heavier noble gases have also been researched experimentally [63-71]. Much of this research was conducted on room temperature implantations which results in the amorphisation of the sample. More recent studies have investigated the damage produced in Si following high temperature (350°C) Ne implantations, where amorphisation was suppressed, and the mechanisms of bubble formation were explored using TEM and RBS [68]. Little research has been conducted in this temperature regime for Xe. Therefore a TEM analysis of the damage morphologies produced after high temperature Xe implantation and thermal annealing was carried out during this study and is also detailed in Chapter 4.

The following section describes bubble formation, growth and evolution into cavities under a variety of implantation and annealing conditions, with special consideration given to He implantation in Si. Heavier noble gas implantations are discussed further in Section 2.8.

2.7.1 Bubble formation in Si

Depending on implant and annealing conditions and on ion species, inert gas bubbles may be produced which either dissolve leading to near complete damage recovery, evolve into empty cavities or form gas filled cavities in which the gas may be in the form of a dense fluid or even solid. Under certain conditions, the latter two results may be accompanied by the production of extended interstitial-type defects such as rod and ribbon-like defects and dislocations. Many studies have been carried out in order to determine the bubble nucleation process and evolution under thermal annealing. It has been found that for noble gas implantations, the as-implanted bubble structures are highly influenced by ion fluence and substrate temperature, and consequently the bubbles' growth mechanisms vary for the different regimes. Dynamical annealing also affects the type of defect structures produced. Implantations with heavy gases such as Ar, Kr and Xe, may result in the creation of amorphous layers even at high temperatures. For example, Xe implantation at 350°C with fluence of the order of $1x10^{16}$ ions/cm^2 results in a buried a-layer (see Figures 4.4 and 4.5 in Chapter 4). However, implantations using He ions must be performed at cryogenic temperatures in order to amorphize the Si.

Bubble formation in Si following He implantation was first reported in the early 80s [72]. In 1987, C. C. Griffioen *et al* [73], using thermal helium desorption spectroscopy (THDS) and TEM, were the first to report on He desorption from bubbles to form voids in Si. The as-implanted samples, implanted with $2x10^{17}$ He ions/cm^2 at RT, contained a high density of small bubbles approximately 3.5nm in size. Their results suggested that the release of He from the bubbles occurs in two stages; the majority permeating between 330 and 630°C with the final release at about 930°C. This two stage desorption regime was also described by Corni *et al* [74] who reported on the thermodynamics and kinetics of He_n-V_m

clusters which occurred during the annealing of Si implanted with $5x10^{15}$ ions/cm^2 at LN_2 temperatures. It was found that 65% of the He was trapped by vacancy-type defects with 35% having formed more stable defects. As the implantations were carried out at LN_2 temperatures, the nature of the post implant damage without the effects of dynamical annealing were reported. Three regions were described; in the near surface region, an abundance of vacancy-like defects, some containing He atoms, were found. The intermediate region contained partially filled He_n-V_m complexes with the final region consisting of He in interstitial positions. Annealing at 250ºC resulted in the He atoms moving towards the surface to combine with the vacancy-type defects. After 700ºC the He had escaped from the bubbles and the resultant unstable cavities then dissolve. Pivac *et al* [75] deduced experimentally that the critical condition for stable bubble formation is the presence of vacancy agglomerates comprising more than four vacancies. If such defects are not formed in the as-implanted Si then bubbles will not form during annealing [76].

Helium bubble formation and evolution is a complex phenomenon. As with substitutional implant species, the implantation temperature and fluence dictates the as-implanted damage structures with dynamical annealing playing a major role in whether bubbles are produced or not. Second to this, the as-implanted damage and annealing temperature and times then determine the different regimes of bubble evolution and, consequently, the final defect structures. What is clear however is the dose dependence on bubble formation. For example at RT, fluences $\varphi < 5x10^{15}$ ions/cm^2, He_mV_n complexes dissociate at low temperatures (<400ºC) preventing bubble formation. At intermediate fluences $5x10^{15} < \varphi < 1x10^{16}$ ions/cm^2, even though much of the He desorbs during low temperature annealing, there still exists significant amounts and bubbles are produced. These bubbles have associated strong strain fields corresponding to He atoms under high pressure. Finally for high fluences where $\varphi > 1x10^{16}$ ions/cm^2 bubble nucleation readily occurs and stable cavities are produced after thermal treatments [77].

2.7.2 The effects of implantation and annealing temperature

Pivac *et al* [75] investigated the low temperature annealing regime of $2x10^{16}$ ions/cm^2 implantations. They reported that He is mobile at 200ºC and then agglomerates into planar defects parallel to the implanted surface. As the annealing temperature is increased so are the defects' associated strain fields until at 450ºC they transform into large bubbles.

Planar defect structures were also reported by Fichtner *et al* [77] who investigated the "medium fluence" regime, following implantation at RT. After 300ºC anneals for 600s, planar defects with strong strain fields were observed. The planar defects remain after anneals in the 400ºC ≤ T ≤ 470 ºC range, however they were surrounded by a ring of small cavities. Between 470 and 700 ºC the planar defects transformed into ellipsoidal cavities, again with the ring of small cavities. At annealing temperatures of 800 to 1000ºC spherical cavities located in circular planar domains were reported. The transformation from planar defects to ellipsoid defects was explained by means of a pressure relaxation process whereby Si atoms were punched out of the defect which in turn coalesced into dislocations surrounding the cavity. There also occurs a decrease in cavity size during higher temperature anneals, corresponding to the concomitant release of He and re-absorption of Si atoms. In the high temperature regime the authors concluded that the cavities grew by Ostwald ripening.

Da Silva *et al* [78] investigated the effect of implantation temperature T_i on implants of fluence of $1x10^{16}$ ions/cm^2. They reported that for $T_i \leq 423K$, a high density of small (radius ~ 0.8nm) He filled bubbles were formed with small {113} defects located around the bubble layer. The number of Si atoms required to form the defects corresponded exactly to those displaced during the bubble formation. As the He is desorbed with increasing annealing temperature, the {113} defects dissolved releasing the Si interstitials which re-combined with the empty cavities, annihilating them. Implanting at 623K results in the formation of a smaller number of larger bubbles (radius ~ 3.6nm). Large {113} defects attached to the bubbles, dislocation and defect clusters were also imaged by TEM. After a 1073K anneal, the cavities had decreased in size, again due to Si atom re-

absorption, and dislocations remained. Intermediate implantation temperatures resulted in a combination of the structures and thermal evolution of the high and low cases. For all regimes, the {113} defects were formed after the over pressurized bubbles punched out Si atoms.

Higher temperature implantations, such as those carried out by Beaufort *et al* [79] resulted in only extended defects being formed. No cavities existed in the as-implanted sample, only {113} rod-like and ribbon-like defects which transformed into dislocations after a 1000ºC anneal. Oliviero *et al* [80] reported that if T_i = 600ºC, then empty cavities would be formed during implantation. They found that, independent of implantation temperature, He permeated from both cavities and voids to the surface with an activation energy of 1.8eV.

Bubble formation and the subsequent thermal development is very complex as many factors govern the as-implanted structure which then determines the evolutionary processes involved during thermal annealing.

2.8 Solid Phase Re-growth of a-Si

Throughout this study, amorphous layers in a crystalline silicon matrix were re-crystallised using furnace annealing (FA), which involved heating the samples in a clean quartz tube, under vacuum in a tube furnace, generally at 600ºC for 30 minutes. The following describes the thermal re-crystallisation of amorphous layers, produced by ion implantation, in Si.

Continuous amorphous layers formed by ion implantation can be made to re-crystallise by heating the material to temperatures above about half the melting point of the crystal, which for Si is approximately 500ºC. This process of re-crystallisation is known as solid phase epitaxial growth (SPEG). The term "solid phase" results from the fact that the material remains solid throughout the process as the temperatures required do not cause melting of the material. Re-crystallisation occurs at the interface between the amorphous and crystalline phases, using the crystalline matrix as a template onto which the amorphous structure re-assembles itself, a process known as epitaxy. A surface a-layer re-crystallises by the movement of the c/a interface towards the surface, whereas the two c/a interfaces of a buried a-layer move towards each other until complete re-crystallisation of the layer has occurred. Figure 2.16 illustrates the SPEG of surface and buried a-layers respectively.

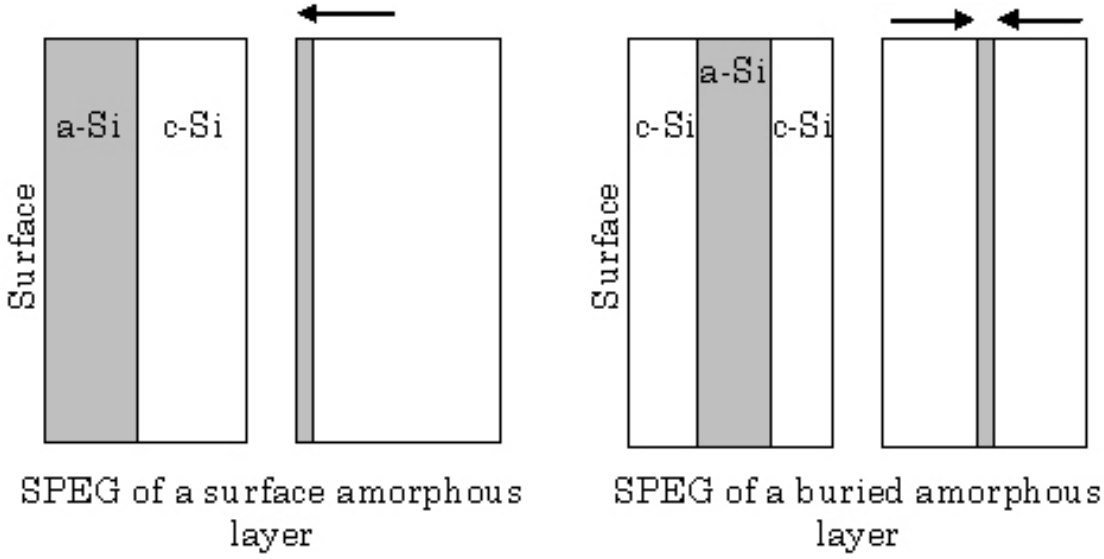

Figure 2.16: *Schematic describing the motions of the c/a interfaces during SPEG of (a) a surface a-layer and (b) a buried a-layer.*

Integrated circuit production requires the accurate doping of semiconductors (so that the concentration and distribution of the impurity is known and controllable) and the electrical activation of the impurities. As stated at the beginning of this chapter, ion implantation is currently the best method available for accurately introducing dopants into semiconductors. It has been found that SPEG of surface a-layers containing group and impurities may result in the incorporation of the impurities into electrically active positions. Further, the concentrations of electrically active dopants in samples amorphized and then thermally re-crystallised are much greater compared to non–amorphising implants which have been annealed. It is also possible, using SPEG, to achieve impurity concentrations greater than the maximum equilibrium concentration of that impurity.

Recovery of the damage produced by implantation generally results in a broadening of the dopant profile. The extent of the broadening depends on the type of as-implanted damage. The annealing of damage produced following non-amorphising implants results in complex secondary defect structures. The damage following SPEG is different, and depends largely on the implant species. For all amorphising implants there exists a layer of small defect clusters beyond the original c/a interface, which can evolve into dislocation loops at sufficient annealing temperatures. These defects are also involved in TED and the gettering of impurities, and lead to anomalous impurity profiles which have been recorded following re-crystallisation.

The re-growth rates of a-layers are dependant on annealing temperature, the crystallographic orientation of the material and the dopants and impurities which exist inside the layer. Figure 2.17 [81] describes the annealing temperature dependence of re-crystallisation, where an increase in temperature gives rise to an increase in velocity of the moving c/a interface. The curves in this figure were constructed using RBS data taken during the re-crystallisation of surface a-layers in <111> orientated Si. These a-layers were produced after implantation with Si ions at low temperatures, allowing for virtually impurity

free layers to be investigated. The velocity of the c/a interface, v, can be described by an Arrhenius relationship, such as:

$$v = v_0 \exp\left(-E_a / kT\right)$$

where v_0 is the velocity prefactor and E_a the activation energy for SPEG, the values of which are generally accepted to be 4.64 x 10^{-6} ms^{-1} and 2.7±0.02eV respectively [82].

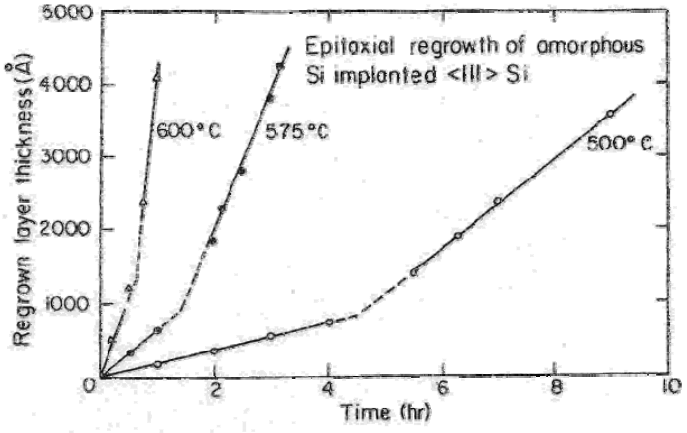

Figure 2.17: *Graph illustrating the temperature dependence on the re-growth rate of a-layers in (111) Si. All three curves are bi-linear with an increase in the re-growth rate observed at 1000Å for all three temperature regimes [80].*

In the following section, models describing the re-crystallisation of continuous amorphous layers by SPEG, factors which affect the re-growth rate and the defect structures which are produced under specific conditions will be further discussed.

2.8.1 Substrate orientation dependence

In addition to the temperature dependence, it has been found that the rate of re-crystallisation is also strongly dependant on the orientation of the substrate. For amorphising self-implants into Si at cryogenic temperatures, Csepregi *et al* found using RBS that the re-growth rate at 550°C for <100> orientated Si was three times higher than that of <110> Si [81]. For these orientations, the moving planar c/a interface maintains its uniformity and the rate of re-growth remains

constant as the layer re-crystallises. The resultant re-crystallised layer was found to be free from defects. The re-crystallisation rate of <111> orientated Si however was found to be bi-linear as Figure 2.17 above describes. The initial re-growth rate was found to be 25 times slower than that of the <100> orientated Si annealed at the same temperature [83], with the alteration in re-growth rate occurring at about 1000Å for all the annealing temperatures investigated. Figure 2.18 gives a comparison of the re-crystallisation rates associated with <100>, <110> and <111> orientated Si found during these studies during a 550ºC anneal. [83]

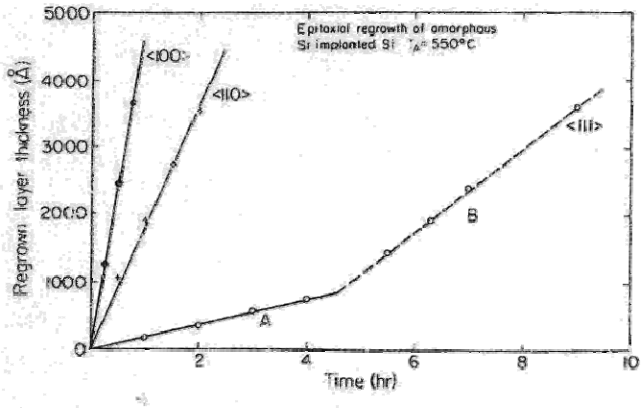

Figure 2.18: *Graph illustrating difference in a-layer re-growth rates experienced by the three major crystallographic directions in Si [82].*

For <111> orientated Si, an increase in the re-growth rate was observed after the layer had re-grown 1000 Å and RBS measurements [83] have shown that during this second phase the planar c/a interface loses its regularity and subsequently a high concentration of residual defects after re-crystallisation was detected. TEM analysis of these defects inferred the existence of stacking faults and/or microtwins [83]. The formation of microtwins appears to coincide with this increase in re-growth rate. Models describing this orientation dependence on growth rate and the formation of microtwins will be described in the following sections.

2.8.2 Impurity dependence

The re-growth rate is also strongly influenced by the presence of impurities. Group III and V elements, i.e. boron, phosphorus and arsenic, are used as

dopants in Si. Csepregi *et al* found using RBS data that concentrations of about 0.5at% of these dopants (fluences of the order 10^{15} – $5x10^{15}$ cm^{-2}) resulted in an enhancement of the re-growth rate by factors of 6-25 [84]. For P^+ implanted layers, the authors reported that the SPEG rate was not linear with time, even in <100> orientated Si. As the re-crystallisation progressed, the c/a interface velocity was initially comparable to that of the self-implanted layers discussed previously. As the concentration of P^+ increased towards the centre of the layer, so did the velocity of the c/a interface. After a maximum, the P^+ concentration decreases towards the surface which also corresponded to a decrease in a-layer re-growth rate. For As implanted layers, the same study reported that in the centre of the a-layer, where the maximum As concentration was $2.4x10^{20}$ ions/cm^3, the layer re-crystallised at a rate of 50Å/min during a 500ºC anneal, comparable to the P re-growth rate [84]. After re-crystallisation of As incorporated layers, it was deduced that 80% of As atoms were located at substitutional lattice sites [84]. Similar trends were observed after B a-layers were re-grown.

More recent studies [85] using the medium energy ion scattering (MEIS) technique have analysed the SPEG of layers produced after low energy P^+ implantation. Their results were in agreement with that of Csepregi *et al*, however higher concentrations were also investigated where it was found that at above a critical concentration of $1x10^{21}$ cm^{-3} the re-growth rate was severely retarded. This retardation at a critical concentration was also reported by several other authors for different impurity implants. This data was compiled by Poate and Williams into the graph shown in Figure 2.19 [86] (p28).

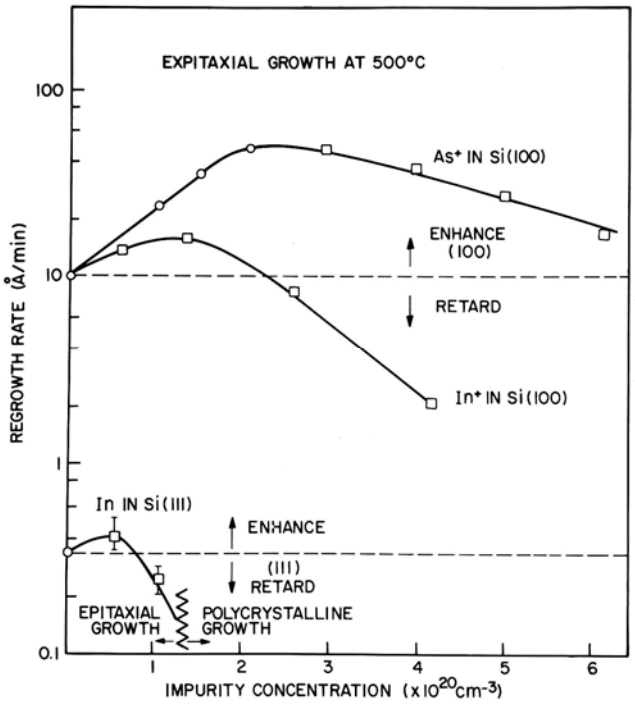

Figure 2.19: *Graph illustrating the re-growth rate dependence on dopant impurity concentration. An enhancement is observed initially until the solubility limit of the impurity is reached at which point re-crystallisation of the layer is retarded [85].*

This graph clearly describes the concentration dependence on re-growth rate for As and In implants for (100) Si and for In implants into (111) orientated Si. These defects have a high solid solubility in Si and are slow diffusers such that they are immobile at the temperatures investigated, so that precipitation in the amorphous phase is very unlikely to occur. Thus the impurity profile remains the same before, during and after SPEG as Figure 2.20 (a) illustrates.

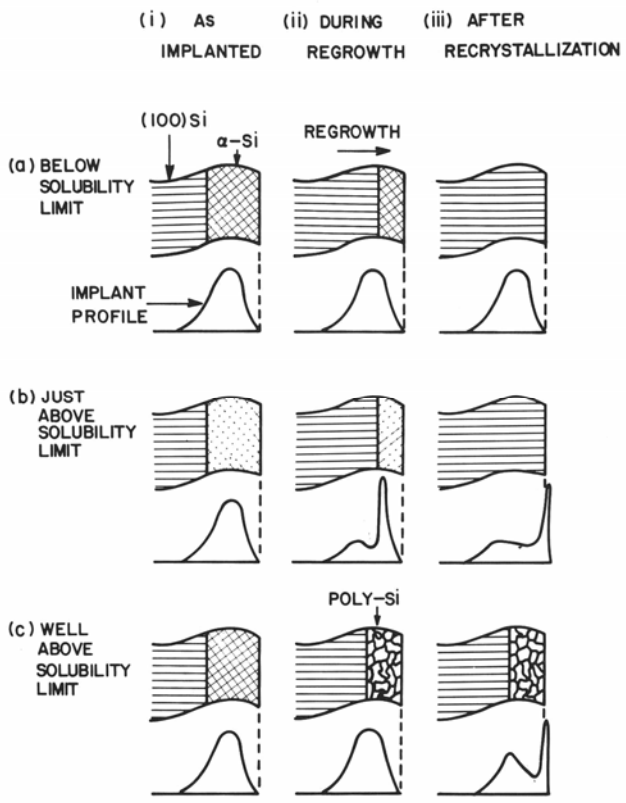

Figure 2.20: *Diagram from illustrating the typical a-layer re-growth sequence of (100) Si during anneals at temperatures ≤ 600˚C for three different impurity concentration regimes [85].*

However, once the solubility limit of the implant species is exceeded, the impurity begins to segregate at the moving c/a interface causing the observed retardation. This is known as "push-out" and leads to some of the impurity atoms residing at the surface with the remaining atoms occupying substitutional positions. This effect is illustrated for As implants just above the solubility limit in Figure 2.20 (b) For considerably higher concentrations of the impurity, the re-growth rate is sufficiently retarded such that complete re-crystallisation of the layer does not occur. Instead a polycrystalline surface structure is observed as is illustrated in Figure 2.20 (c) Segregation of the impurities at the c/a interface is assumed to promote nucleation of the polycrystalline Si. Once the polycrystalline Si is completely formed, the implanted impurities diffuse along the grain boundaries to the surface. The same concentration dependence and resultant defect structures are also observed for Na implanted a-layers [87].

Studies using channelling measurements [88] show that a compensating effect exists where the addition of equal concentrations of p-type and n-type dopants (group III and V elements) act to cancel out the enhanced re-growth rate, such that it is comparable with that of the un-doped material. In addition it was reported that the combination of implants of the same dopant type results in further SPEG enhancement. These findings indicate that electronic processes may be an influencing factor in the re-crystallisation of continuous amorphous layers [89].

Fe has also been found to enhance re-crystallisation [90]. In this case the authors attributed the observed "push-out" of Fe to the surface to the fact that the c/a interface releases the Fe which is otherwise trapped in the a-Si as Fe silicide complexes. It is theorised that these $FeSi_x$ complexes decompose upon interaction with the c/a interface [90].

Impurities such as oxygen, carbon and nitrogen at concentrations of 0.5at% have been found to retard the re-growth rate by an order of magnitude [66]. Channelling effect measurements were made on O implanted a-layers. Contrary to the group III and V implants, the re-growth rate increased as the O concentration decreased towards the surface, showing the inverse relationship between impurity concentration and re-growth rate. Such impurities are known as fast diffusers as they are mobile in c-Si at SPEG temperatures. It is believed therefore that their mobility in a-Si is similar, thus precipitation in the a-layer is achievable at the low concentrations described here.

The heavier noble gases such as argon, krypton, neon and xenon have also been found to retard the re-crystallisation of a-layers. In this case it is believed that the presence of gas bubbles slows down re-crystallisation, as the solubility of these gases in c-Si is known to be low and so the gas is retained at these temperatures. In some cases the concentration of the bubbles is such that complete re-crystallisation is unachievable, and instead a layer of polycrystalline material is produced. This was demonstrated in a TEM study where room temperature implants of $6x10^{15}$ Ne ions/cm^2, $2x10^{15}$ Ar ions/cm^2 and $6x10^{14}$ Kr

ions/cm^2 were found to produce continuous amorphous layers which extended to the surface [65]. However upon annealing of these layers, all three samples contained polycrystalline layers. Reduction of the implanted fluences to 2x10^{15} Ne ions/cm^2 and 6x10^{14} Ar ions/cm^2 however achieved complete re-crystallisation of the layers [65]. All of the samples were annealed at 1100°C for 30mins and the experiments were carried out on both (100) and (111) Si. Above a fluence of about 6x10^{15} Ar ions/cm^2 the resultant defect structures, as indicated by RBS, were found to be similar for both orientations and gas bubbles were observed by TEM in all the annealed samples. The high concentrations of gas in the layers were purported to lead to the occurrence of bonding mistakes made during SPEG, which led to the production of microtwins and a polycrystalline Si surface layer. In addition to this, layers formed by Ne were found to re-crystallise with fewer defects of this type than Ar implanted layers. The authors ascribed this to the fact that Ar is a larger atom and thus has greater associated lattice strain, which in turn promotes an increase in lattice bonding errors [65].

The idea that gas bubbles promote the production of microtwins was further investigated, again using TEM, by Revesz *et al* who produced surface a-layers by Ar implantation into (100) Si at LN_2 temperature [63]. Figure 2.21 illustrates their proposed model of microtwin nucleation. They believed that a large Ar bubble residing at the c/a interface causes de-coupling of the two phases, thus the atoms in the amorphous phase are unable to map onto those in the crystalline phase. This local effect allows for misorientated crystal re-growth; i.e. the formation of a microtwin. This model was in agreement with another similar study using Ne and Kr implanted layers [64]. However, as will be described in Chapters 4 and 5, this model cannot be used to explain the results presented therein, as *in situ* TEM images show unequivocally microtwin nucleation where there are no bubbles, in (100) orientated Si.

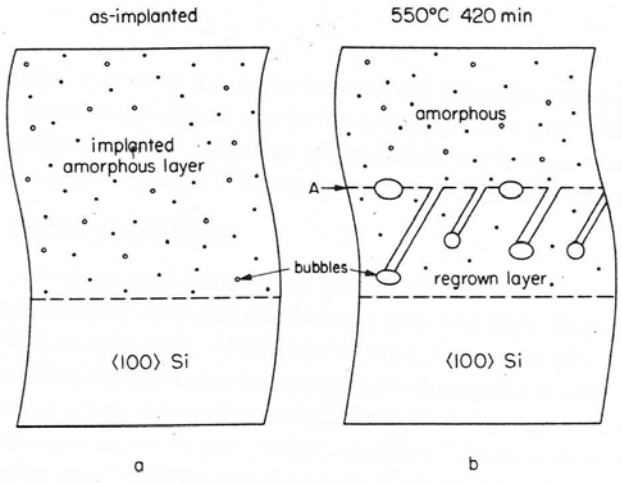

Figure 2.21: *Diagram illustrating the microtwin nucleation model as proposed by Revesz et al [62]. Microtwin nucleation occurs exclusively at the surface of large bubbles as is depicted in (b).*

As is now evident, the SPEG of a-layers in Si is an extremely complex affair. It is no surprise therefore that several atomistic models to describe this process exist. The following describes these models, paying special attention to theories proposed for the production of microtwins in (111) orientated Si.

2.9 Models of SPEG

Over the past 30 years several models have been proposed in order to explain the SPEG process and the dependence of substrate orientation and impurities on the re-growth rate. Initially a very simple model was described by Spaepen [91] where re-crystallisation occurred via the breaking and re-arrangement of bonds at the a/c interface. This idea was further developed by Csepregi *et al* [81] who attempted to incorporate the substrate orientation dependence into their model. Epitaxial growth was only envisaged to proceed once at least two undistorted bonds had been formed by an atom at the c/a interface with atoms in the crystalline matrix. This was thought to occur again via a bond-breaking mechanism. Due to the necessity for at least two undistorted bonds to be produced, re-growth along the <111> direction should not occur as alternate planes only contain one bond in this direction [81]. The authors therefore proposed that nucleation and growth of atomic clusters must occur on (111) interfaces, resulting in an irregular interface and the formation of microtwins.

They also suggested that microtwins are the cause of the increased c/a interface velocity observed for (111) Si, which has been discussed previously. This model however does not discuss the difference in growth rate observed in (110) Si, nor integrate the effect of dopants on SPEG.

Drosd and Washburn [92] developed a model which explains the growth rates observed for all three of the major axis in Si, as well as describing in greater detail the production of microtwins on (111) interfaces and their observed a-symmetrical growth during SPEG. As for the Csepregi model, for an atom to be considered to belong to the crystalline phase it must make two undistorted bonds with that phase at the a/c interface. Once this has occurred, epitaxial growth can proceed. Single atoms or groups of atoms therefore need to reorient in order to meet this criterion. Figure 2.22 taken from [92] illustrates how this is achieved for each of the three major crystallographic planes.

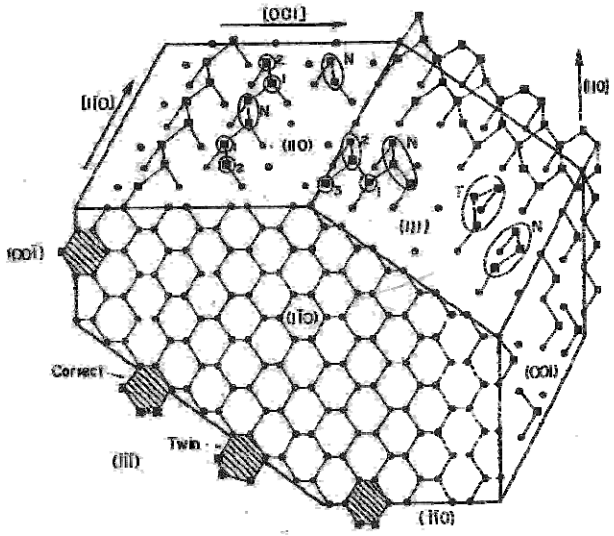

Figure 2.22: *Diagram taken from Drosd and Washburn [91] illustrating, for each of the three major crystallographic orientations in Si, the way in which bonds are required to re-orientate and form with one another in order for SPEG to proceed.*

On the (001) surface described in this diagram, only one atom is required to form two undistorted bonds and so SPEG is expected to progress relatively easily. As microtwins are the result of mistakes in the stacking sequence of the re-crystallising Si, this model clearly demonstrates that such mistakes are not

possible on {100} surfaces and hence microtwin nucleation is not expected in this case. On {110} surfaces, a cluster of two atoms is required for SPEG to proceed, where one atom in the cluster forms a bond with the other atom in the cluster as well as with an atom in the crystalline material. Once this cluster has formed, expansion of this surface occurs by the addition of one extra atom to another cluster. This process results in the formation of linear chains of atoms on the surface, propagating in the <110> direction [92]. The situation is further complicated for {111} surfaces, where as is illustrated in Figure 2.22, 3 atoms are required in order to form two undistorted bonds with the crystalline matrix. Labelled "N" in the diagram, these surface clusters are the nuclei for further atomic bonding. Expansion in this plane can therefore occur by the attachment of a single atom followed by a two atom cluster on to each nucleus, resulting in the formation of chains of atoms which can propagate in a variety of directions [92]. The three atom cluster can bond to the crystal in two different ways. If the situation labelled "T" in the diagram occurs then a reverse in the stacking sequence takes place, leading to the formation of a microtwin. This is further illustrated by the hatched hexagons in the lower part of the diagram.

This model can also account for the bi-linear nature of the re-growth rate associated with (111) orientated Si, where the formation of microtwins is shown to accelerate re-crystallisation [81]. The c/a interface has been observed by TEM to consist of small undulations of about 50Å due to the amorphisation process [92, 93]. These undulations in (111) Si allow for the addition of single atoms or clusters of two atoms to the matrix in order for re-growth to proceed. Because the interface motion is bounded by the slower re-growing <111> direction, after sufficient re-growth the c/a interface will contain mainly (111) surfaces allowing for microtwin nucleation to occur. It is at this point that an increase in growth rate is observed to occur [83]. Figure 2.23 illustrates the situation which can transpire once a microtwin has penetrated the amorphous material. It demonstrates clearly that contrary to the three atom clusters required for nucleation on a normal (111) surface, the inclined nature of the microtwin surface to the (111) plane allows for re-crystallisation to occur via the bonding of just two atoms to the matrix.

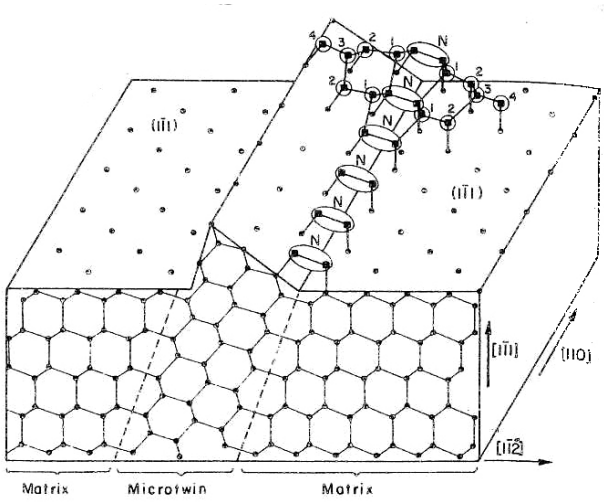

Figure 2.23: *Diagram taken from Csepregi [82] illustrating that, once a microtwin has penetrated the amorphous material, the inclined nature of the microtwin surface to the (111) plane allows for re-crystallisation to occur via the bonding of just two atoms to the matrix, ultimately resulting in enhanced re-growth rate on that side. The opposite side of the microtwin grows at a slower rate.*

As a consequence of this nucleation step, only one other atom in the amorphous material is required to form two more undistorted bonds with the crystal and thus linear chains of atoms are easily produced, propagating in the <112> direction, resulting in the enhanced growth rate observed. On the opposite surface of the inclined microtwin, a cluster of two atoms, then another single atom is necessary for the required undistorted bonding to the crystal to be achieved. This side therefore grows at a slower rate compared to the other side of the microtwin.

TEM experiments such as those carried out in [92] and during other studies [93] have revealed that microtwins increase in thickness exclusively on one side, whilst the other side possess a planar interface between it and the rest of the matrix. The increase in thickness and enhanced growth rate are illustrated in Figure 2.24 taken from [92].

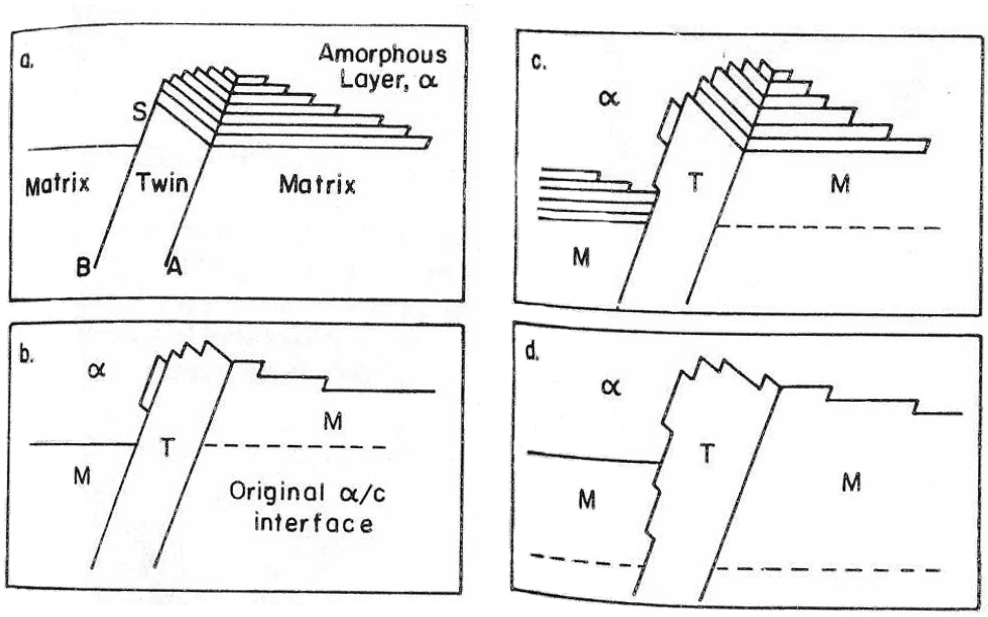

Figure 2.24: *Diagram, illustrating the a-symmetric nature of microtwin growth [91].*

Re-growth on the slower growing side can only occur by nucleation of new atomic layers [92] leading to the observed thickness increase. The increase in growth rate on the other side is that which is observed in the second part of the bi-linear curve. The activation energy for SPEG following on from this model was proposed to be due to the re-orientation of small groups of atoms at the c/a interface.

The effect of impurities on the SPEG rate was modelled by Narayan [93], who investigated experimentally, using TEM, the production of microtwins in (100) Si as a consequence of excessive concentrations of impurities. In this situation, crystallisation is assumed to occur by diffusion of the impurities and Si interstitials in the amorphous phase followed by their local rearrangement to complete a hexaring at the c/a interface. Critical substitutional concentrations of a variety of impurities were determined, above which the (100) c/a interface becomes non-planar, resulting in the development of {111} facets onto which twins are formed [93]. In this model, the interface velocity is related to the diffusivity of interstitials in the amorphous layer near the c/a interface, where an enhancement of their diffusion results in an increased SPEG rate. The diffusivity of Si interstitials is strongly affected by electrically active impurities at high

concentrations, where an enhanced diffusion has been found in heavily doped p- and n-type Si.

At the maximum concentration with which dopants can be incorporated into substitutional sites, the interface velocity is zero. However diffusion of dopants in the amorphous material still occurs according to this model, leading to their clustering and precipitation at the c/a interface. The interface in between the precipitates is then able to progress, resulting in a non-planar re-growth [93]. {111} facets are formed at this undulating interface leading to the production of microtwins in the same way as described by Drosd and Washburn.

An alternative approach to the effect of dopants on the SPEG rate was devised by Williams and Elliman [89] who speculated that the mass transport of defects was not occurring. Again a bond-breaking process at the c/a interface was envisaged, where kinks were formed on [110] ledges. Such a situation is described in Figure 2.25, taken from [89].

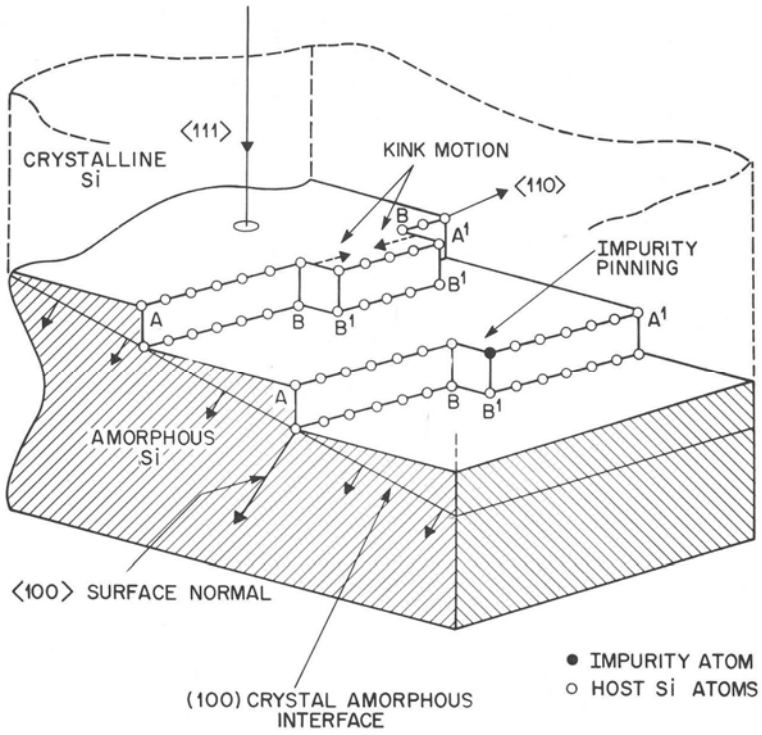

Figure 2.25: *Diagram illustrating SPEG via the movement of kinks, as proposed by Williams and Elliman [88].*

Once a kink is formed, re-crystallisation occurs via the growth of the kink along its ledge. On {111} surfaces, re-growth occurs in this way because an atom in the amorphous material forms two undistorted bonds with an adjacent atom on a ledge in the crystalline material allowing for SPEG to proceed, which is unlike the usual three bonds required for [111] re-growth. The Si bonds at the kink-sites are believed to be strained and thus introduce electronic energy levels into the Si band gap. The dopants and other defects also have associated electronic energy levels in the Si band gap, which results in an alteration in the Fermi level. The band structure of doped a-Si is therefore different to that of doped c-Si. Because of this difference, band bending at the c/a interface occurs. From this the associated defect related energy levels at the interface were deduced, which when incorporated into equations allowed for the determination of the c/a interface velocity for n- and p-type dopants with different concentrations.

Various molecular dynamics simulations [94, 95] have also utilised the kink model in order to describe SPEG processes, where some authors believe that di-vacancies or di-interstitials are responsible for re-crystallisation.

Results from recent studies have suggested that the I-V pair is the defect responsible for re-crystallisation. Results from MD simulations [96] have shown that the stability of agglomerates of I-V pairs is related to the number of neighbouring I-V pairs, thus larger clusters are more stable with the recombination rate decreasing as the number of neighbouring I-V pairs increases. Figure 2.26 is a simulation of various I-V pairs in different environments, where isolated I-V pairs (A) are the first to annihilate. It was found that, as re-crystallisation occurs at c/a interfaces, the outer I-V pairs re-combine initially, and large round amorphous pockets (B and C) shrink. This model also can be used to describe SPEG. If an I-V pair re-combines at the surface then those neighbouring it (D and E) will re-crystallise faster, due to the deficit in one surrounding I-V pair. This continues until the whole layer has re-crystallised [4].

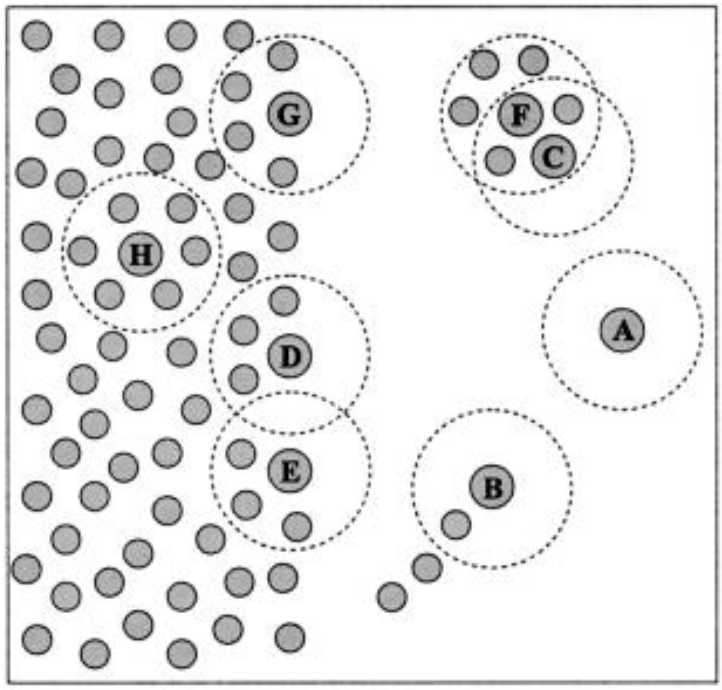

Figure 2.26: *Simulation showing the possible mechanisms by which I-V pairs may re-combine [5].*

As for the amorphisation models, the nature of the defect or defects which are responsible for the observed thermal activation energies of SPEG and thus the precise processes involved is as yet not unanimously decided.

2.10 References

1. Bonafos, C., Alquier, D., Martinez, A., Mathiot, D., and Claverie, A. *TED of boron in the presence of EOR defects: the use of the theory of Ostwald ripening to calculate Si-interstitial supersaturation in the vicinity of extrinsic defects.* Nuclear Instruments and Methods in Physics Research Section B: Beam Interactions with Materials and Atoms, 1996. **112**(1-4): p.129-132.
2. Nastasi, M., Mayer, J.W., and Hirvonen, J.K., *Ion-solid interaction: fundamentals and applications*. Cambridge solid state science series, ed. D.R. Clarke, S. Suresh, and I.M. Ward. 1996, Cambridge: Cambridge University Press.
3. Gibbons, J.F. Proceedings of the IEEE 1972. **60**: p.1062.
4. Pelaz, L., Marques, L.A., and Barbolla, J. *Ion-beam-induced amorphization and recrystallization in silicon.* Journal of Applied Physics, 2004. **96**(11): p.5947-5976.
5. Kinchin, G.H. and Pease, R.S. *The Displacement of Atoms in Solids by Radiation.* Reports on Progress in Physics, 1955. **18**: p.1-51.
6. Brinkman, J.A. *Production of atomic displacements by high-energy particles.* American Journal of Physics, 1956. **24**: p.246.
7. Donnelly, S.E. and Birtcher, R.C. *Ion-induced spike effects on metal surfaces.* Philosophical Magazine a-Physics of Condensed Matter Structure Defects and Mechanical Properties, 1999. **79**(1): p.133-145.
8. Ziegler, J.F. *Srim-2003.* Nuclear Instruments & Methods in Physics Research Section B-Beam Interactions with Materials and Atoms, 2004. **219-20**: p.1027-1036.
9. Edmondson, P.E., *An in-situ TEM study of the formation and annealing of the damage resulting from single ion impacts in crystalline silicon.* 2006, Universtiy of Salford.
10. Giles, J.M. *Transient Phosphorus Diffusion Below the Amorphization Threshold.* Journal of Electrochemical Society, 1991. **138**: p.1160.
11. Kittel, C., *Introduction to Solid State Physics*. 1996, New York: John Wiley and Sons.

12. Bonafos, C., Omri, M., deMauduit, B., BenAssayag, G., Claverie, A., Alquier, D., Martinez, A., and Mathiot, D. *Transient enhanced diffusion of boron in presence of end-of-range defects.* Journal of Applied Physics, 1997. **82**(6): p.2855-2861.
13. Roth, E.G., Holland, O.W., and Thomas, D.K. *Control of diffusion of implanted boron in preamorphized Si: Elimination of interstitial defects at the amorphous-crystal interface.* Applied Physics Letters, 1999. **74**(5): p.679-681.
14. Pichler, P., *Intrinsic point defects, impurities, and their diffusion in silicon.* 2004, New York: SpringerWien.
15. Watkins, G.D. *Intrinsic defects in silicon.* Materials Science in Semiconductor Processing, 2000. **3**(4): p.227-235.
16. Cerofolini, G.F., Corni, F., Frabboni, S., Nobili, C., Ottaviani, G., and Tonini, R. *Hydrogen and helium bubbles in silicon.* Materials Science and Engineering 2000. **27**: p.1-52.
17. Raineri, V., Coffa, S., Szilagyi, E., Gyulai, J., and Rimini, E. *He-vacancy interactions in Si and their influence on bubble formation and evolution.* Physical Review B, 2000. **61**(2): p.937-945.
18. Hastings, J.L., Estreicher, S.K., and Fedders, P.A. *Vacancy aggregates in silicon.* Physical Review B, 1997. **56**: p.10215.
19. Schreutelkamp, R.J., Custer, J.S., Liefting, J.R., Lu, W.X., and Saris, F.W. *Pre-Amorphization Damage in Ion-Implanted Silicon.* Materials Science Reports, 1991. **6**(7-8): p.275-366.
20. Libertino, S., Coffa, S., and La Magna, A. *Room temperature defect diffusion in ion implanted c-Si.* Nuclear Instruments and Methods in Physics Research Section B: Beam Interactions with Materials and Atoms, 2002. **186**(1-4): p.265-270.
21. Richie, D.A., Kim, J., Barr, S.A., Hazzard, K.R.A., Hennig, R., and Wilkins, J.W. *Complexity of small silicon self-interstitial defects.* Physical Review Letters, 2004. **92**(4)
22. Arai, N., Takeda, S., and Kohyama, M. *Self-Interstitial Clustering in Crystalline Silicon.* Physical Review Letters, 1997. **78**: p.4265.

23. Libertino, S., Coffa, S., and Benton, J.L. *Formation, evolution, and annihilation of interstitial clusters in ion-implanted Si.* Physical Review B, 2001. **6319**(19)

24. Benton, J.L., Halliburton, K., Libertino, S., Eaglesham, D.J., and Coffa, S. *Electrical signatures and thermal stability of interstitial clusters in ion implanted Si.* Journal of Applied Physics, 1998. **84**: p.4749.

25. Claverie, A., Colombeau, B., De Mauduit, B., Bonafos, C., Hebras, X., Ben Assayag, G., and Cristiano, F. *Extended defects in Shallow implants.* Appl. Phys. A, 2003. **76**: p.1025-1033.

26. Claverie, A., Colombeau, B., Cristiano, F., Altibelli, A., and Bonafos, C. *Modeling of the Ostwald ripening of extrinsic defects and transient enhanced diffusion in silicon.* Nuclear Instruments and Methods in Physics Research Section B: Beam Interactions with Materials and Atoms, 2002. **186**(1-4): p.281-286.

27. Tang, M., Colombo, L., J.Zhu, and Rubia., T.D.d.l. *Intrinsic point defects in crystalline silicon: Tight-binding molecular dynamics studiesof self-diffusion, interstitial-vacancy recombination, and formation volumes* Physical Review B, 1997. **55**: p.14279.

28. Cargnoni, F., C Gatti, and Colombo, L. *Formation and annihilation of a bond defect in silicon: An ab initio quantum-mechanical characterization.* Physical Review B, 1998. **57**: p.170.

29. Polk, D.E. and Boudreaux, D.S. *Tetrahedrally coordinated Random-Network Structure.* Physical Review Letters, 1973. **31**: p.92.

30. Lee, I.-H. and Chang, K.J. *Atomic and electronic structure of amorphous Si from first-pronciples molecular-dynamics simulations.* Physical Review B, 1994. **50**: p.18083.

31. Zdetsis, A. and Froudakis, G. *Energetics and structure of dangling and floating bonds in amorphous silicon.* Journal of Non-Crystalline Solids, 1991. **137 and 138**: p.303-306.

32. Pantelides, S.T. *Defects in Amorphous-Silicon - a New Perspective.* Physical Review Letters, 1986. **57**(23): p.2979-2982.

33. Uda, T. *Atomic-Structure of Amorphous-Silicon.* Solid State Communications, 1987. **64**(5): p.837-841.

34. Pantelides, S.T. *Native defects and diffusion in amorphous silicon - a revisit.* Solid State Communications, 1992. **84**: p.221-225.

35. Kugler, S., Kohary, K., Kadas, K., and Pusztai, L. *Small bond angles in amorphous silicon: are they a new type of defect?* Journal of Non-Crystalline Solids, 2004. **338-340**: p.425-429.

36. Hoven, G.N.v.d., Liang, Z.N., Niesen, L., and Custer, J.S. *Evidence for vacancies in amorphous silicon.* Physical Review Letters, 1992. **68**: p.3714.

37. Coffa, S., Priolo, F., and Battaglia, A. *Defect production and annealing in ion-implanted amorphous silicon.* Physical Review Letters, 1992. **70**: p.3756.

38. Brodsky, M.H., Title, R.S., Weiser, K., and Pettit, G.D. *Structural, Optical, and Electrical Properties of Amorphous Silicon Films.* Physical Review B, 1970. **1**: p.2632.

39. Sinke, W.C. and Roorda, S. *Aspects of Silicon Crystallization.* Journal of Crystal Growth, 1990. **99**(1-4): p.222-228.

40. Roorda, S., Sinke, W.C., Poate, J.M., Jacobson, D.C., Dierker, S., Dennis, B.S., Eaglesham, D.J., Spaepen, F., and Fuoss, P. *Structural Relaxation and Defect Annihilation in Pure Amorphous-Silicon.* Physical Review B, 1991. **44**(8): p.3702-3725.

41. Polman, A., Jacobson, D.C., Coffa, S., Poate, J.M., Roorda, S., and Sinke, W.C. *Defect States of Amorphous Si Probed by the Diffusion and Solubility of Cu.* Applied Physics Letters, 1990. **57**(12): p.1230-1232.

42. Coffa, S., Poate, J.M., Jacobson, D.C., and Polman, A. *Impurity Trapping and Gettering in Amorphous-Silicon.* Applied Physics Letters, 1991. **58**(25): p.2916-2918.

43. J. S. Williams, K. T. Short, R. G. Elliman, M. C. Ridgway, and Goldberg, R. *Ion-beam-induced amorphization and dynamic annealing processes in silicon.* nuclear Instruments & Methods in Physics Research Section B-Beam Interactions with Materials and Atoms, 1990. **48**: p.431.

44. Prussin, S., Margolese, D.I., and Tauber, R.N. *Formation of Amorphous Layers by Ion-Implantation.* Journal of Applied Physics, 1985. **57**(2): p.180-185.

45. Motooka, T. *The role of defects during amorphization and crystallization processes in ion implanted Si.* Materials Science and Engineering A, 1998. **253**: p.42-49.

46. Jr, F.F.M. and Crowder, B.L. Radiation effects, 1970. **6**: p.27.

47. Howe, L.M. and Rainville, M.H. *Features of collision cascades in silicon as determined by transmission electron microscopy.* Nuclear Instruments and Methods, 1981. **182-183**(Part 1): p.143-151.

48. Howe, L.M. and Rainville, M.H. *Heavy ion damage in silicon and germanium.* Nuclear Instruments and Methods in Physics Research Section B: Beam Interactions with Materials and Atoms, 1987. **19-20**(Part 1): p.61-66.

49. R. D Goldberg, J. S Williams, and Elliman, R.G. Mater. Res. Soc. Symp. Proc, 1994. **316**: p.259.

50. Goldberg, R.D., Williams, J.S., and Elliman, R.G. *Amorphization of silicon by elevated temperature ion irradiation.* Nuclear Instruments and Methods in Physics Research Section B: Beam Interactions with Materials and Atoms, 1995. **106**(1-4): p.242-247.

51. D.M. Stock, B. Webber, and Gartner, K. *Role of the bond defect for structural transformations between crystalline and amorphous silicon:A molecular-dynamics study.* Physical Review B, 2000. **61**: p.8150.

52. Marques, L.A., Pelaz, L., Hernandez, J., Barbolla, J., and Gilmer, G.H. *Stability of defects in crystalline silicon and their role in amorphization.* Physical Review B, 2001. **6404**(4)

53. Jones, K.S., Prussin, S., and Weber, E.R. *A Systematic Analysis of Defects in Ion-Implanted Silicon.* Applied Physics a-Materials Science & Processing, 1988. **45**(1): p.1-34.

54. Seshan, K. and J. Washburn Radiation effects, 1978. **37**: p.147.

55. Goldberg, R.D., Simpson, T.W., Mitchell, I.V., Simpson, P.J., Prikryl, M., and Weatherly, G.C. *Secondary defect formation in self-ion irradiated silicon.* Nuclear Instruments & Methods in Physics Research Section B-Beam Interactions with Materials and Atoms, 1995. **106**(1-4): p.216-221.

56. Cowern, N.E.B., Mannino, G., Stolk, P.A., Roozeboom, F., Huizing, H.G.A., van Berkum, J.G.M., Cristiano, F., Claverie, A., and Jaraiz, M. *Cluster*

ripening and transient enhanced diffusion in silicon. Materials Science in Semiconductor Processing, 1999. **2**(4): p.369-376.

57. Colombeau, B., Cowern, N.E.B., Cristiano, F., Calvo, P., Lamrani, Y., Cherkashin, N., Lampin, E., and Claverie, A. *Depth dependence of defect evolution and TED during annealing.* Nuclear Instruments and Methods in Physics Research Section B: Beam Interactions with Materials and Atoms, 2004. **216**: p.90-94.
58. Calvo, P., Claverie, A., Cherkashin, N., Colombeau, B., Lamrani, Y., de Mauduit, B., and Cristiano, F. *Thermal evolution of {1 1 3} defects in silicon: transformation against dissolution.* Nuclear Instruments and Methods in Physics Research Section B: Beam Interactions with Materials and Atoms, 2004. **216**: p.173-177.
59. Cristiano, F., Cherkashin, N., Hebras, X., Calvo, P., Lamrani, Y., Scheid, E., de Mauduit, B., Colombeau, B., Lerch, W., Paul, S., and Claverie, A. *Ion beam induced defects in crystalline silicon.* Nuclear Instruments and Methods in Physics Research Section B: Beam Interactions with Materials and Atoms, 2004. **216**: p.46-56.
60. Templier, C., *Inert gas bubbles in metals: A review*, in *Fundamental aspects of inert gases in solids*. 1990: Bonos France.
61. Trinkaus, H. and Singh, B.N. *Helium accumulation in metals during irradiation - where do we stand?* Journal of Nuclear Materials, 2003. **323**(2-3): p.229-242.
62. Donnelly, S.E. *Helium bubbles in implanted metals. A Critical Review.* Radiation effects, 1985. **90**: p.1 - 47.
63. Revesz, P., Wittmer, M., Roth, J., and Mayer, J.W. *Epitaxial Regrowth of Ar-Implanted Amorphous Silicon.* Journal of Applied Physics, 1978. **49**(10): p.5199-5206.
64. Wittmer, M., Roth, J., Revesz, P., and Mayer, J.W. *Epitaxial Regrowth of Ne-Implanted and Kr-Implanted Amorphous Silicon.* Journal of Applied Physics, 1978. **49**(10): p.5207-5212.
65. Cullis, A.G., Seidel, T.E., and Meek, R.L. *Comparative-Study of Annealed Neon-Ion, Argon-Ion, and Krypton-Ion Implantation Damage in Silicon.* Journal of Applied Physics, 1978. **49**(10): p.5188-5198.

66. Kennedy, E.F., Csepregi, L., Mayer, J.W., and Sigmon, T.W. *Influence of O-16, C-12, N-14, and Noble-Gases on Crystallization of Amorphous Si Layers.* Journal of Applied Physics, 1977. **48**(10): p.4241-4246.

67. Faraci, G., Pennisi, A.R., Terrasi, A., and Mobilio, S. *Xe bubbles in si observed by extended x-ray-absorption fine-structure spectroscopy.* Physical Review B, 1988. **38**(18): p.13468.

68. Oliviero, E., Peripolli, S., Fichtner, P.F.P., and Amaral, L. *Characterization of neon implantation damage in silicon.* Materials Science and Engineering B, 2004. **112**(2-3): p.111-115.

69. Oliviero, E., Peripolli, S., Amaral, L., Fichtner, P.F.P., Neaufort, M.F., FJ.F Barbot, and Donnelly, S.E. *Damage accumulation in neon implanted silicon.* Journal of Applied Physics, 2006. **043505**.

70. Fleischer, E.L. and Norton, M.G. *Noble gas inclusions in materials.* Heterogeneous Chemistry Reviews, 1996. **3**(3): p.171-201.

71. Mader, S. and Tu, K.N. *Microstructure of Xenon-Implanted Silicon.* Journal of Vacuum Science & Technology, 1975. **12**(1): p.501-503.

72. Elliman, R. Mater. Res. Soc. Symp. Proc, 1983. **27**: p.229.

73. Griffioen, C.C., Evans, J.H., Dejong, P.C., and Vanveen, A. *Helium Desorption Permeation from Bubbles in Silicon - a Novel Method of Void Production.* Nuclear Instruments & Methods in Physics Research Section B-Beam Interactions with Materials and Atoms, 1987. **27**(3): p.417-420.

74. Corni, F., Calzolari, G., Frabboni, S., Nobili, C., Ottaviani, G., Tonini, R., Cerofolini, G.F., Leone, D., Servidori, M., Brusa, R.S., Karwasz, G.P., Tiengo, N., and Zecca, A. *Helium-implanted silicon: A study of bubble precursors.* Journal of Applied Physics, 1999. **85**(3): p.1401-1408.

75. Pivac, B., Milat, O., Dubcek, P., Bernstorff, S., Corni, F., Nobili, C., and Tonini, R. *Early stages of bubble formation in helium-implanted (100)silicon.* Physica Status Solidi a-Applied Research, 2003. **198**(1): p.29-37.

76. Raineri, V., Saggio, M., and Rimini, E. *Voids in silicon by He implantation: From basic to applications.* Journal of Materials Research, 2000. **15**: p.1449.

77. Fichtner, P.F.P., Kaschny, J.R., Behar, M., Yankov, R.A., Mucklich, A., and Skorupa, W. *The effects of the annealing temperature on the formation of helium-filled structures in silicon.* Nuclear Instruments and Methods in Physics Research Section B: Beam Interactions with Materials and Atoms, 1999. **148**(1-4): p.329-333.

78. da Silva, D.L., Morschbacher, M.J., Fichtner, P.F.P., Oliviero, E., and Behar, M. *Formation of bubbles and extended defects in He implanted (1 0 0) Si at elevated temperatures.* Nuclear Instruments and Methods in Physics Research Section B: Beam Interactions with Materials and Atoms, 2004. **219-220**: p.713-717.

79. Beaufort, M.F., Donnelly, S.E., Rousselet, S., David, M.L., and Barbot, J.F. *Extended-type defects created by high temperature helium implantation into silicon.* Nuclear Instruments and Methods in Physics Research Section B: Beam Interactions with Materials and Atoms, 2006. **242**(1-2): p.565-567.

80. Oliviero, E., David, M.L., Fedorov, A.V., van Veen, A., Beaufort, M.F., and Barbot, J.F. *Helium implantation in silicon: the effects of implantation temperature.* Materials Science and Engineering B-Solid State Materials for Advanced Technology, 2003. **102**(1-3): p.222-227.

81. Csepregi, L., Kennedy, E.F., Mayer, J.W., and Sigmon, T.W. *Substrate-Orientation Dependence of Epitaxial Regrowth Rate from Si-Implanted Amorphous Sia.* Journal of Applied Physics, 1978. **49**(7): p.3906-3911.

82. Roth, J.A., Olson, G.L., Jacobson, D.C., and Poate, J.M. *Kinetics of solid phase epitaxy in thick amorphous Si layers formed by MeV ion implantation.* Applied Physics Letters, 1990. **57**: p.1340.

83. Csepregi, L., Mayer, J.W., and Sigmon, T.W. *Regrowth Behavior of Ion-Implanted Amorphous Layers on [111] Silicon.* Applied Physics Letters, 1976. **29**(2): p.92-93.

84. Csepregi, L., Kennedy, E.F., Gallagher, T.J., Mayer, J.W., and Sigmon, T.W. *Reordering of Amorphous Layers of Si Implanted with P-31, as-75, and B-11 Ions.* Journal of Applied Physics, 1977. **48**(10): p.4234-4240.

85. Ruffell, S., Mitchell, I.V., and Simpson, P.J. *Solid phase epitaxial regrowth of amorphous layers in silicon created by low energy phosphorus*

implantation: A medium energy ion scattering study. Nuclear Instruments & Methods in Physics Research Section B-Beam Interactions with Materials and Atoms, 2006. **242**(1-2): p.591-594.

86. Williams, J.S. and Poate, J.M., *Ion Implantation and Beam Processing*. 1984: Academic Press.
87. Wang, W.H., Bolse, W., Illgner, C., Lieb, K.P., Keinonen, J., and Ewert, J.C. *Recrystallization and diffusion in sodium-implanted silicon.* Thin Solid Films, 1997. **295**(1-2): p.169-177.
88. Suni Applied Physics Letters, 1982. **40**(3).
89. Williams, J.S. and Elliman, R.G. *Role of Electronic Processes in Epitaxial Recrystallization of Amorphous-Semiconductors.* Physical Review Letters, 1983. **51**(12): p.1069-1072.
90. de Souza, J.P., Amaral, L., and Fichtner, P.F.P. *Recrystallization behavior of silicon implanted with iron.* Journal of Applied Physics, 1992. **71**(11): p.5423-5426.
91. Spaepen, F. *Structural Model for Interface between Amorphous and Crystalline Si or Ge.* Acta Metallurgica, 1978. **26**(7): p.1167-1177.
92. Drosd, R. and Washburn, J. *Some Observations on the Amorphous to Crystalline Transformation in Silicon.* Journal of Applied Physics, 1982. **53**(1): p.397-403.
93. Narayan, J. *Interface Structures during Solid-Phase-Epitaxial Growth in Ion-Implanted Semiconductors and a Crystallization Model.* Journal of Applied Physics, 1982. **53**(12): p.8607-8614.
94. Weber, B., Stock, D.M., and Gartner, K. *Defect-related growth processes at an amorphous/crystalline interface: a molecular dynamics study.* Materials Science and Engineering B-Solid State Materials for Advanced Technology, 2000. **71**: p.213-218.
95. Motooka, T. *The role of defects during amorphization and crystallization processes in ion implanted Si.* Materials Science and Engineering a-Structural Materials Properties Microstructure and Processing, 1998. **253**(1-2): p.42-49.

96. Pelaz, L., Marques, L.A., Aboy, M., Barbolla, J., and Gilmer, G.H. *Atomistic modeling of amorphization and recrystallization in silicon.* Applied Physics Letters, 2003. **82**(13): p.2038-2040.

Chapter 3

Experimental Techniques

3.1 Introduction

This research project is concerned with the investigation of the formation of, and interactions between, radiation induced defects of different types in Si during thermal annealing. Cross-sectional transmission electron microscopy (XTEM) was the principal analytical technique used throughout the course of this study. TEM is an extremely powerful tool for the characterisation and analysis of radiation induced defects, which in this study were produced in Si by ion implantation and subsequent thermal treatments. TEM is performed using an accelerated electron beam focused by a series of magnetic lenses onto a thin specimen. The electrons are scattered by the atoms in the specimen and then focused by more magnetic lenses onto a fluorescent screen, a digital imaging system or a photographic negative. Altering the strength of the second set of lenses results in either an image or diffraction pattern being recorded on the screen, both of which contains important structural information about the specimen. Due to the importance of the TEM in this study, a concise account of its components, operation and theory of operation are given in this chapter.

The resolution of the final image is improved by the use of thin specimens, as this reduces the inelastic scattering of electrons by the atoms in the material. For example, when investigating Si, it is preferable to produce samples which are less than 100nm thick when imaging with 200keV electrons. Various preparation methods may be employed to produce such “electron transparent” specimens. The most common of these is ion beam milling (IBM), which involves bombarding the specimen with energetic argon ions to sputter away material. Other techniques include chemical polishing; cleaving of the material along specific crystallographic planes; or simply cutting the sample with a knife. The technique which is chosen depends on the type of material to be thinned and the structures which are to be investigated, as the technique itself may alter the structure of the material and the defects therein. Following an analysis of the effects of two of these techniques on the type of samples investigated throughout this study, IBM techniques were deemed the most suitable. This investigation and its results are detailed in Section 3.3.6.

This chapter describes all the techniques used in the production and preparation of the samples investigated in this study, as well as the theory behind the TEM analysis of the defect structures produced.

3.2 Specimen production

All the experiments in this study were performed on *p-type* (boron doped) (100) Si with a resistivity between 1-10 Ω cm^{-1}. The Si wafers used were between 400 and 1000 microns thick and were cut into pieces of a few cm^2. When a process is performed on samples of these dimensions, i.e. before any thinning for TEM has taken place, the sample is referred to as being "in the bulk". Facilities at the University of Salford, England, the Universidade Federai do Rio Grande do Sul (UFRGS) in Brazil, and at the Laboratoire de Métallurgie Physique in Poitiers, France, were utilised throughout this study. At UFRGS, Si samples were implanted with either Xe or Li, thermally annealed in the bulk, and analysed using Rutherford Backscattering Spectroscopy (RBS). In Poitiers, Si samples were implanted with either Xe or He, thinned using IBM, and analysed using either a JEOL 200CX, JEOL 3010 or JEOL 2200 TEM. In addition, these and some of the samples implanted at UFRGS were thermally annealed in the bulk and during *in-situ* TEM analysis at this facility. Thermal annealing, both in the bulk and during *in-situ* TEM experiments, TEM specimen preparation using IBM, analysis using RBS, and investigations using either a JEOL 200CX or JEOL 3010 TEM, were conducted at the University of Salford. For clarity, table 1 shows the principle operations undertaken at each of these facilities in producing all the samples investigated during this study.

Salford	UFRGS	Poitiers

Implantation species and conditions				Bulk thermal anneal	Analysis	
Xe	450keV	RT	$1x10^{16}$ ions/cm^2	No	TEM	
Xe	250keV	350°C	$5x10^{16}$ ions/cm^2	No	TEM	
Xe	250keV	350°C	$5x10^{16}$ ions/cm^2	600°C for 30 mins	TEM	
Xe	250keV	350°C	$5x10^{16}$ ions/cm^2	800°C for 30 mins	TEM	
Xe	250keV	350°C	$2x10^{16}$ ions/cm^2	No	TEM	
Xe	250keV	350°C	$2x10^{16}$ ions/cm^2	600°C for 30 mins	TEM	
Xe	250keV	350°C	$2x10^{16}$ ions/cm^2	800°C for 30 mins	TEM	
Xe	250keV	350°C	$1x10^{16}$ ions/cm^2	No	TEM	
Xe	250keV	350°C	$1x10^{16}$ ions/cm^2	600°C for 30 mins	TEM	
Xe	250keV	350°C	$1x10^{16}$ ions/cm^2	800°C for 30 mins	TEM	
Xe	250keV	350°C	$5x10^{15}$ ions/cm^2	No	TEM	
Xe	250keV	350°C	$5x10^{15}$ ions/cm^2	600°C for 30 mins	TEM	
Xe	250keV	350°C	$5x10^{15}$ ions/cm^2	800°C for 30 mins	TEM	
Xe	250keV	350°C	$1x10^{16}$ ions/cm^2	No	TEM	
Xe	250keV	350°C	$1x10^{16}$ ions/cm^2	800°C for 30 mins	TEM / HRTEM / Z-contrast	
Xe	250keV	350°C	$5x10^{15}$ ions/cm^2	No	TEM	
Xe	250keV	350°C	$5x10^{15}$ ions/cm^2	800°C for 30 mins	TEM	
Li	150keV	LN_2	$7x10^{15}$ ions/cm^2	No	RBS	TEM
Li	150keV	LN_2	$7x10^{15}$ ions/cm^2	600°C for 30 mins	TEM	
Li	150keV	LN_2	$7x10^{15}$ ions/cm^2	400°C for 30 mins	TEM	TEM
(Li)(400°C) He	80keV	RT	$2.5x10^{16}$ ions/cm^2	No	TEM	TEM
(Li) He	80keV	RT	$2.5x10^{16}$ ions/cm^2	600°C for 30 mins	TEM	TEM
(Li)(400°C) He	80keV	RT	$2.5x10^{16}$ ions/cm^2	No	*in-situ:* up to 665°C for 1 hour	*in-situ:* up to 665°C for 1 hour
(Li)(400°C) He	80keV	RT	$5x10^{15}$ ions/cm^2	No	TEM	
(Li)(400°C) He	80keV	RT	$5x10^{15}$ ions/cm^2	600°C for 30 mins	TEM	
He	80keV	RT	$2.5x10^{16}$ ions/cm^2	1000°C for 30 mins	None	
(He)Li	150keV	LN_2	$7x10^{15}$ ions/cm^2	No	TEM	
(He)Li	150keV	LN_2	$7x10^{15}$ ions/cm^2	600°C for 30 mins	TEM	

Table 1.1: *This table gives the complete implantation, annealing and analysis information of the samples investigated in this study. The left hand column shows the ion species with which the Si samples were implanted. Some experiments required several implantation and annealing stages. For example, in one experiment, Si was implanted with Li at 70K and then annealed at 400°C for 30mins. The sample was then re-implanted with He at 300K. The species and temperature in parenthesis therefore define those of the initial implantation. The different colours indicate where each operation was performed with the key given at the top of the table.*

At the UFRGS, the bulk pieces of Si were implanted with 250keV Xe ions, at a temperature of 350ºC and with a fluence of either $5x10^{15}$, $1x10^{16}$, $2x10^{16}$ or $5x10^{16}$ Xe ions/cm^2. Other pieces were implanted with $7x10^{15}$ Li ions/cm^2 at liquid nitrogen temperature (70K) and with energy of 150keV. These latter samples were then re-implanted at the Laboratoire de Métallurgie Physique with 80keV He ions at room temperature (300K) and with a fluence of either $5x10^{15}$ or $2.5x10^{16}$ He ions/cm^2. Xe implantations were also carried out in Poitiers, in order to check and verify the results obtained from the samples implanted in UFRGS.

The types of damage produced by these implantations can be recovered by heating the samples to temperatures of about 400 - 1000ºC, for a few tens of minutes to several hours. In this investigation, the bulk samples were contained in an evacuated (about 10^{-7} torr) quartz tube in order to limit the diffusion of foreign atoms into the material during annealing. This tube was inserted into a furnace which was already at the required temperature. For the damage recovery specific to this investigation, samples were annealed in this way for 30 minutes, or in one case for 1 hour, using a ramp furnace either in the Laboratoire de Métallurgie Physique or at the University of Salford.

3.3 TEM Specimen Preparation Methods

The TEMs used in this study were operated using accelerating voltages of 200 or 300keV. These voltages require specimen thicknesses to be approximately 100nm or less for optimal imaging. Such specimen thicknesses may be produced using one of a variety of preparation techniques available. Unfortunately, damage is produced as a consequence of many of these techniques. It is essential that this damage is kept to a minimum, and in-depth knowledge of how this damage has affected the specimen is required. As previously mentioned, IBM techniques were used during this study. A comparison of this type of method with one which utilises crystallographic cleavage planes, known as the small angled cleavage technique (SACT), found that IBM techniques alter the morphology of small (~2nm radius) near-surface bubbles in silicon [2]. These results suggest that all small radiation induced, near-surface defects may be subjected to the same perturbation and this must be taken into consideration during any defect

analysis. This perturbation and the damage introduced due to these techniques will be discussed further in Sections 3.3.5 and 3.3.6. An advantage to IBM techniques is that they produce TEM specimens with relatively large areas of useful electron transparency, compared to those produced using SACT. In addition, some brittle materials which can be prepared using IBM techniques may break if prepared using SACT. Therefore, during selection of the TEM specimen preparation technique, consideration must be given to the type and depth distribution of the defects being investigated, as well as the specimen composition and defects produced during preparation. Further explanations as well as detailed descriptions of both types of techniques are described in the following section.

3.3.1 Bulk Sample Cutting

Most TEM specimen preparation techniques require the bulk samples to initially be cut into pieces <500μm thick. For brittle materials such as silicon, a wire saw, diamond saw or ultramicrotome may be used. Due to its well defined cleavage planes, a razor blade or other suitable tool can also be used to cleave thin slices of silicon; a fact which, once developed, allows for the preparation of electron transparent samples without the need for chemicals or ion beams. This developed technique is discussed in Section 3.3.7. Chemical wire saws are generally used for cutting metals.

3.3.2 Cross-sectional Sample preparation

It is possible to prepare samples so that their cross-sections can be imaged using TEM. Preparing samples in this way allows for the study of the interfaces in multilayered structures, as well as the depth distribution of defects. If such samples are required then they must be pre-prepared before being subjected to any type of thinning. The standard method used for semiconductors like Si is as follows. The faces-of-interest of the sample are glued together using a suitable epoxy. Extra pieces of no interest are glued either side of this structure. Once the epoxy has cured, a circular ultra-sonic drill is used to extract a circular core with the interfaces in the centre. This core is then fixed into a copper tube using epoxy. Once cured, the Cu-tube/Si-core structure is sliced into thin,

approximately 400μm, pieces using a suitable apparatus, commonly a diamond saw. These disk structures are then polished and thinned using a dimpler followed by an IBM technique, both of which are described below. The Cu surround allows the final fragile thinned sample to be handled without the need of further attachment to a specimen grid; it is a self supporting structure.

The method used throughout this study was slightly different and described in Fig 3.1. As with the previous method, the interfaces-of-interest were glued together, Fig 3.1a. This simpler structure was then cured and cut into pieces approximately 400μm thick using suitable equipment, such as a wire saw, Figs 3.1b and c. These cross-sectional samples were thinned using a tripod polisher, described below, followed by an IBM technique.

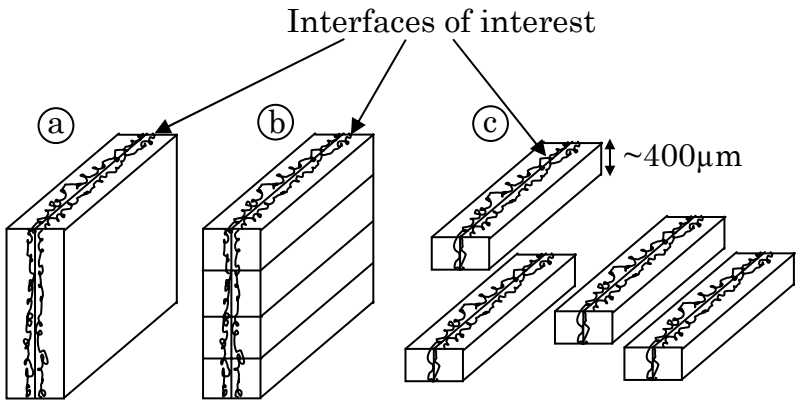

Figure 3.1: *Diagram showing the simple method employed in this study to produce cross-sectional samples of Si. The pieces on the right of the diagram, (c), have been cut using a wire saw to a thickness of approximately 400* μm.

3.3.3 Mechanical Polishing

Depending on the material and skill of the operator, it is possible to produce electron transparent samples solely by using mechanical polishing. An example of this is dimpling, which thins the centre of the sample using varying grades of diamond paste applied to a rotating wheel. Another example is the tripod polisher; developed by Anderson [1] it consists of a rigid support block for the sample and three feet that can be accurately levelled using micrometers, shown in Fig 3.2.

Figure 3.2: *Picture of 2 tripod polishers. The silver components on both polishers are the three micrometers which comprise the feet. The sample is attached the Perspex stub which is visible on the right hand polisher, indicated by x.*

Diamond impregnated disks are attached via water tension to a highly smooth polishing wheel, generally made of glass, which can vary in speeds between 1 to 30 revolutions per minute. The combination of mechanically polishing the sample on this wheel whilst supporting it using the tripod allows for the production of electron transparent plan view and cross-sectional TEM samples in a matter of hours. During both these techniques however, surface roughness may build up, producing samples of non-uniform thickness. Therefore much patience and practice is needed to produce suitable electron transparent samples using these methods alone. As a consequence, both dimpling and tripod polishing are generally used as a means of pre-thinning the samples to between 10 and 40μm, before completing the preparation with a final thinning stage. This final thinning, as well as further reducing the samples thickness, is designed to remove any damage produced during the preceding mechanical polishing stages. However the final thinning may also act to enhance the damage if sufficient surface roughness has already been produced. Therefore care must always be taken when mechanically thinning samples to ensure as smooth a surface as possible. Depending on the technique used, other forms of damaged may be introduced during this final thinning stage and are discussed below. Throughout this study, the tripod polisher was used as a means of pre-thinning the silicon samples to approximately 10μm.

3.3.4 Final Thinning of Specimens

Selection of the final thinning process depends on the type of material being prepared and on what is to be investigated. Metals and alloys, as they are electrically conductive, can be thinned using electropolishing. This method can be fast and introduce no mechanical damage, though the surface chemistry may be altered and reproduction of suitable conditions is difficult due to the large number of variables involved. For biological samples, polymers and crystalline materials, ultramicrotomy may be used. This technique simply cuts the sample using a knife blade if the material is soft, or initiates a partially controlled fracture for hard or brittle materials. No chemical change of the sample is induced during this process; however deformation structures such as knife marks, bends, tears and dislocation are introduced [1, 3]. In materials science, specifically investigation of radiation induced defects in semiconductors, ion beam milling (IBM) techniques and the small angled cleavage technique (SACT) are generally used, with IBM techniques being the more common.

3.3.5 Ion beam milling (IBM) techniques

Although there are a number of variations on the theme, in general, these techniques involve energetic ions incident onto a rotating sample at angles <20° to the surface inside a vacuum, as shown in Fig 3.3. The purpose of these ions is to sputter the material until it is electron transparent. For plan view specimens, only the un-implanted side is subjected to the energetic ions, whilst for cross-sectional specimens both sides are sputtered. In general Ar ions are used as they are heavy and inert and therefore result in a good sputtering yield with no chemical interactions with the sample material.

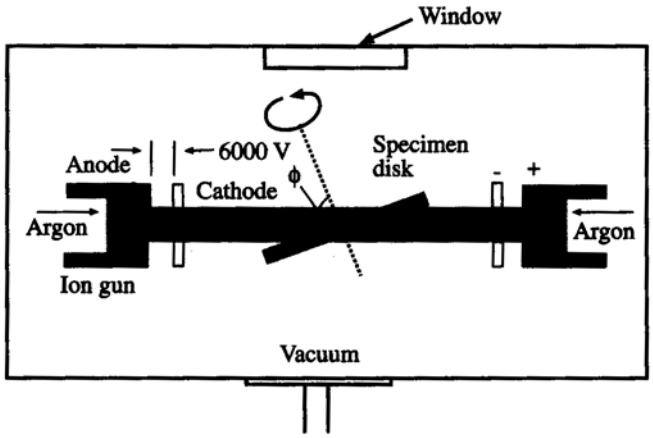

Figure 3.3: *Schematic, taken from [1] showing the basic principle adopted by all IBM methods. The rotating sample, in the middle of the diagram, is at a slight angle to the incident beams of Ar ions.*

In the conventional IBM system, Ar gas is fed into the ion guns, where a potential of up to 6keV creates a beam of Ar ions [1] which is directed on to the surface of the rotating sample. During the IBM process, Ar ion implantation into a shallow layer inevitably leads to damage accumulation in the near surface regions resulting in amorphisation of that area. The effect of these two artefacts is to reduce TEM image resolution and therefore they must be kept to a minimum. Various studies have been undertaken to determine conditions which minimise surface amorphisation [4-6]. Lowering the angles of the ion guns with respect to the specimen surface and decreasing ion energy reduces the thickness of the amorphous layer. However, as a consequence, milling times are increased. Surface roughness is reduced by rotating the sample a few revolutions per minute during the thinning process. Additional reduction of the damage is achieved by further reducing the milling angle by a couple of degrees for the final few minutes of thinning.

Samples are generally cooled using liquid nitrogen as the ion beams may otherwise heat up the samples to temperatures in excess of 200°C [7]. Depending on the material being prepared, such an effect could lead to defect diffusion thus alter the defect structure which is to be analysed. Throughout this study however, cooling was not necessary as the defects observed were not mobile at such temperatures. Also, in some experiments the samples were subjected to

thermal treatments in excess of 400°C, thus a further anneal of 200°C would have no effect on the defect morphology.

For the purpose of this study, a Gatan Duo Mill (DM) and Gatan Precision Ion Polishing System (PIPS) were used to thin the samples. For the DM, an accelerating voltage of about 4keV and gun current of 0.5 µA were chosen to thin the Si samples. The guns were operated at an angle of 18º from the surface of the sample. This angle was reduced to 16º for the final 10 to 15 minutes of thinning. The PIPS was operated with an accelerating voltage of about 2.5keV and gun current of 11mA at its maximum. The gun angles were set at about 8º from the sample surface, which were also reduced to about 6º for the final few minutes of thinning. The result of the reduced gun angles and the decreased accelerating voltage is that the samples prepared using the PIPS have a thinner amorphous layer compared to those produced using the DM.

3.3.6 The Effects of IBM Techniques on Vacancy-Type Defects in Silicon

In addition to the aforementioned artefacts produced by the IBM techniques, it has also been found that a perturbation in the defect morphology of small near-surface (up to a depth of a few nanometres), vacancy-type defects in silicon was produced when using either the DM or PIPS [2].

For this investigation, nanometre sized cavities were created in single crystal (100) Si via implantation with 10keV He ions and annealing at 900°C for 30 minutes. In addition to the main cavity band situated around the mean projected ion range R_p, small cavities of diameter approximately 2nm were located at the surface, up to a depth of a few nm. It is known that oxygen impedes the migration and coalescence of bubbles during thermal annealing [8]. It is believed that these smaller, near-surface cavities result from the recoil-implantation of oxygen from the native oxide layer during He implantation; a theory which is consistent with results obtained from simulations using the Monte-Carlo code SRIM [9].

The sample was separated into three pieces, each prepared for TEM analysis using either the SACT, DM or PIPS. Fig 3.4 is a composite image of the bright field TEM micrographs depicting the results. The cross-sectional samples were tilted slightly off the <110> zone axis to avoid strong Bragg diffraction and were also underfocused to obtain the best images of the cavities. The contrast of the cavities was further enhanced using Adobe Photoshop where a high-pass filter was applied and the grey-scale levels adjusted.

Image a) shows what is believed to be the unperturbed defect structure and is of the sample produced using SACT. Images b) and c) are of the samples prepared using the DM and PIPS respectively. A denuded zone is clearly visible extending from the surface to a depth of about 20nm denoted by the horizontal grey line. Between this and the main cavity band, smaller cavities are present. As other work has shown [10], interstitial-type, extended defects are also produced during He implantation and annealing, and are located slightly behind the cavity layer, not shown in these images. Owing to the type of defects present, this damaged region is likely to be under compressive stress.

During ion beam milling, the ion irradiation causes vacancies and interstitials, both mobile at liquid nitrogen temperatures and above, to be injected into the sample. The interaction of these defects with the cavities causes an alteration in cavity shape, leading to a change in centre of mass and thus cavity motion. Smaller cavities are more sensitive to this process therefore no motion is observed in the main cavity band. However, this process alone causes a stochastic motion of the cavities which will lead to a broadening of the distribution, and not the observed production of a denuded zone

The presence of the extended defect region however is likely to give rise to a strain gradient, dropping off towards the surface, thus making it energetically favourable for vacancy-type defects to migrate towards the strained region. It is this strain gradient which we believe may be responsible for the observed effect.

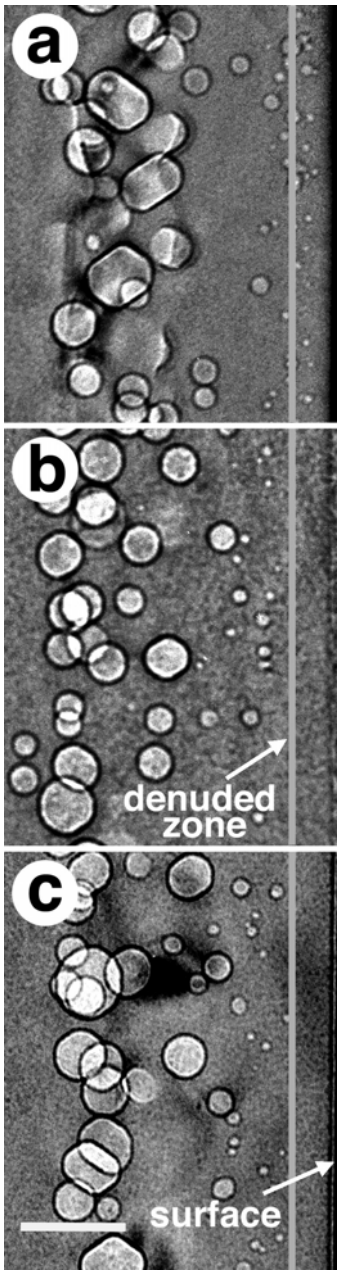

Figure 3.4: *A composite picture of three TEM micrographs depicting the defect morphology after sample preparation using either a)SACT, b)DM or c)PIPS. The white line represents 50nm [2].*

Whatever the process of cavity migration, it is clear that preparing TEM specimens using an IBM technique alters the defect structure under investigation. However, as it appears only small defects situated in the near surface region of the sample are affected, as long as this is taken into account during analysis, this perturbation may be an acceptable consequence of an otherwise extremely useful method.

3.3.7 The Small Angle Cleavage Technique (SACT)

This method, first reported by McCaffrey in 1991 [3] for the preparation of semiconductors, and extended to be used with polycrystalline and amorphous thin films on Si substrates by Suder in 1997 [11], produces many cross-sectional and plan view TEM samples in a matter of hours. Unlike previous methods, no pre-preparation is needed for the production of the cross-sectional samples.

Some crystalline materials are weakly bonded along one plane compared to other planes. For suitable materials (e.g. graphite), the classical cleavage method utilises this fact by repeatedly pulling apart the material, using adhesive strips, along the weakly bonded plane until the sample is thin enough for TEM [1]. However this can only be used to prepare plan view samples. McCaffrey developed an alternative cleavage methodology to produce thin tapered wedges of the material. These wedges can be mounted on Cu support grids with circular 1mm holes, in such a way that both cross-sectional and plan view imaging can be achieved. For (100) Si the standard cleavage plane, (that with the lowest bond energy) is the (110) plane. Cleaving along the (110) and the (120) plane, which is at an angle of approximately 18.5° to the (110) plane, produces these thin wedges.

Fig 3.5 schematically portrays the small angle cleavage technique, so called due to the small angle between the (120) and (110) planes. The material is cleaved along the (110) planes to produce a 6 x 3mm piece which is attached with low-temperature wax, implanted face down, to a metal stub. The material is then polished in a direction 18.5º with respect to the longer side using wet silicon carbide paper until it is approximately 100μm thick. This corresponds to the (120) direction. A diamond scriber and ruler are then used to scribe parallel lines along this direction, a few millimetres apart. Scribing acts to reduce the bond density thus allowing the material to fracture along this specific direction. Once the wax has been removed using acetone, applying a slight pressure causes the material to break along these

scribed lines. These smaller pieces are placed implanted face up in a weigh boat, in ethanol and under an optical microscope. Using a pair of tweezers to secure one of the pieces, a small amount of pressure is applied in the (110) direction using a silicon carbide scriber. This produces a small angled wedge where the very tip is electron transparent.

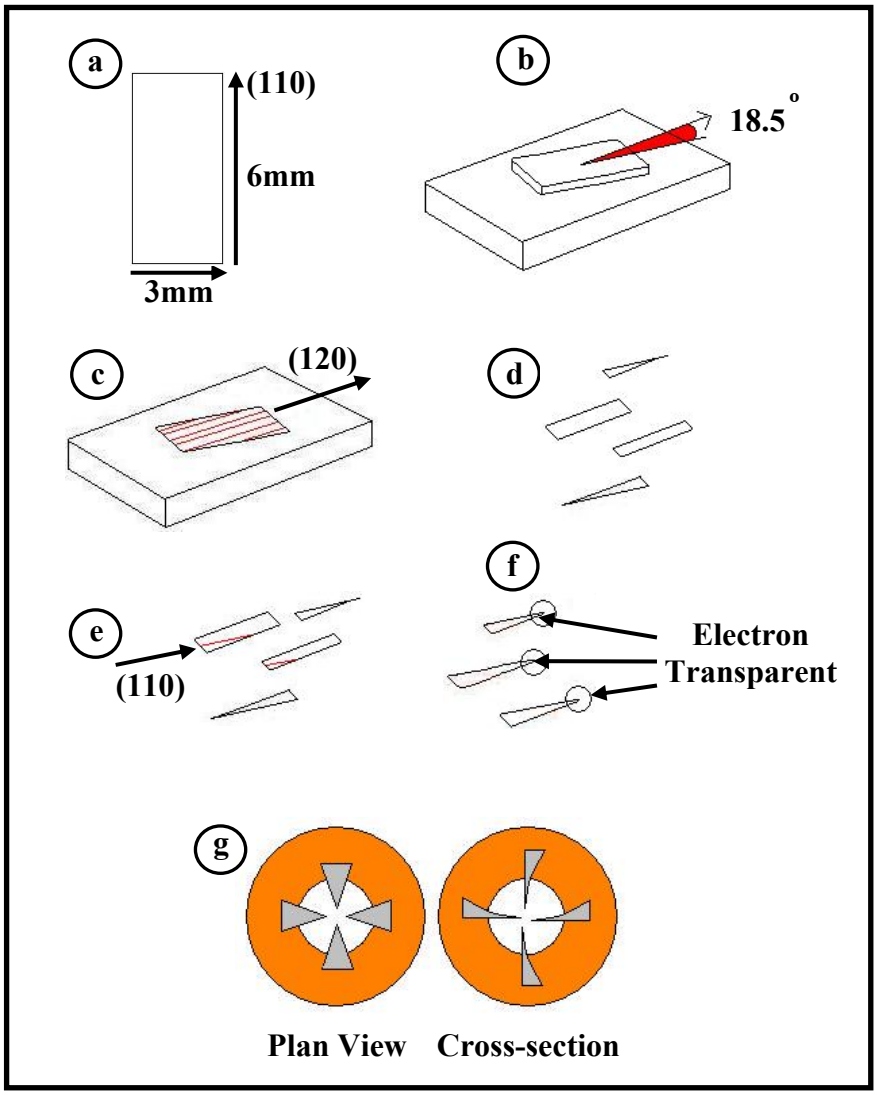

Figure 3.5: *Schematic depicting the SACT method. a) 6 x 3mm piece of Si produced by cleaving down the (110) direction; b) Back-polishing along the (120) direction; c) Lines scribed along (120) direction; d) Scribed lines break producing small pieces; e) Lines scribed along (110) direction; f) Tips of pieces produced are electron transparent; g) Pieces are mounted to produce either cross-sectional or plan view TEM images.*

Once this method has been applied to all the material in the weigh boat and the ethanol removed, the wedges can then be mounted, 4 to each grid, in either a plan view or cross-sectional manner, as shown in Fig 3.5g, using a conducting silver epoxy. No chemical etching or energetic ion beams were used, thus the only artefacts produced due to this technique are cleavage steps and a small amorphous SiO_2 layer approximately 1nm in thickness formed due to exposure to air [4]. neither of which have any significant effect on the internal defect structure of the samples. However, this technique is only suitable for XTEM when investigating the region <200nm from the surface. This is due to the fact that the wedge is tapered and therefore it rapidly increases in thickness. SACT can however be utilised as a check to see if the actual preparation method used alters the defect morphology, as it can be assumed to produce reference samples, i.e. those which are unaltered due to the preparation technique, as was assumed in the previous investigation [2].

Throughout this study, the defects under investigation were situated up to 1000nm below the surface where, during the previous investigation [2], the perturbation due to IBM was not observed. Considering this and the fact that larger areas of electron transparency are produced, and defects located at a greater depth can be imaged by preparing the samples by IBM compared to SACT, the IBM techniques were deemed more suitable.

Once electron transparent, the samples are now ready for TEM analysis. The subsequent sections explain the theory behind TEM, including the operational modes which were used in this study, followed by a description of the major components of the TEM.

3.4 The Transmission Electron Microscope

Fig 3.6 is a schematic diagram showing the basic components which comprise a conventional transmission electron microscope. All TEMs consist of a source which produces a beam of electrons inside a column under vacuum. This beam is accelerated by a high potential, then de-magnified and focused onto the sample using a set of condenser lenses and an aperture. The electrons are then scattered by the atoms in the sample. The objective lens collects these scattered beams which are then magnified and focused by the intermediate and projector lenses onto a fluorescent screen. Altering the strength of the intermediate lens allows for either a diffraction pattern or image of the internal structure of the material to be viewed on the screen. Recording of the image or diffraction pattern is achieved by raising the screen allowing the beams to be incident on photographic plates or to be imaged using a digital camera. Misalignment of the microscope will result in a loss of image resolution and therefore information. The major limiting factor for the resolution of the TEM is due to aberrations in the lens systems. It is important therefore to understand how each component works and is controlled in order to operate the TEM at its optimum level.

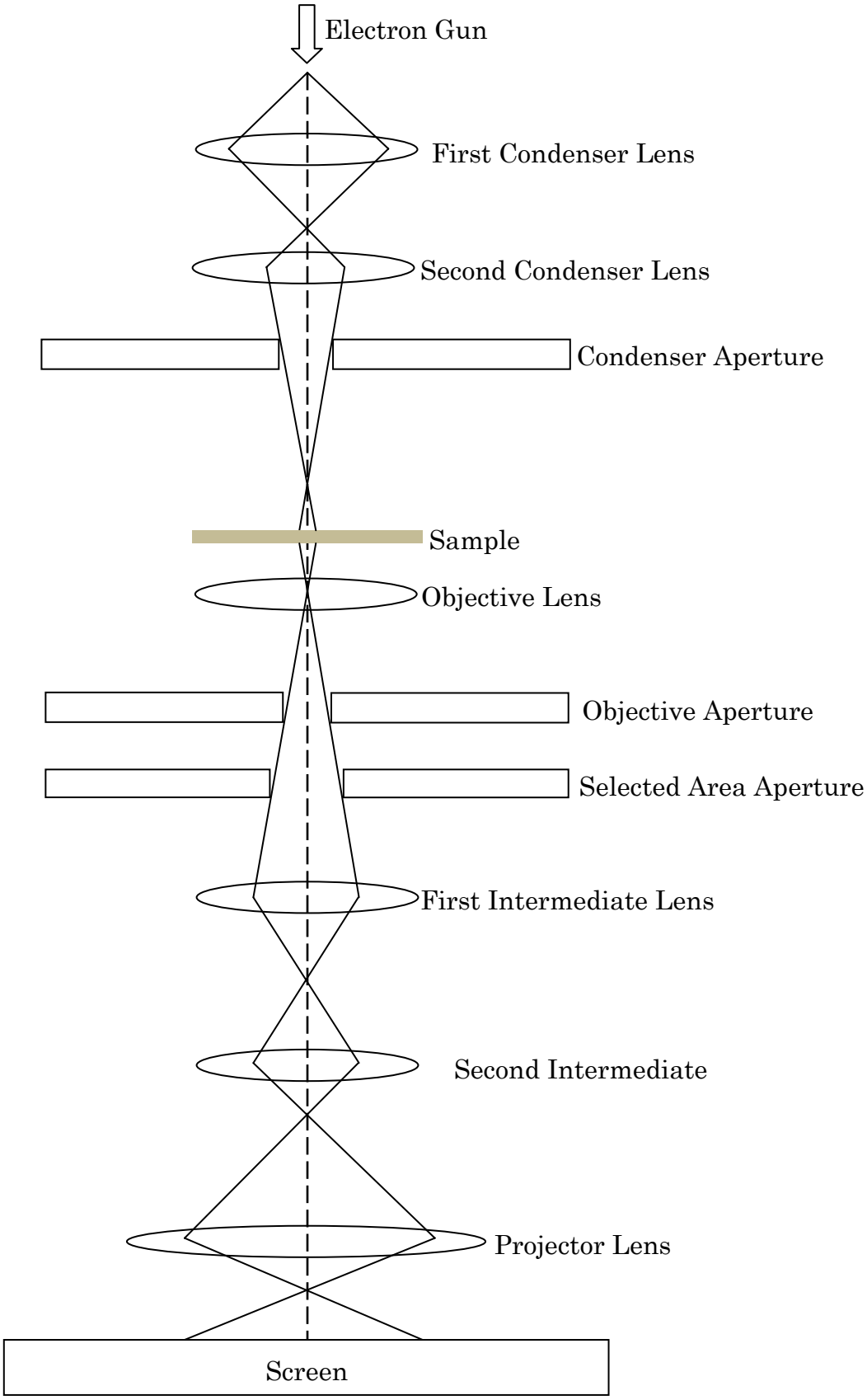

Figure 3.6: *Schematic diagram showing the basic components which comprise a conventional TEM.*

3.4.1 The Illumination System

This consists of the electron gun, condenser lenses, apertures and other components necessary to focus the beam onto the sample.

3.4.1.1 The electron gun

The electron gun in any traditional TEM consists of a Wehnelt cylinder into which a source is inserted that produces a beam of electrons which then pass through a hole in an earthed anode, as shown in Fig 3.7, a diagram from Williams and Carter [1] (page 73). This is known as a "triode gun" where the electron source is the cathode. The electrons leaving the source have, in general, a negative potential of greater than 100kV with respect to the anode, which results in the electrons being accelerated to velocities of greater than half the speed of light [1]. The Wehnelt cylinder allows for the control of the electron beam. A small negative bias is applied to the Wehnelt cylinder which results in the electrons being converged to a point between the cylinder and the anode. This point is known as the gun crossover which has a diameter d_0. The Wehnelt cylinder is therefore an electrostatic lens which focuses the electron beam to a relatively small size.

3.4.1.2 Electron sources

There are variations of two types of electron sources available; the thermionic source or the field-emission source. The latter utilises the fact that the strength of an electric field is increased at sharp points and it produces a very small diameter beam which, for conventional TEM such as used throughout this study, is not suitable as large areas of the sample cannot generally be viewed with sufficient brightness. Therefore it is the thermionic sources which are used and described here.

Electron emission from a thermionic source is achieved by heating the source to a temperature where the electrons in the source have sufficient energy to overcome the energy barrier. The energy barrier which the electrons energy needs to exceed for emission is known as the work function

(Φ) and is typically a few eV, which equates to temperatures that lead to melting or vaporisation of many materials. Therefore a source material must either have a high melting point, such as the tungsten filament used in the JEOL 200CX, or low work function like that of the lanthanum hexaboride (LaB_6) crystals used in the JEOL 3010.

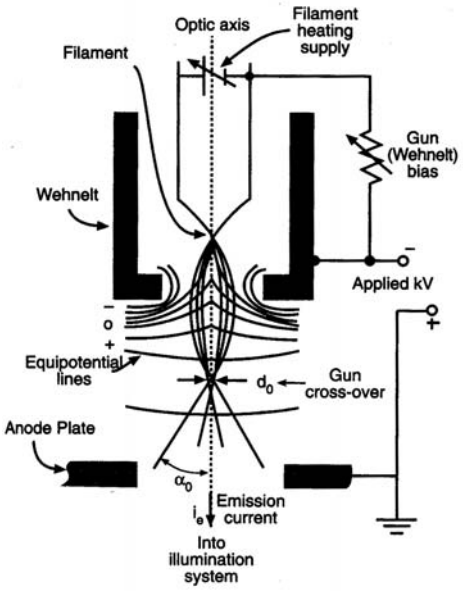

Figure 3.7: *Diagram of a typical electron gun. Electrons are produced from a source which acts as a cathode. The electron beam is focused to a relatively small size by the Wehnelt cylinder and then travels through a hole in an anode and into the rest of the illumination system [1].*

The sources are heated by passing a current through them. The temperature is increased by increasing the current until thermionic emission occurs. This emission current is know as the beam current i_e and it increases with increasing filament current. There exists a critical point where further increasing the filament current does not lead to any further increase of the beam current. This is known as saturation and it is generally with this current that microscopy is carried out. Working above saturation shortens the life of the filament, whilst working below it reduces the current incident on the sample which in turn decreases the intensity of any signal which is transmitted from the sample. In general the tungsten filament is

bent into a "V" shape and the LaB_6 crystal grown with a <110> orientation and both are designed to produce electron emission from a small area.

Once focused at the gun cross over the electron beam passes through the rest of the illumination system.

3.4.1.3 TEM Lenses

In the TEM, the beam of electrons is focused by means of several sets of magnetic lenses. A standard magnetic lens consists of a cylindrically symmetrical core, made out of a soft magnetic material such as soft iron, called a polepiece. A hole drilled through the centre of the polepiece is known as the bore. Surrounding the polepiece is a coil of copper wire. Application of a current through the wire results in the production of a magnetic field in the bore. As the electrons pass through the lens system they follow a helical path, which results in rotation of the image when altering magnification and focus. Some microscopes, for example the JEOL 3010, correct for this rotation by the introduction of an extra lens. In some cases two polepieces, one above the other separated by a gap of specific distance, are produced. Such a system is used for the objective lens. This allows for the introduction of the sample and objective aperture near the plane of the lens as is required in TEM.

It is convenient to neglect the helical path of the electrons and assume the lenses behave similarly to those in a standard light microscope when considering the formation of images and diffraction patterns. The basic principles are the same in that points on the objective plane are reproduced in the image plane and parallel rays passing through the lens are focused to points in the back focal plane. Fig 3.8 describes this schematically.

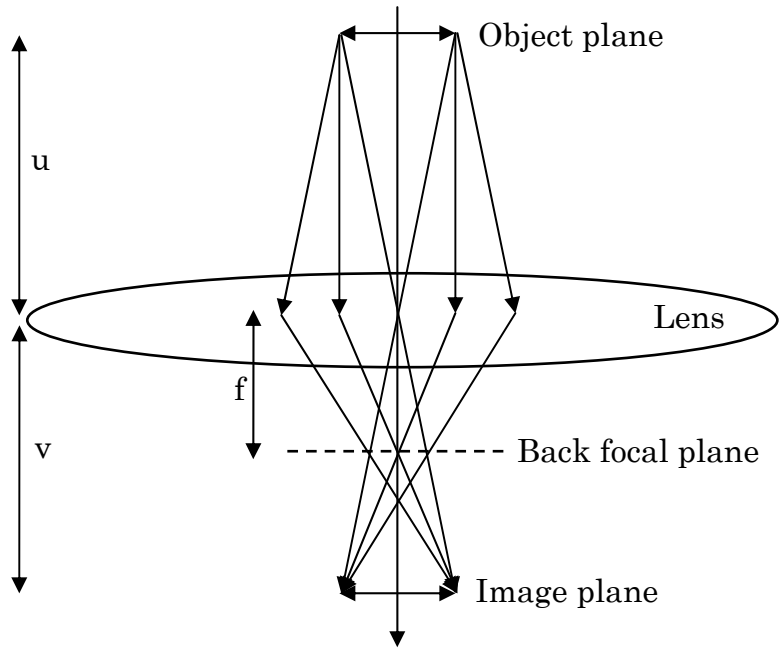

Figure 3.8: *Ray diagram for a finite object, indicative of what occurs in the TEM. A diffraction pattern is produced in the back focal plane, whilst an image of the object is produced in the image plane.*

Altering the strength of the lenses changes the magnification of the image. By adding several lenses in tandem it is possible to further magnify the image. This is done by making the image plane of the top lens the object plane of the lens below it. If the back focal plane of the top lens coincides with the object plane of the subsequent lens, an image of the diffraction pattern is produced.

Consider an object which is a point on the optic axis. The image will be in focus if the rays from the object recombine to a point in the image plane. If the lens is too strong then the rays will recombine before the image plane and the lens is said to be overfocused. If the lens is too weak then the rays will recombine below the image plane and the lens is said to be underfocused. Altering the strength of the lens to make it over and underfocused is a technique used when imaging vacancy-type defects such as bubbles.

As it is impossible to produce perfect magnetic lenses, many problems arise which ultimately limit the resolution of the TEM. The three main problems are discussed below and are termed spherical aberration, chromatic aberration and astigmatism.

3.4.1.3.1 Spherical Aberration

This problem arises due to that fact that magnetic lenses bend rays more strongly the further away they are from the optic axis. If the object being imaged is a point then this bending results in the production of a disk surrounded by a halo at the image plane. In fact it is on a plane above the image plane where the smallest image of the point is obtained. This plane is called the plane of least confusion and the disk produced is the disk of least confusion. Spherical aberration limits how much an image can be usefully magnified due to the degradation of the image.

3.4.1.3.2 Chromatic aberration

Electrons with lower energy are bent more strongly by magnetic lenses than those with higher energies. Typical TEM high voltage supplies are so stable that the energy spread of electrons produced by the electron source is of the order of 1-2eV, therefore there is minimal chromatic aberration of the beam incident on the sample. However inelastic scattering of the electrons in the sample results in a loss of energy and an electron energy spread ΔE of 15-25eV leaving the sample [1]. Therefore, as for spherical aberration, a disk of confusion is produced in the image plane of the objective lens. Chromatic aberration can be reduced by producing thinner samples.

3.4.1.3.3 Astigmatism

It is impossible to produce a bore in the polepiece which is cylindrical and perfectly symmetrical about the bore axis, therefore the electrons' helical trajectory is distorted due to a non-uniform magnetic field. This is known as astigmatism and it results in a distortion of the image.

It is possible to correct for this however using small compensating fields which are produced using stigmators. This is done manually on the TEM and though often takes much practice and patience to find the optimum conditions, results in great improvements of image quality. Astigmatism also arises if the apertures used are misaligned, contaminated or their shapes altered due to prolonged irradiation.

Even for a theoretically "perfect" specimen, these three aberrations, inherent to all magnetic lenses, limit the resolution of the TEM. The most important of all the lenses is the objective lens which collects the electrons from the sample and forms them into an image or diffraction pattern.

3.4.1.4 Condenser Lenses and aperture

This system either converges the electron beam onto the sample for use as a probe during nanodiffraction TEM or, as for use throughout this study, produces a de-magnified near-parallel beam, several micrometers in diameter. In general there are two lenses is this system, though some TEMs (such as the JEOL 3010) have three. The two lens system is shown in Figure 3.6. The first condenser lens C_1 de-magnifies the image of the gun cross-over. The strength of the second condenser lens C_2 is then altered to produce an underfocused image of the cross-over resulting in a near parallel beam incident on the sample. It is not possible to produce a totally parallel beam, but it is necessary to achieve as parallel and coherent a beam as possible to obtain the sharpest diffraction patterns and best image contrast. The addition of an aperture at C_2 decreases the angle of convergence β thus making the beam more parallel.

3.4.1.5 Moving and tilting the beam

Several magnetic deflectors called scan coils, located after C_2, can be used to tilt the beam so that it is incident on the sample through a range of angles, or to move the beam laterally across the sample in such a way that the beam remains parallel to the optical axis. The deflector scan coils are used

to traverse the beam across the sample and the tilt scan coils to tilt the beam with respect to the optical axis. This second process is used when producing centred dark-field images.

3.4.1.6 Alignment

Correct alignment of the illumination system results in the beam of electrons following a path down the optical axis, straight through the lenses and aperture, onto the specimen. To align the gun, it is first undersaturated so that the image of the filament is visible. This image is centred using the gun deflectors and the image of the filament is made symmetrical using the gun tilts. If the C_2 aperture is misaligned the beam will move across the screen as it is overfocused and underfocused. Aligning is done by condensing the beam until the aperture is visible then, using the external controls, the aperture is centred. The beam is then focused and using the deflector controls centred on the screen. This process is repeated until the beam is condensed and focused about the centre of the screen, and without distortion of its spherical nature.

3.4.2 The Objective Lens

This lens is used to form either an image or diffraction pattern using the scattered beams as they exit the specimen and is considered to be the most important lens in the TEM. The specimen holder is placed in the centre of the polepiece of this lens via a side entry mechanism. As the holder is much thicker compared to the sample, it exists in many planes inside the lens. It is important that the specimen is positioned in the centre of the polepiece in a plane known as the symmetric plane. This is done by altering the height of the sample in the holder. It is necessary that the specimen can be tilted whilst the area of interest remains in view with little or no translational motion. This is done by ensuring the specimen is in a plane known as the eucentric plane, which coincides with the symmetric plane.

It is often necessary to form a diffraction pattern from a specific area in the sample. This is achieved by inserting an aperture, called the selected area aperture, so that only electrons from the area of interest are used in the formation of the diffraction pattern. It is important to do this for example if an area was thought to be amorphous, then it is possible to look at the diffraction pattern from that specific area provided it is not smaller than the aperture. As the aperture cannot be inserted in the plane of the sample, it is inserted in the image plane of the objective lens which yields the same result as if inserted in the sample plane. This is known as selected area diffraction (SAD) and should be carried out whenever analysis of a specific defect or area on the sample is required.

The objective aperture is used to limit the collection angle of electrons transmitted from the sample. The use of this aperture results in aberrations in the image and limits the resolution of the TEM. It is placed in the back focal plane of the objective lens. Centring the aperture on the (000) reflection produces a bright-field image. It can be moved off the optical axis to select one of the diffracted reflections, producing a dark-field image. These off-axis dark-field images suffer from aberrations and are highly distorted. To rectify this, the tilt scan coils are used to tilt the beam above the objective lens so that the diffracted beam travels down the optical axis. This is known as centred dark-field imaging and should, in general, be performed for all dark-field images.

3.4.3 The Imaging System

This system consists of the intermediate and projector lenses, apertures and a viewing screen. The strength of the intermediate lens can be altered so that its object plane coincides with either the image plane of the objective lens to form an image, or the back focal plane of the objective lens to form a diffraction pattern.

The back focal plane of the intermediate lens coincides with the object plane of the projector lens. The image can be magnified hundreds to hundreds of thousands of times using the projector lens. The back focal plane of this lens coincides with the viewing screen.

3.5 Transmission Electron Microscopy

In a transmission electron microscope a beam of electrons enters the sample under investigation where it interacts with the atoms in the material and is then transmitted out of the bottom surface. The electrons are then directed onto a fluorescent screen producing a 2-dimensional projection of the internal structure of the sample. Due to the periodicity of the sample and the wave nature of electrons, a diffraction pattern can also be formed which allows for further investigation of the crystallographic structure of the sample and defects therein.

In all types of microscopes the resolution of the final image is ultimately limited by the wavelength of the radiation used. Hence smaller objects can be imaged by using X-rays or electrons compared to when using an optical microscope. Unlike X-rays, electrons are charged particles and so they can be accelerated to precise velocities in an electrostatic field and focused using magnetic lenses. They are also strongly scattered in the target material by the positive nuclei and the electron clouds via a coulomb interaction, making them sensitive to the structure of the material. An increase in the electrons' accelerating voltage results in a decrease in their wavelength thus, using high energy electrons (from approximately hundred keV to several MeV), objects can be magnified hundreds of thousands of times with resolution down to the atomic level.

TEM is only possible because of the way in which the electrons interact with the atoms in the sample. The following section describes the interactions and details some of the applications which have arisen because of them.

3.5.1 Electron Interactions

When an electron enters a sample, it can either pass through un-deflected or interact with the atoms in some way. The beam of electrons incident on the sample surface in a TEM is monoenergetic and of uniform intensity. Scattering of the electrons by the atoms can lead to variations in intensity producing an image of the sample. Diffraction patterns are produced when the diffracted electron beams interfere constructively producing an interference pattern. Constructive interference can only occur if the electron waves remain coherent after exiting the sample. This will not happen if the electron loses energy during its interaction with the substrate. If an electron is deflected without energy loss, then this event is known as *elastic scattering*. An electron which imparts some of its energy to the atom during interaction is said to be *inelastically scattered.*

As Figure 3.9, adapted from Williams and Carter [1] (page 22), illustrates, inelastic electrons are almost always incoherent and are transmitted through very small angles ($<1^{o}$) relative to the optic axis. Elastically scattered electrons can be both coherent and incoherent. The greater the angle with which the electrons are deflected, the more likely they are to be incoherent. Electrons whose scattering angles are greater than 10° are generally incoherent [1]. Thus in conventional TEM, only those electrons which are scattered through 1° to 10° are used to form diffraction patterns and images. However, as will be explained in Section 3.5.3.1.2, incoherent elastically scattered electrons have been used in recent years to produce images of atomic resolution, which distinguish between areas of the sample containing different elements. This technique, known as Z-contrast imaging, has also been employed in this study. The incoherent elastic scattering of electrons is known as Rutherford scattering.

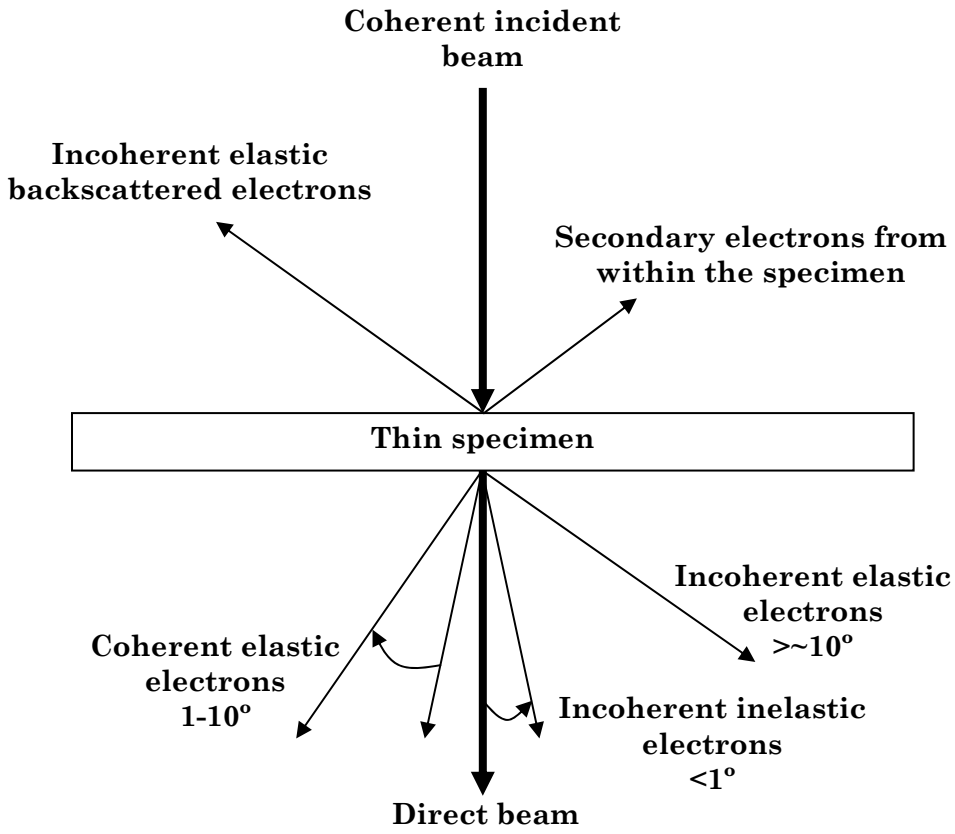

Figure 3.9: *Diagram showing the different types of scattering which can occur as an electron beam passes through a thin piece of material [1].*

3.5.1.1 Elastic Scattering

Elastically scattered electrons do not transfer energy to the atoms in the sample and a change in their momentum occurs. The angle through which the electrons are scattered depends on the electron energy (the beam energy), the atomic number or atomic weight of the atoms in the specimen, the thickness and density of the sample and importantly the crystallinity of the material. Electrons scatter less as their energy increases and heavier atoms scatter electrons more than lighter ones. In a crystalline material the elastically scattered electron waves are mainly coherent and therefore have a well defined phase relationship with each other and the incident electron wave which may result in the production interference patterns.

In amorphous materials the primary scattering mechanism is incoherent scattering. Here the scattering is random and therefore a change in phase occurs between the incident electron wave and the scattered wave.

3.5.1.2 Inelastic Scattering

An electrons interaction with either the electron-cloud or nucleus may result in loss of energy. In general, during nuclear interactions the larger the angle of scatter, the greater the probability that the electron will lose energy. Although inelastically scattered electrons are not used in TEM to produce images or diffraction patterns, they are by no means inconsequential.

An important consequence of inelastic scattering in TEM occurs when electrons in the electron beam interact with the electrons in the valence band of the sample causing them to oscillate. This is known as plasmon generation. The scattered electron is scattered at very small angles and produces a diffuse background intensity to the diffraction pattern or image.

In addition to plasmon generation, when a high energy electron interacts with an atom in the sample, the surrounding lattice vibrates. The resultant lattice oscillations are called phonons and they cause localised heating of the sample. The incident electrons are scattered by these phonon vibrations. This results in diffuse background intensity between diffraction spots, visible on all diffraction patterns [1]. In order to generate clearer diffraction patterns the TEM samples may be cooled, decreasing the amount of phonon scattering.

3.5.2 Electron Diffraction

A consequence of the wave nature of electrons is the constructive and destructive interference which occurs after the electron waves have diffracted off planes of atoms in the material. This results in the production of diffraction patterns which yield a wealth of information about the structure of the material and any defects which may be present. Diffraction

patterns allow us to determine whether the specimen is amorphous, crystalline or polycrystalline. From these patterns we are able to find the crystallographic orientation of the specimen if it is a single crystal, or the orientations of the crystal grains if polycrystalline. It is also possible to identify certain defects, such as platelets or microtwin lamellae, via a diffraction pattern, as well as measure lattice spacings allowing for the determination of the composition of the material. An example of a diffraction pattern is given in Figure 3.10. This particular pattern was formed from (001) Si, imaged down the [110] zone axis, at the interface between crystalline and amorphous Si. Each spot corresponds to a particular plane of atoms in the real crystal. The diffuse ringed pattern is indicative of amorphous Si.

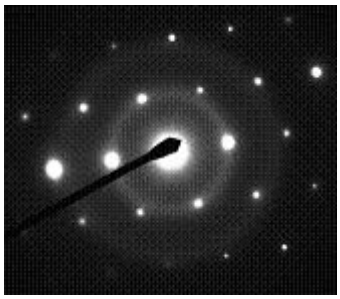

Figure 3.10: *Diffraction pattern produced from (001) Si, imaged down the [110] zone axis, at the interface between amorphous and crystalline Si.*

Diffraction patterns are only produced when the diffracted beams of electrons interfere constructively. Constructive interference only occurs if the beams are coherent and remain in phase with one another following diffraction. Consider two parallel plans of atoms a distance d apart as given in Figure 3.11. A beam of electrons can be thought of as a plane wave, incident on the planes at an angle θ. The plane wave is scattered by the atoms also by an angle θ, analogous to the way light reflects off a mirror. Because of this similarity, the spots in the diffraction patterns are known as reflections. In order for the left hand beam to remain in phase with the right hand beam, it travels an extra distance given by AB+BC, which must equal an integral number of wavelengths $n\lambda$.

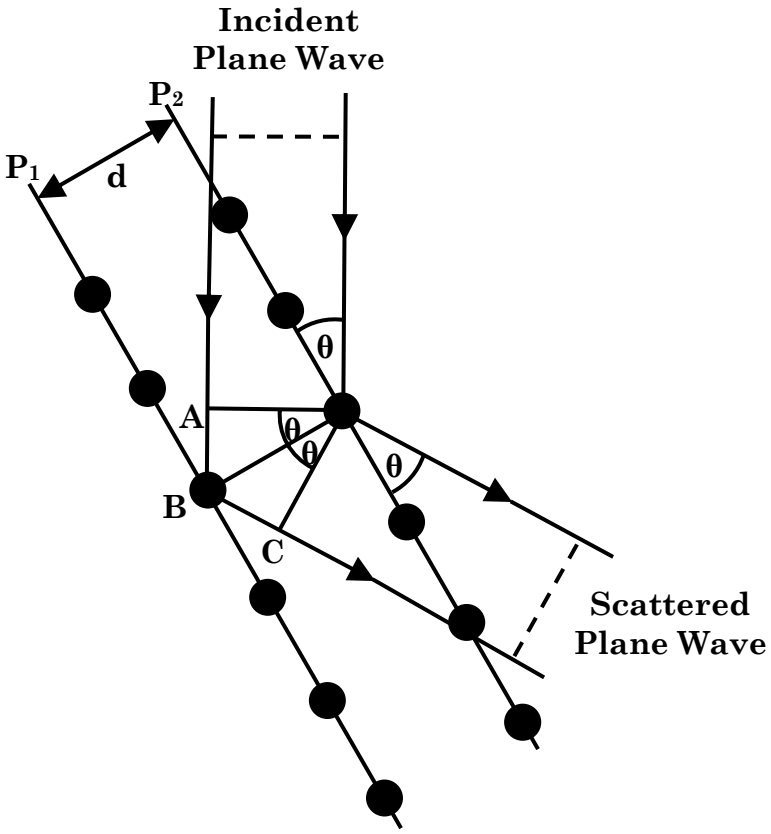

Figure 3.11: *Diagram showing a plane wave incident on two parallel planes of atoms. In order for the wave to remain in phase, the left hand side must travel an extra distance which equates to nλ [1].*

As AB = BC we can write 2AB = $n\lambda$. The path difference AB is found by basic trigonometry, such that:

$$AB = d \sin \theta \qquad [3.1]$$

Substituting $n\lambda$ / 2 for AB and re-arranging gives:

$$n\lambda = 2\ d \sin \theta \qquad [3.2]$$

This equation was first derived by William Bragg and his son in order to explain their observation that X-rays only reflected off faces of crystals at certain angles. This equation is therefore called the ***Bragg equation***.

Constructive interference only occurs when θ is a specific angle known as the Bragg angle θ_B. If the electron wavelength and reflecting angle is known, then by using this equation it is possible to calculate the interplanar spacings d in the crystal and therefore, in some cases, determine the composition of the material. If the wavelength is kept constant, a larger angle of deviation is observed as the reflecting planes get are closer together. Thus d is proportional to 1/θ and the distance between the spots in the diffraction pattern increases as the interplanar spacing decreases.

In TEM, it is convention to describe the incident plane waves in terms of wave propagation vectors **k**, which are normal to the wavefront. Fig 3.11 can be simplified using wave vectors, as illustrated in Fig 3.12(a), taken from Williams and Carter [1] (page 181), where $\mathbf{k_I}$ and $\mathbf{k_D}$ are the wave vectors for the incident and diffracted electron beams respectively.

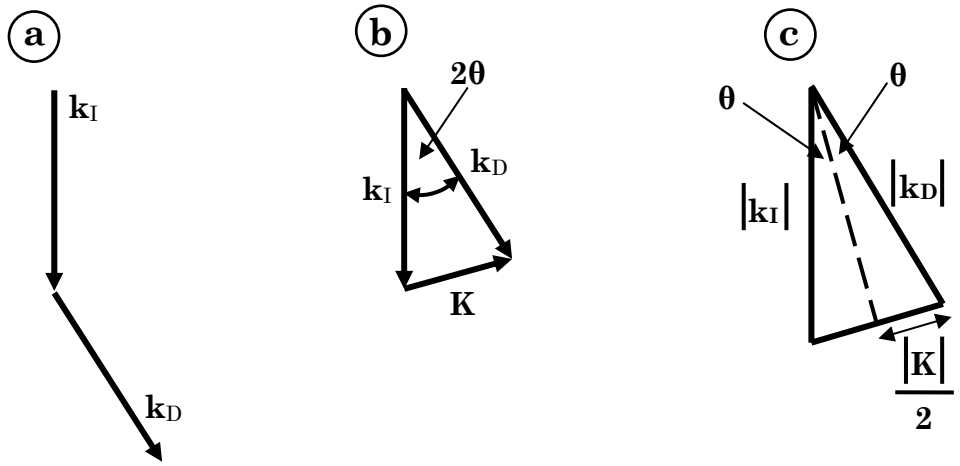

Figure 3.12: *This diagram from Williams and Carter [1] shows electron beam diffraction off a plane of atoms in terms of wave vectors **k**. (a) gives a simplified version of Fig 3.11. The change in wave vector as a result of the diffraction is given by the vector **K**, shown in (b).*

The change in wave vector as a result of diffraction through any angle θ is given as $\mathbf{K} = \mathbf{k_D} - \mathbf{k_I}$. Provided the electron was elastically scattered, an inverse relationship exists between the electron's wavelength and wave vectors such that:

$$|k| = \frac{1}{\lambda} \qquad [3.3]$$

From Fig 3.10(c), an expression for θ can be written such that:

$$\sin\theta = \frac{|K|/2}{|k_I|} \qquad [3.4]$$

Or:

$$|K| = \frac{2\sin\theta}{\lambda} \qquad [3.5]$$

At the special condition where $\theta = \theta_B$, equation 3.5 is written as:

$$|K| = \frac{2\sin\theta_B}{\lambda} \qquad [3.6]$$

By taking $n = 1$, Bragg's equation can be rearranged such that:

$$2\sin\theta_B = \frac{\lambda}{d} \qquad [3.7]$$

By rearranging equation 3.7 and combining with this form of Bragg's equation, it can be shown that:

$$|K_B| = \frac{1}{d} \qquad [3.8]$$

Only at this special Bragg condition does constructive interference occur and reflections are produced in the diffraction pattern. The wave vector $|\mathbf{K}_B|$ is defined as **g** and is known as the Bragg vector.

Consider many parallel planes, separated by a distance d, orientated to the incident electron beam such that the Bragg condition is satisfied. As is shown in Figure 3.13 a series of reflections is produced.

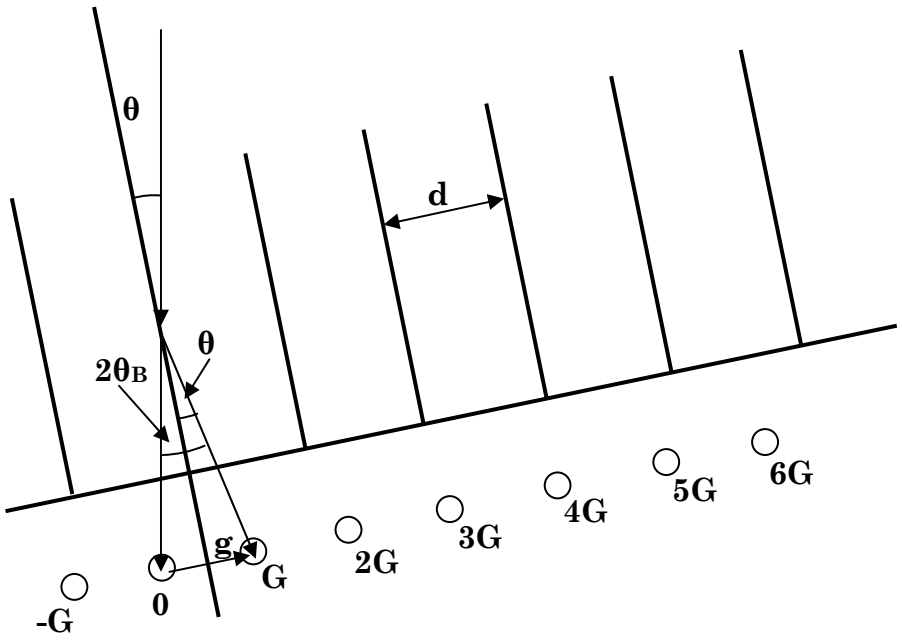

Figure 3.13: *This diagram shows parallel planes of atoms orientated such that the angle between them and the incident electron beam satisfies the Bragg condition. When this occurs many reflections produced [1].*

The reflections denoted by **–G**, **0, G**, **2G** etc are periodically spaced, separated by **g** along a line. The vector **g** is always normal to the reflecting planes.

3.5.2.1 Real Diffraction patterns

By extending this construction to 3-dimensions, diffraction patterns such as that shown in Figure 3.10 are produced. The way in which the reflections are arranged in the pattern allows for the identification of the orientation of the crystal. Taking single crystal Si for example, there are three major crystallographic orientations which exist. These are known as the lowest order indices and are illustrated in Figure 3.14.

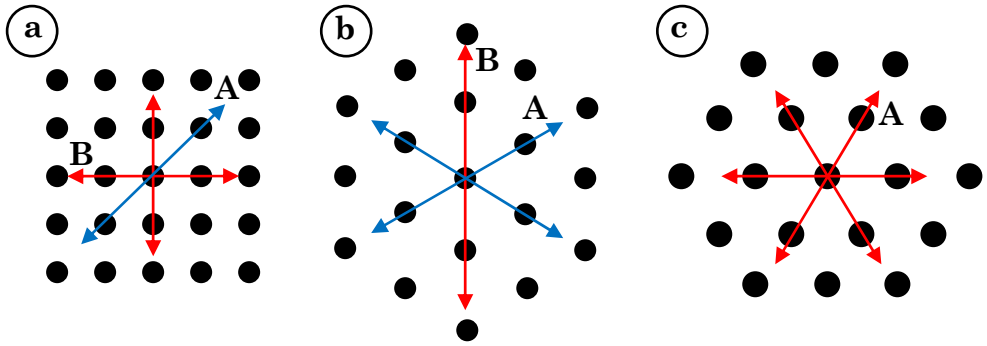

Figure 3.14: *The diffraction patterns indicative of the three lowest order indices in Si: [001], [110] and [111] are shown in (a), (b) and (c) respectively.*

Depending on the orientation, the distance between the reflections along one direction may be different compared to along another. The ratios of the spacings taken along two directions, indicated as A and B in the figures, are unique to that orientation and therefore may be used to determine which orientation is being imaged.

In real diffraction patterns, reflections are produced even when the Bragg condition is not exactly satisfied. In order to understand this, first consider a 3-dimentional array of spots where each spot corresponds to a set of parallel planes of atoms in the corresponding crystal lattice. This array is known as the reciprocal lattice. Each point on the lattice is located a distance $1/d_{hkl}$ from the origin of the lattice, where d_{hkl} corresponds to the interplanar spacing of a plane with indices *hkl* (e.g. for the (110) plane; h=1, k=1 and l=0). Next, a sphere of radius $1/\lambda$ is constructed, such that it passes through the origin O of the reciprocal lattice as shown in Fig 3.15. The origin is defined as the reflection corresponding to the direct (000) beam as is shown in Fig 3.13. The sphere is known as the Ewald sphere.

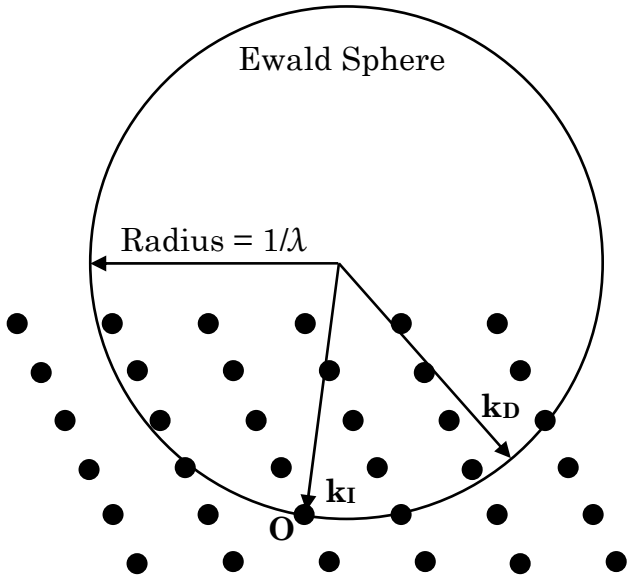

Figure 3.15: *Construction of the reciprocal lattice and the Ewald Sphere with radius 1/λ. The origin of the reciprocal lattice O corresponds to the direct beam reflection.* $\boldsymbol{k_I}$ *and* $\boldsymbol{k_D}$ *are the incident and diffracted wave vectors, respectively.*

When the sphere intercepts a reciprocal lattice point, the Bragg condition is satisfied for the corresponding plane of atoms, and the reflection corresponding to that plane is visible in the diffraction pattern. Each reciprocal lattice point is in fact a rod with finite width and whose length is perpendicular to the thin foil of the specimen. They are known as relrods. If the sphere intersects the centre of a relrod then the Bragg condition is exactly satisfied and $\mathbf{K} = \mathbf{g}$. If the sphere intersects at some other point along the relrod, Bragg is not exactly satisfied but reflections are still visible on the diffraction pattern. This departure from Bragg is measured by a vector **s** called the deviation parameter. The wave vector resulting from diffraction can therefore be defined as:

$$\mathbf{K} = \mathbf{g} + \mathbf{s} \qquad [3.12]$$

The concept of relrods is very important in understanding the diffraction patterns from samples which contain certain defects, for example, microtwins.

Figure 3.16 is a diffraction pattern taken from an area of Si containing microtwin lamellae. These defects have been described in Chapter 2 and have a crystallographic orientation which is the mirror reflection of the surrounding matrix. The extra reflections in this diffraction pattern are due to the presence of these microtwin lamellae. As the crystallographic structure of the microtwins and the undefected Si are the same, their corresponding diffraction patterns will also be the same. However, due to the orientation change of the microtwins, their diffraction pattern is rotated with respect to the pattern of the surrounding Si, resulting in the extra reflections. Streaking occurs because of the finite dimension of the microtwins which results in an extension to length of the relrods. If the electron beam is parallel to the relrods then no streaking is observed. However, if the relrods are nearing 90° to the electron beam, diffuse lines are visible on the diffraction pattern.

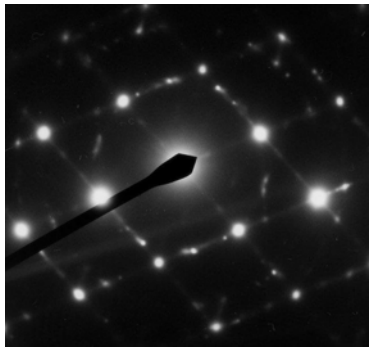

Figure 3.16: *A diffraction pattern taken from a defected area of (001) Si, imaged down the [110] zone axis. This region is comprised of microtwin lamellae in the Si matrix. The microtwin lamellae have the same crystallographic structure as the Si matrix, but are inclined along <111> type directions, resulting in the extra reflections in the diffraction pattern.*

Fig 3.17 is a diffraction pattern taken from amorphous Si. As was described in section 2.5.1, although the bond angles and lengths are distorted, a-Si retains the four-fold coordination indicative of c-Si. Therefore there is a probability that, per unit element of volume, a Si atom will be located a distance r from another Si atom. This probability is called the radial

distribution function, $\rho(r)$. To understand the ringed pattern, first consider a sample which contains many crystalline grains of the same crystallographic orientation but rotated with respect to one another. Each grain will produce its own diffraction pattern. As with the microtwin lamellae, the diffraction patterns will be superimposed onto each other but rotated with respect to one another. The resultant diffraction pattern therefore, comprises many spots arranged into rings and the distance between the rings gives the nearest neighbour spacing. This concept is then extended to a-Si, where each atom can be thought of as Bragg diffracting on some direction which produces the concentric circle pattern shown in Fig 3.17. The circles are diffuse because of the distorted bond angles and lengths indicative of a-Si.

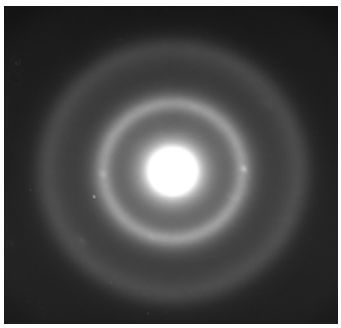

Figure 3.17: *Diffraction pattern taken from amorphous Si.*

3.5.3 TEM Image production

As previously mentioned, images in the TEM are produced because the electrons are scattered by the atoms in the material resulting in changes in intensity on the viewing screen. During the scattering events, both the amplitude and phase of the electron waves can vary, giving rise to changes in contrast in the final image. If many electrons contribute to generating the image then the intensity is high, however as a consequence the contrast is poor. In order to study defects within the sample, it is necessary to obtain strong contrast in the final image. This is achieved by selecting fewer electron beams or conventionally, just a single electron beam, by placing an aperture just above the specimen (objective aperture as discussed in Section 3.4.3). The majority of TEM analysis undertaken during this study utilised

the contrast arising from the alterations in amplitude. Images formed in this way are termed amplitude contrast images. Some high resolution TEM was also performed during this study. This type of microscopy uses the contrast arising due to changes in the electron wave's phase and the images produced are aptly named phase contrast images. Both amplitude and phase contrast images are discussed below.

3.5.3.1 Amplitude Contrast

In order to maximise the contrast in the image and to be able to relate the image to the corresponding diffraction pattern, an aperture is used to select either the direct transmitted electron beam or one of the diffracted beams. It is essential that the chosen beam is parallel to the optic axis as this reduces aberrations in the final image therefore improving resolution. If the microscope is well aligned then the direct beam should already be situated parallel to the optic axis. An image formed with the direct beam is called a bright-field image. To form an image with a diffracted beam it is necessary to tilt the incident electron beam so that the transmitted diffracted beam is parallel to the optic axis. An image formed in this way is known as a centred dark-field image.

The two main types of amplitude contrast whose effects are observed in TEM are mass-thickness contrast and diffraction contrast.

3.5.3.1.1 Mass-thickness contrast

This type of contrast arises due to the Rutherford scattering of electrons, which as discussed earlier in this section, results in incoherent elastically scattered electrons. The cross-section for elastic scattering is a function of the atomic number Z, and the number of scattering events increases with the thickness of the specimen. As explained in Section 3.3, it is not possible to produce a TEM specimen of uniform thickness. Ignoring all other contrast mechanisms, a bright-field image of a real TEM sample will appear darker in areas where the sample is thicker. In addition, heavier elements scatter a

greater number of electrons off the axis than lighter elements, therefore regions of greater atomic mass will also appear darker compared to areas containing lighter elements.

3.5.3.1.2 Z Contrast

High resolution images which can distinguish between areas containing different elements can be produced by TEM. This imaging technique is known as Z contrast imaging and it represents the limit of the mass-thickness contrast mechanism [1]. The high-angled (>10°) incoherent elastically scattered electrons are used in forming this type of image. This is to ensure that the Bragg diffracted electrons do not contribute to the image. In Z contrast images, areas comprised of heavier elements appear lighter compared to areas of light elements.

3.5.3.2 Diffraction Contrast

Diffraction contrast is the dominant form of contrast in conventional TEM images of crystalline materials and is used to image defects which may be present in the sample. To obtain a strong diffraction contrast the sample is tilted into what is known as two-beam conditions, where only the direct reflection and one diffracted reflection are visible on the diffraction pattern. Electrons from many Bragg diffracting planes contribute to a bright-field image and so for crystalline material, much of the image appears bright. Amorphous areas and defects with different crystallographic orientations to the matrix or with strain fields which bend the surrounding planes so that they are not at the Bragg condition will appear darker. As a dark field image uses only one diffracted beam to produce an image, much of the image will appear dark with only those areas or defects whose orientations satisfy Bragg being bright. Dark-field images therefore exhibit greater contrast than the corresponding bright-field image.

If the diffraction pattern exhibits extra reflections as shown in Fig 3.16, by centring one of these reflections and selecting this reflecting beam with an

aperture, a dark-field image which only shows the defects responsible for the extra reflections will be produced. Such images were produced during this study, providing more evidence for the existence of microtwin lamellae in some of the samples.

3.5.3.2.1 Weak Beam Dark-Field (WBDF) images

It is possible to achieve even stronger contrast by using an imaging technique known as weak beam dark-field (WBDF) microscopy. As with basic dark-field images, defects appear bright on a dark background. The basic principle behind this technique is to tilt the sample so that majority of planes in the crystalline matrix do not satisfy the Bragg condition. If there is a defect like a dislocation present, its strain field will bend the planes surrounding it. The sample is tilted so that these bent planes satisfy the Bragg condition, as illustrated in Fig 3.18.

In practice, such an image is formed by first choosing a particular **g** in the dark-field diffraction pattern, and centring it in the same way as to produce a centred dark-field image. The sample is then tilted so that only the reflections along that specific **g** direction are systematically excited. Depending on the defect under observation, other than **g**, only one specific reflection is to be excited, for example the 5**g** reflection. The sample is then tilted to increase $s_{\mathbf{g}}$, which consequently decreases the intensity in this reflection, hence the name "weak beam". An aperture is then used to select **g**. Planes close to the defect satisfying Bragg will appear white on a dark background and very narrow in width, yielding greater resolution and stronger contrast compared to conventional bright-field or dark-field images. The defect observed in the image is displaced slightly compared to where the actual defect resides in the specimen as it is the surrounding planes which are Bragg diffracting and it is these which are observed.

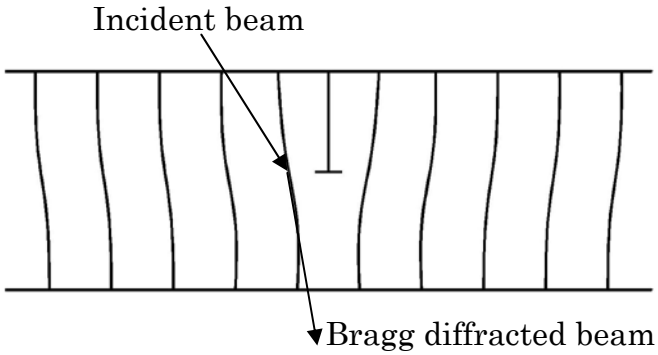

Figure 3.18: *Diagram illustrating how planes of atoms surrounding a dislocation are bent due to the defect's strain field. This strain field can be imaged by using WBDF microscopy. The sample is tilted so that only the planes surrounding the defect satisfy the Bragg condition. The final image therefore appears dark except for those Bragg diffracting planes close to the defect, resulting in enhanced diffraction contrast.*

3.5.4 Phase Contrast

When an electron wave is diffracted in the sample, it undergoes a phase change. When many transmitted beams with different phases interact, an interference pattern is produced which is observed in the final image as fringes. These fringes are the visible effect of phase contrast and they can give rise to information about lattice spacings. Phase contrast can only occur therefore, whenever more than one beam is used to form an image. To produce phase contrast images an aperture is used to select several beams, in contrast to bright-field and dark-field imaging. During this study, three affects of phase contrast were used in producing TEM images. These were Moiré Fringes, Fresnel Contrast and High Resolution TEM (HRTEM) and are described below.

3.5.4.1 Moiré Fringes

The effects of phase contrast are also visible in diffraction contrast images. Figure 3.19 is a WBDF image of solid Xe precipitates in a Si matrix. Because the lattice spacings of solid Xe and Si are similar, the overlap of these two structures produces a fringe pattern. This type of pattern is

known as a Moiré fringe, and has been observed in some of the samples investigated during this study.

Figure 3.19: *A WBDF image showing the Moiré fringes produced when two lattices of similar or equal lattice spacings overlap.*

3.5.4.2 Fresnel Contrast

Fresnel contrast is a form of phase contrast which arises where there is an abrupt alteration in inner potential, such as at the boundary of a void in crystalline Si. The path travelled by the electrons through the void is different to those travelling in the surrounding crystal, resulting in a phase difference and the production of fringes surrounding the void. A He or Xe filled gas bubble in Si will appear very light with a dark fringe in underfocus, and dark with a very light fringe in overfocus. When the image is in focus, the defect is not clearly visible. The same is true for surfaces of the sample, which has a light fringe if the image is overfocused, and a dark fringe in underfocus. No fringe is produced if the image is in focus.

3.5.4.3 High Resolution TEM (HRTEM)

Under optimal conditions, high resolution TEM can produce 2-dimensional images of the arrangement of the columns of atoms in a crystal. In order to achieve this, a very thin sample has to be oriented in down-zone conditions, where the electron beam is perpendicular to one of the low-index directions. The lattice planes that are almost parallel to the electron beam will be close to the Bragg condition and will diffract the beam. The resultant diffraction pattern is a Fourier transform of the periodic potential of the electrons in

two dimensions. By allowing the direct and several diffracted beams to combine results in an interference pattern which gives an enlarged picture of the periodic potential which is then further magnified by the lenses in the microscope. This interference pattern is an inverse-Fourier transformation of the diffraction pattern.

The light and dark spots of contrast in a HRTEM image do not necessarily relate directly to columns of atoms and the spaces between then. These fringes do allow however for the structure of the material to be qualitatively investigated. Fig 3.20 is a HRTEM image of microtwin lamellae in a crystalline Si matrix. The mirror reflected crystalline structure of the microtwins is clearly visible.

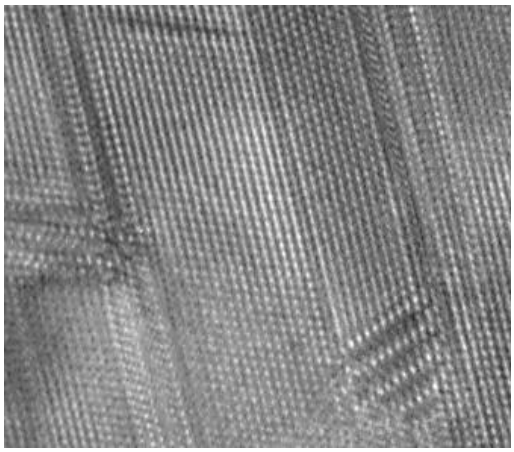

Figure 3.20: *HRTEM micrograph of microtwin lamellae in a c-Si matrix.*

Changes in the thickness of the sample and focus conditions alter the phase change experienced by the beams, and consequently the fringe pattern produced. Computer simulations of the perfect crystal and of defected crystals can be performed in order to produce reference images which can be compared to the real TEM image.

3.5.5 *In-situ* experiments

In an investigation such as the one undertaken during this study, TEM images produced of as-implanted and the associated bulk annealed samples

yield a "before and after" picture of damage recovery. The researcher therefore has to infer the possible mechanisms of defect evolution and interaction during annealing. Extra information can be obtained by observing the damage recovery *in-situ* during TEM. The evolution of defects during such experiments is not exactly comparable to that which occurs during annealing of a bulk specimen, as the thinness of TEM samples results in extra surfaces through which point defects can be lost or created. However, after taking account of this, these experiments can provide useful insight into the mechanisms of damage recovery during thermal annealing. During this investigation, *in-situ* experiments were carried out at the Laboratoire de Métallurgie Physique in Poitiers and at the University of Salford using a double-tilting heating stage in a JEOL 200CX microscope.

3.6 Image analysis

TEM images were either captured on photographic negative or on S-VHS videotape. The negatives were digitally scanned into a computer using an Epson 4990 photo scanner at a resolution of 1200 dpi. In order to analyse the defects captured on the negatives, the images were imported into Adobe Photoshop. In order to maximise contrast pertaining to defects, the images were subject to a high pass filter, and the levels were adjusted.

The videos of the *in-situ* experiments were digitised in order for individual frames to be analysed.

3.7 References

1. Carter, D.B. and Williams. C.B. *Transmission Electron Microscopy* ed. Plenum. 1996: New York.
2. Gandy, A.S., Donnelly, S.E., Beaufort, M.F., Vishnyakov, V.M., and Barbot, J.F. *The effect of ion-beam specimen preparation techniques on vacancy-type defects in silicon.* Nuclear Instruments and Methods in Physics Research Section B: Beam Interactions with Materials and Atoms, 2006. **242**(1-2): p.610-613.
3. McCaffrey, J.P. *Small-angle cleavage of semiconductors for transmission electron microscopy.* Ultramicroscopy, 1991. **38**(2): p.149-157.
4. McCaffrey, J.P., Phaneuf, M.W., and Madsen, L.D. *Surface damage formation during ion-beam thinning of samples for transmission electron microscopy.* Ultramicroscopy, 2001. **87**(3): p.97-104.
5. Barna, A., Pecz, B., and Menyhard, M. *Amorphisation and surface morphology development at low-energy ion milling.* Ultramicroscopy, 1998. **70**(3): p.161-171.
6. Barna, A., Pecz, B., and Menyhard, M. *TEM sample preparation by ion milling/amorphization.* Micron, 1999. **30**(3): p.267-276.
7. B. Viguier and Mortensen, A. *Heating of TEM specimens during ion milling.* Ultramicroscopy, 2001. **87**: p.123.
8. Evans, J.H., VanVeen, A., and Griffioen, C.C. *The Annealing of Helium-Induced Cavities in Silicon and the Inhibiting Role of Oxygen.* Nuclear Instruments & Methods in Physics Research Section B-Beam Interactions with Materials and Atoms, 1987. **28**(3): p.360-363.
9. Ziegler, J.F. *Srim-2003.* Nuclear Instruments & Methods in Physics Research Section B-Beam Interactions with Materials and Atoms, 2004. **219-20**: p.1027-1036.
10. Beaufort, M.F., Donnelly, S.E., Rousselet, S., David, M.L., and Barbot, J.F. *Extended-type defects created by high temperature helium implantation into silicon.* Nuclear Instruments and Methods in

Physics Research Section B: Beam Interactions with Materials and Atoms, 2006. **242**(1-2): p.565-567.

11. Suder, S., Faunce, C.A., and Donnelly, S.E. *Thin solid film sample preparation by a small-angle cleavage for transmission electron microscopy*. Thin Solid Films, 1997. **304**(1-2): p.157-159.

Chapter 4

Characterisation of Xe implantation damage in Si

4.1 Introduction

Sections 2.7 and 2.8 described the damage produced following noble gas implantation and its evolution during thermal annealing. Many implantation and annealing conditions have been explored experimentally with a view to further understanding the damage accumulation and bubble formation processes in Si. He implantation has been extensively researched and the production of He bubbles in Si as a function of implant fluence and temperature, and their development into voids is well documented. Studies of heavier inert gas implantations such as Ar, Kr, Ne and Xe, have shown that at room temperature and below, amorphisation of Si occurs. TEM and RBS studies have yielded results which show that recrystallisation of these amorphous layers results in a polycrystalline structure. It has been reported that this is a result of the "recrystallisation-enhanced segregation" of the gas into bubbles, whose associated strain fields breaks the re-growth symmetry of the layer [1-4].

A recent investigation into the formation of bubbles in Ne implanted Si [5] showed, using TEM and RBS, that by implanting at elevated temperatures (250°C) amorphisation is inhibited. It was also reported that bubble formation occurs all along the Ne concentration profile which is contrary to that generally observed after He implantation, where a critical local concentration is required for bubble formation. Also reported was the retention of Ne in Si during thermal annealing. Ne has a lower permeability in Si than He, therefore Ne is retained in the sample during annealing. Ne bubbles migrate during sufficient annealing. When these bubbles intersect the surface of the material, they cause blistering and exfoliation of that surface.

Little other research has been conducted into high temperature implantations of heavy inert gases in Si, i.e. temperatures where amorphisation is inhibited. However, a greater understanding of radiation-induced damage accumulation and evolution during thermal annealing may be gained from such studies, as a wide variety of interstitial type defects may be formed, depending on implantation parameters and annealing temperatures.

Ion species plays an important role during damage accumulation, as is evident by comparing the resultant defect structures produced following He and Ne implantation at room temperature, for example. Implantation at room temperature using Xe leads to a similar morphology to that observed following implantation with Ne at room temperature, even though a Ne atom is considerable smaller than a Xe atom. Due to its size, Ne implantation should result in the production of less radiation induced damage compared to that produced by Xe implantation using the same implantation conditions. Therefore, at higher implantation temperatures, where radiation induced defects are mobile, different defect morphologies may be produced by the different ion species.

Therefore, it is envisaged that the defect structures produced by high temperature Xe implantation would be different to those produced by high temperature Ne implantation. Such differences in defect morphology may further aid our understanding of thermally activated defect mobility.

This chapter details a study conducted to investigate the damage formed in Si due to Xe implantation at high temperatures (350°C) and with a range of fluences. Cross-sectional TEM (XTEM) was used to investigate the resultant as-implanted and annealed defect structures with a view to obtaining an increased understanding of damage accumulation in Si produced after heavy inert gas implantation and thermal evolution of radiation induced defects.

4.2 Experimental procedure

All the experiments were carried out on Czochralski (Cz) grown n-type single crystal Si wafers with resistivity between 1-2 Ω cm. The majority of implantations were carried out at the Universidade Federal do Rio Grande do Sul in Brazil. TEM analysis of these samples found that they had been contaminated with Cu, possibly during implantation. In order to determine whether the presence of the Cu had affected the damage morphology observed, further implantations were performed at the Laboratoire de Métallurgie Physique in

Poitiers, France. For a concise list of implantations and the facilities where they were carried out, refer back to Table 1.1, p89.

Three sets of experiments were carried out on Si wafers. The room temperature implantation was performed in order to compare the damage morphology with the higher temperature implantations, and with results from previous studies.

1. Room temperature implantation (Brazil)
   - $1x10^{16}$ Xe ions/cm^2
   - 450keV
   - As-implanted

2. High temperature (350°C) implantations (Brazil)
   - $5x10^{15}$, $1x10^{16}$, $2x10^{16}$ or $5x10^{16}$ Xe ions/cm^2
   - 250keV
   - As-implanted, 600°C, or 800°C anneal for 30mins

3. High temperature (350°C) implantations (France)
   - $5x10^{16}$ or $1x10^{16}$ Xe ions/cm^2
   - 250keV
   - As-implanted or 800°C anneal for 30mins
   - Flux = 4 μA.cm-2

The implantation damage was studied by XTEM using a JEOL 200CX operating at 200keV. High resolution and Z-contrast images were produced using a JEOL 2200FS. The samples were prepared for XTEM using the tripod polishing technique, followed by bombardment with energetic Ar ions in either a Gatan Precision Ion Polishing System (PIPS) or Gata duo mill (DM) in order to achieve electron transparency. In order to image the cavities produced, the samples were tilted from their <110> orientation by a few degrees to reduce diffraction effects and the images were taken in either under-focus or over-focus to obtain Fresnel contrast. Descriptions of all these techniques are given in Chapter 3.

4.3 Results

1. Room temperature implantation

The implantation of $1x10^{16}$ Xe ions/cm^2 into Si at room temperature with an energy of 450keV results in the formation of a continuous damaged region extending from the surface to a depth of 480nm as shown in Figure 4.1. The selected area diffraction pattern taken of this region (shown inset) indicates that it is amorphous. The line of dark contrast is attributed to point defects unresolvable by TEM and constitutes the c/a interface.

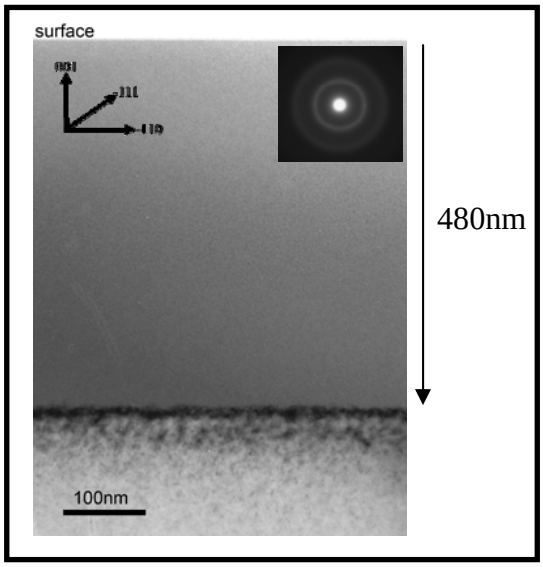

Figure 4.1: *[110] cross-section, bright field TEM micrograph of the damaged region formed in Si after 450keV Xe implantation with 1 x 10^{16} Xe ion/cm^2 at RT.*

2. High temperature implantation

Figure 4. 2 shows, in the form of a composite graph, the results obtained from TRIM calculations for Xe implantation with an energy of 250keV. TRIM calculations give the R_p of Xe ions as 110nm (distribution of Xe shown in red), and the maximum in the vacancy and interstitial distributions (green and black respectively) as 75nm. The amount of energy deposited per ion to the Si is shown in blue, where it can be seen that the energy loss is a maximum in a region from the surface up to a depth of about 60nm. From this latter result, one would expect to see, using TEM, the maximum amount of damage produced to also be in this region. Indeed, the a-layer produced during room temperature implantations, as shown in Fig 4.1, extends from the surface, corresponding to the region of maximum energy deposited to the Si. The total expected damage depth, as calculated by TRIM, is given as 200nm. However, implantation at high

temperatures results in enhanced defect mobility and a lateral spreading of the distribution profiles.

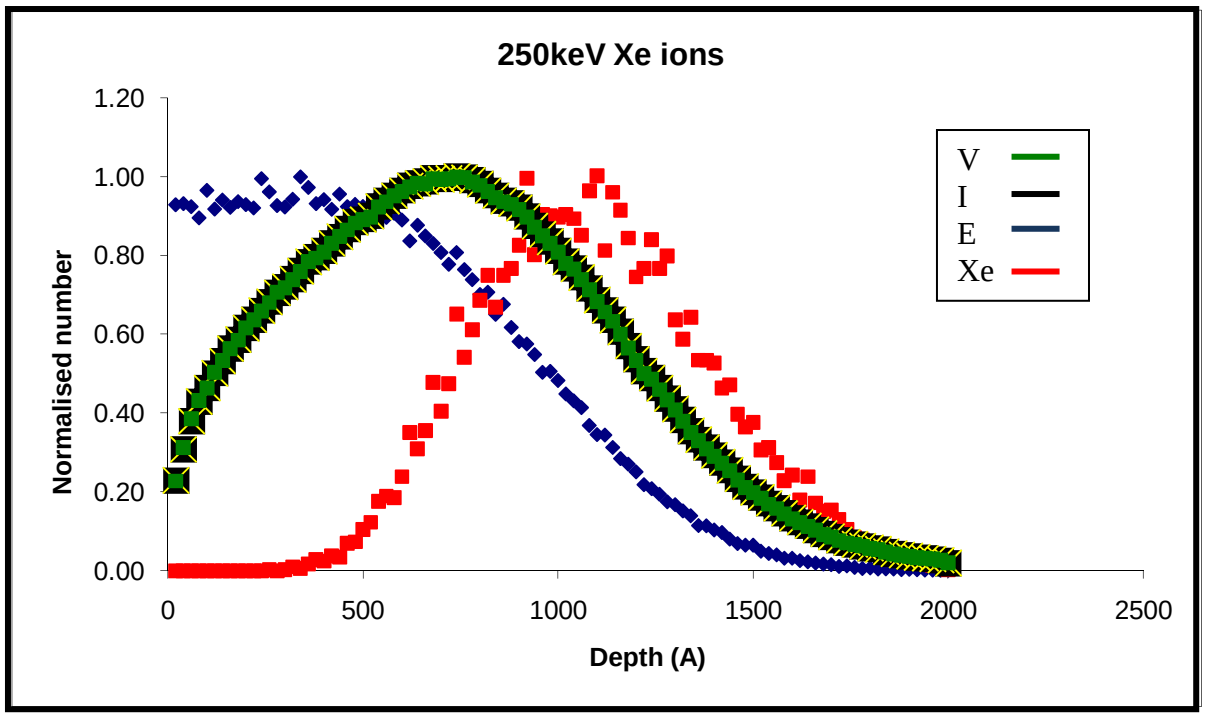

Figure 4.2: *Graph showing results of TRIM calculations for 250keV Xe ions implanted into Si. Energy deposited per ion to the Si is given in blue, Vacancy profile in yellow, interstitial profile in green, and Xe profile in red.*

Using TEM, it was found that in all of the samples implanted at 350°C a highly disordered region continuous from the surface to depths dependant on fluence was produced. For those samples implanted in Brazil, at fluences of $1x10^{16}$ Xe ions/cm^2 and above, the damaged region in the as-implanted samples consist of a buried amorphous layer, and crystalline regions containing point defects and / or bubbles, in front of and behind of this layer. A different morphology was found in those samples implanted with the same fluence but in Poitiers. Comparisons between samples implanted in Brazil and those implanted in Poitiers with a fluence of either 1 x 10^{16} Xe ions/cm^2 or 5 x 10^{16} Xe ions/cm^2 are given in Figs 4.4 and 4.16 respectively.

5 x 10^{15} Xe ions/cm^2 (as-implanted) implanted in Brazil

For low fluence implantations, a high density of dark contrast, characteristic of point defects, extends from the surface to a depth of about 300nm.

5 x 10^{15} Xe ions/cm^2 (800°C) implanted in Brazil

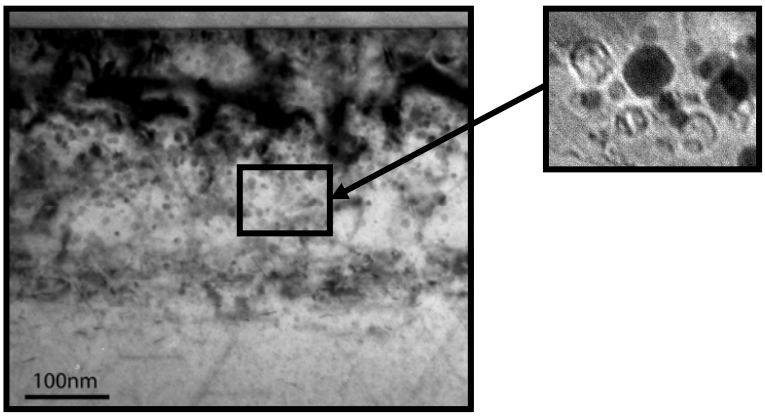

Figure 4.3: *[110] cross-section, bright field TEM micrograph of the damaged region formed in Si after 250keV Xe implantation with 5 x 10^{15} Xe ion/cm^2 at 350°C and after 800°C anneal for 30 minutes. The dark contrast inside the bubbles indicates contamination of the samples with copper.*

Figure 4.3 is a low magnification, bright field image tilted slightly off the Bragg condition which shows the defect structure following annealing at 800°C for 30 minutes. Small bubbles, of diameters of a few nanometres up to about 10nm, are visible in an area ranging from the surface up to a depth of about 350nm. The larger bubbles are faceted, whilst the smaller ones appear spherical. {311} defects are clearly visible behind the layer containing the bubbles. The total width of this disordered region, including the {311} defects, is about 600nm.

Under these imaging conditions, gas filled bubbles and cavities are usually defined by light contrast surrounded by a dark fringe. However, as the magnified image given in figure 4.3 shows, some of the bubbles are completely or partially filled with a material, yielding the very dark contrast visible. This contrast is an example of mass-thickness contrast, which is described in Chapter 3. Investigation of this material using electron energy loss spectroscopy (EELS) indicated that these samples contain Cu. The source of this Cu contamination is

not known conclusively but is thought to have come from the implanter used at the Universidade Federal do Rio Grande do Sul in Brazil as the implanter contains some copper components. In order to establish the source of the Cu and to investigate whether its presence perturbed the evolution of the defect structures during annealing, specimens were also implanted at the Laboratoire de Métallurgie Physique in Poitiers, France. Figure 4.4 shows bright field TEM images of samples implanted in Brazil and in Poitiers with 1 x 10^{16} Xe ions/cm^2. The figure shows the as-implanted samples, and those that have been annealed at either 600°C or 800°C for 30 minutes. Next to each image is a schematic showing the damage observed using TEM. The dashed red line indicates the surface of the samples.

Figure 4.4 clearly shows the evolution of the defects during thermal annealing. The difference between the morphology of the samples implanted in Brazil and is Poitiers is also obvious. Both aspects are described and discussed in more detail below.

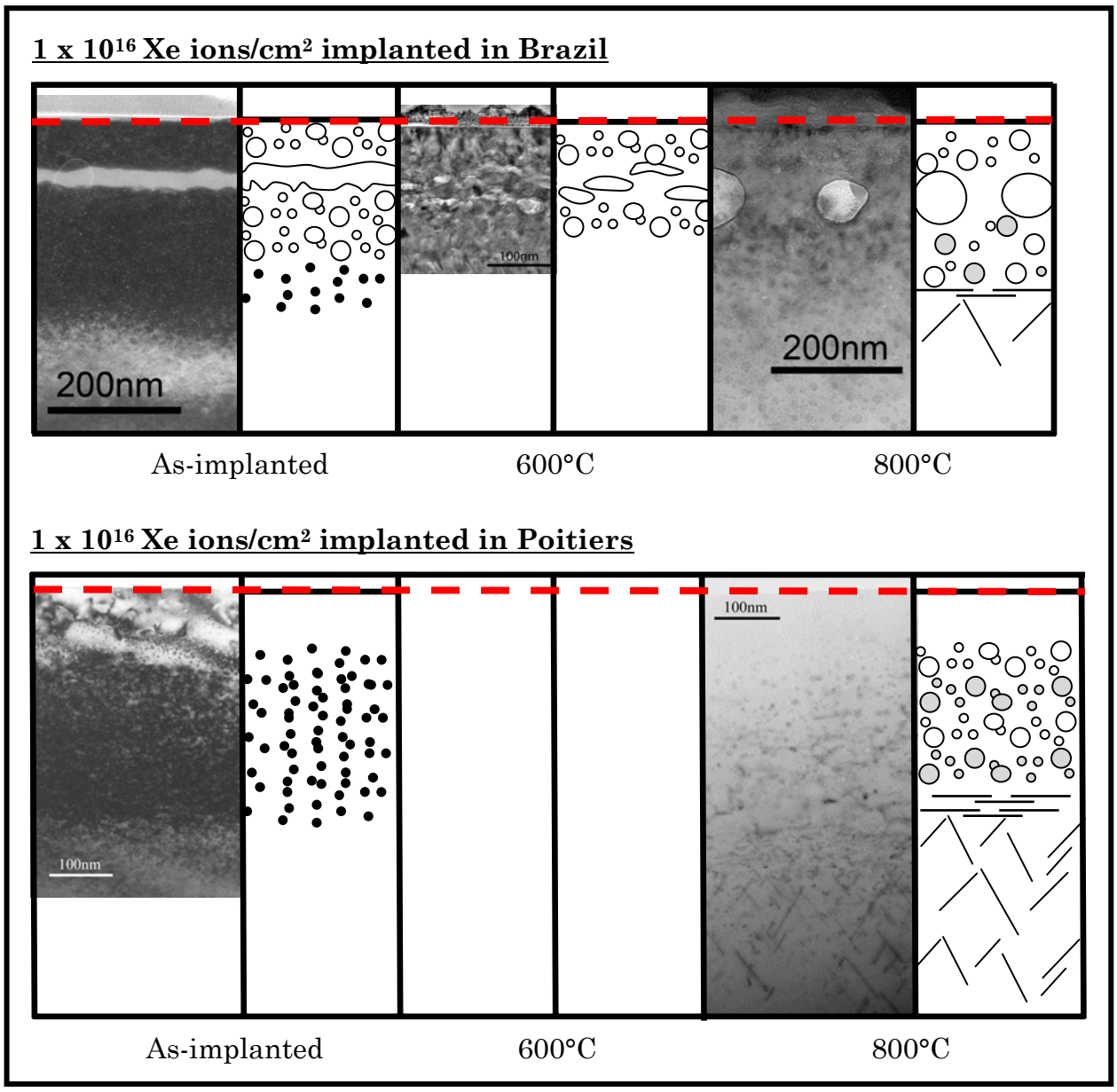

Figure 4.4: *Bright field TEM images and corresponding schematics of samples implanted in Brazil and in Poitiers with a fluence of 1 x 10¹⁶ Xe ions/cm². The figure shows the as-implanted samples and those annealed at either 600°C or 800°C for 30 minutes.*

1 x 10¹⁶ Xe ions/cm² (as-implanted) implanted in Brazil

The total defect structure extends to a depth of about 350nm. The band of light contrast, approximately 30nm wide and 80 nm from the surface, is an amorphous layer. This was confirmed using SAD of that area where diffuse rings were visible. The deep area of dark contrast is approximately 220 nm wide.

Figure 4.5 is a bright field TEM image which shows a magnified view of the structure of the amorphous layer. The sample was slightly tilted off Bragg and underfocused in order to image the bubbles and precipitates present. The triangular structure in the top left hand corner of this image is attributed to the glue which is used during preparation of the sample, and should be ignored. Bubbles of dark and light contrast are visible both in front of and behind the a-layer. The bubbles range in diameter from a few nanometres to about 20nm. Their shapes vary greatly; the smaller ones and those behind the layer appear spherical, whereas the larger ones in front of the layer tend to be irregular in shape.

The contrast in the a-layer under these conditions indicates the presence of bubbles. A clear difference in structure can be seen by comparing this layer to the a-layer in figure 4.1. In addition, the interfaces of this a-layer are irregular, which differs from the interface produced after room temperature implantation.

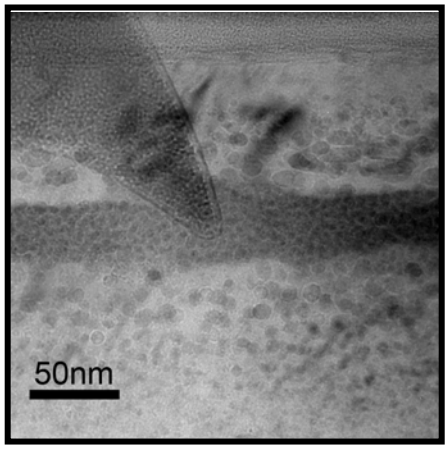

Figure 4.5: *[110] cross-section, bright field TEM micrographs of the damaged region formed in Si after 250keV Xe implantation with 1 x 10^{16} Xe ion/cm^2 at 350°C. Sample was tilted slightly off Bragg in order to image the bubbles.*

1 x 10^{16} Xe ions/cm^2 (600°C anneal) implanted in Brazil

A layer of highly irregular and elongated bubbles can be seen in a band about 130nm wide, extending from approximately 40nm below the surface. At this temperature the a-layer has recrystallised epitaxially.

1 x 10^{16} Xe ions/cm^2 (800°C anneal) implanted in Brazil

Figures 4.6 and 4.7 give the defect structures produced following an 800°C anneal for 30 minutes.

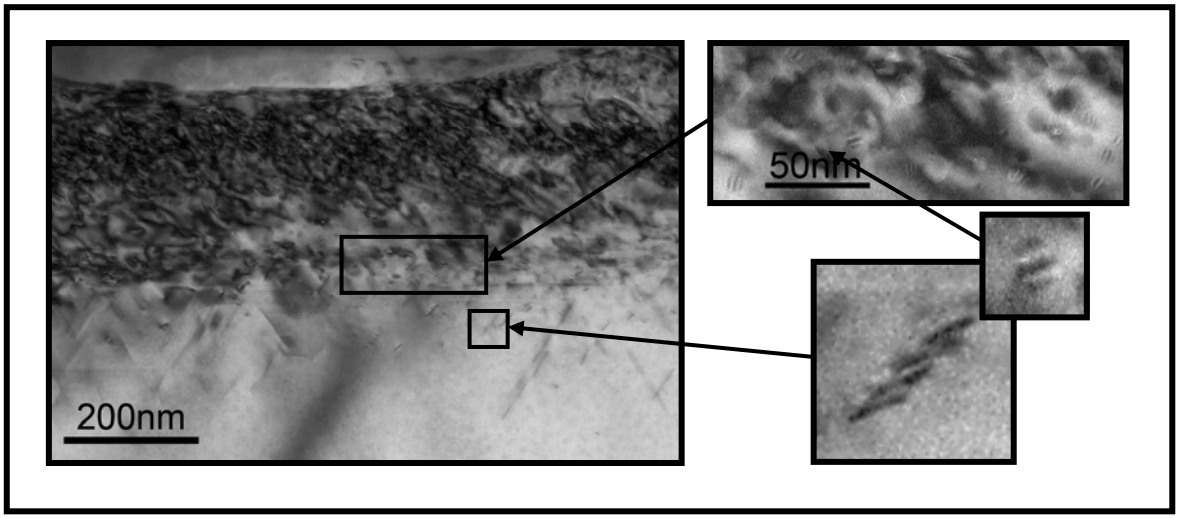

Figure 4.6: *[110] cross-section, 2-beam using [-111], TEM micrograph of the damaged region formed in Si after 250keV Xe implantation with 1 x 10^{16} Xe ion/cm^2 at 350°C and following an 800°C anneal . The top right hand image is a magnified section showing circular defects identified by Moiré fringes. The bottom right hand image if of a ribbon-like defect.*

Figure 4.6 is a 2-beam image, produced using [-111]. Small Moiré fringes, indicative of a crystalline structure with a different lattice spacing to that of the surrounding matrix, are visible, as is shown in the top right hand magnified images. The bottom image shows a ribbon-like defect.

The area containing {311} rod-like and, as is shown in Fig 4.6, ribbon-like defects, extends from the area of dark contrast to about 240nm, resulting in a total defect layer of about 600nm.

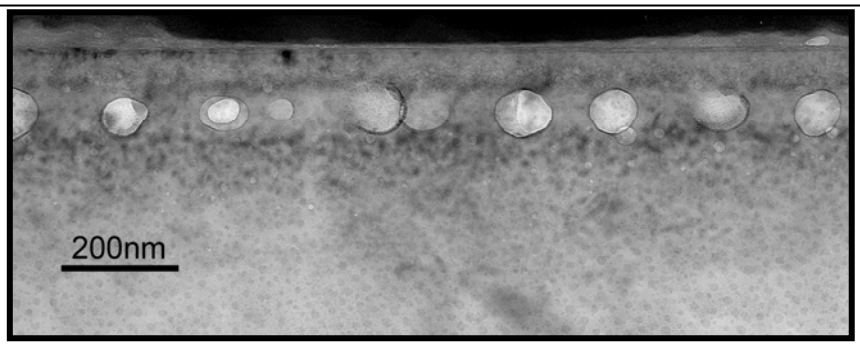

Figure 4.7 *[110] cross-section, bright-field TEM micrograph of the damaged region formed in Si after 250keV Xe implantation with 1 x 10^{16} Xe ion/cm^2 at 350°C and following an 800°C anneal. This image was tilted slightly off Bragg in order to image the bubbles (imaged in underfocus).*

The sample in Figure 4.6 was tilted slightly off Bragg in order to reduce the contrast and give the image shown in Figure 4.7. A line of relatively large bubbles is clearly visible. This bubble band is about 100nm wide and begins about 80nm from the surface. These large bubbles are not faceted. Smaller bubbles can be seen in front of and behind this band. A higher density of bubbles exists in the area nearest the surface. These smaller bubbles, both behind and in front of the large bubble band, range in size from about 3nm to about 25nm.

In underfocus conditions dark contrast can be once again seen in many of the bubbles, including 2 of the large bubbles, which would normally be light in contrast under these conditions, indicating the presence of a higher Z element within the bubble.

1 x 10^{16} Xe ions/cm^2 (as-implanted) implanted in Poitiers

Figure 4.8 shows the defect structure produced following implantation with 1x10^{16} Xe ions/cm^2 at the facility in Poitiers. The image on the left (a) is a down-zone [110], bright field image. A layer of dark contrast about 250nm wide is produced. This contrast is attributed to point defects and defect clusters. Towards the surface, small "dots" of light contrast on a dark fringe and dark contrast on a light fringe are visible. The image on the right (b) is the corresponding WBDF image, produced using 1g 7g [-111]. The bright contrast in the WBDF image also suggests the existence of small defect clusters.

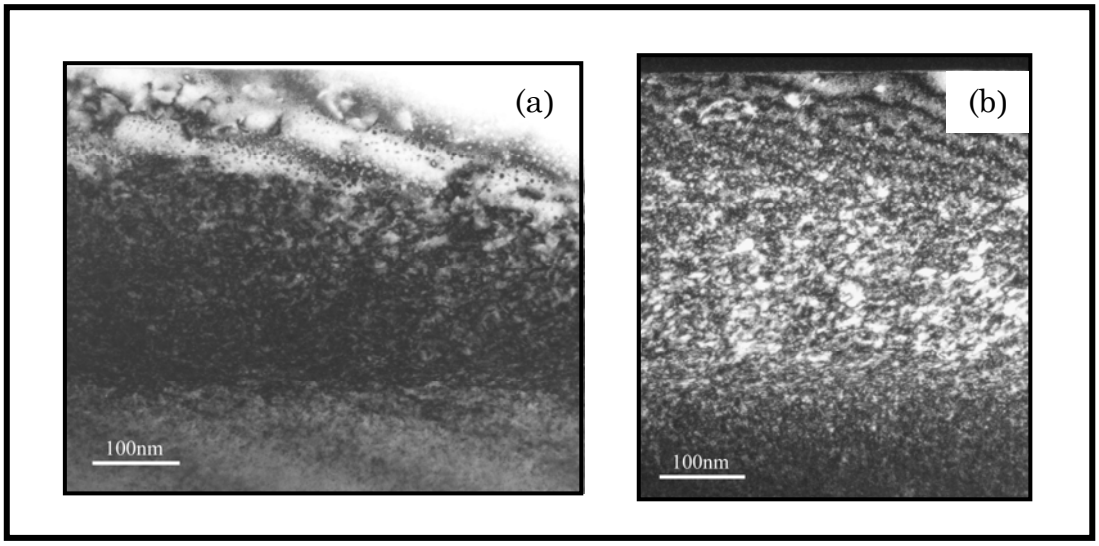

Figure 4.8: *(a) is a [110] cross-section, bright-field TEM micrograph of the damaged region formed in Si after 250keV Xe implantation with 1 x 10^{16} Xe ions/cm² at 350°C. (b) is a weak beam dark field image of the sample on the left, produced using 1g 7g [-111].*

By comparing this to the images of the as-implanted sample implanted in Brazil, in Figures 4.4 and 4.5, it can be seen that an a-layer was produced in the sample implanted in Brazil, whereas no a-layer was produced in the sample implanted in Poitiers with the same fluence. In the bright field micrographs, dark contrast, ascribed to non-crystallographic defects, is visible in the images of both as-implanted samples. The overall damaged area in the sample implanted in Brazil is 100nm wider than in the sample implanted in Poitiers as shown in Figure 4.8.

1 x 10^{16} Xe ions/cm² (800°C anneal)implanted in Poitiers

Figure 4.9 shows the defect structures produced following an 800°C anneal of the above sample. A defect layer, extending in excess of 600nm has been produced. About 100nm below the surface small bubbles are visible, about 10nm in diameter. This bubble zone extends to about 300nm below the surface. Behind this layer {113} defects have been produced.

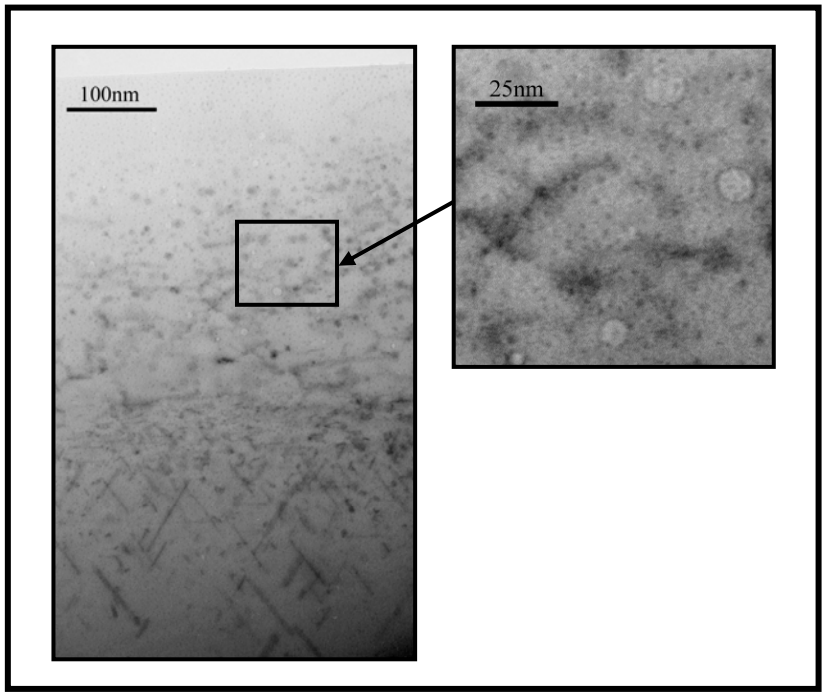

Figure 4.9: *[110] cross-section, bright-field TEM micrographs of the damaged region formed in Si after 250keV Xe implantation with 1 x 10^{16} Xe ions/cm^2 at 350°C, followed by 800°C anneal. The image on the right is a magnified view of the area specified on the sample on the left. The sample was tilted slightly off Bragg.*

Figure 4.10 shows WBDF images of this sample. The images were produced using 1g 7g [-111]. In the first defect band, corresponding to the bubble band in the bright field image, many circular defects are visible. These defects contain Moiré fringes, as can be seen in the 2-beam image of that area in Figure 4.11.

In between this area and the area containing the {113} defects, is an area about 150nm wide containing line defects which extend in the [110] direction, parallel to the surface. Behind this region, an area containing {113} rod-like and ribbon-like defects is visible.

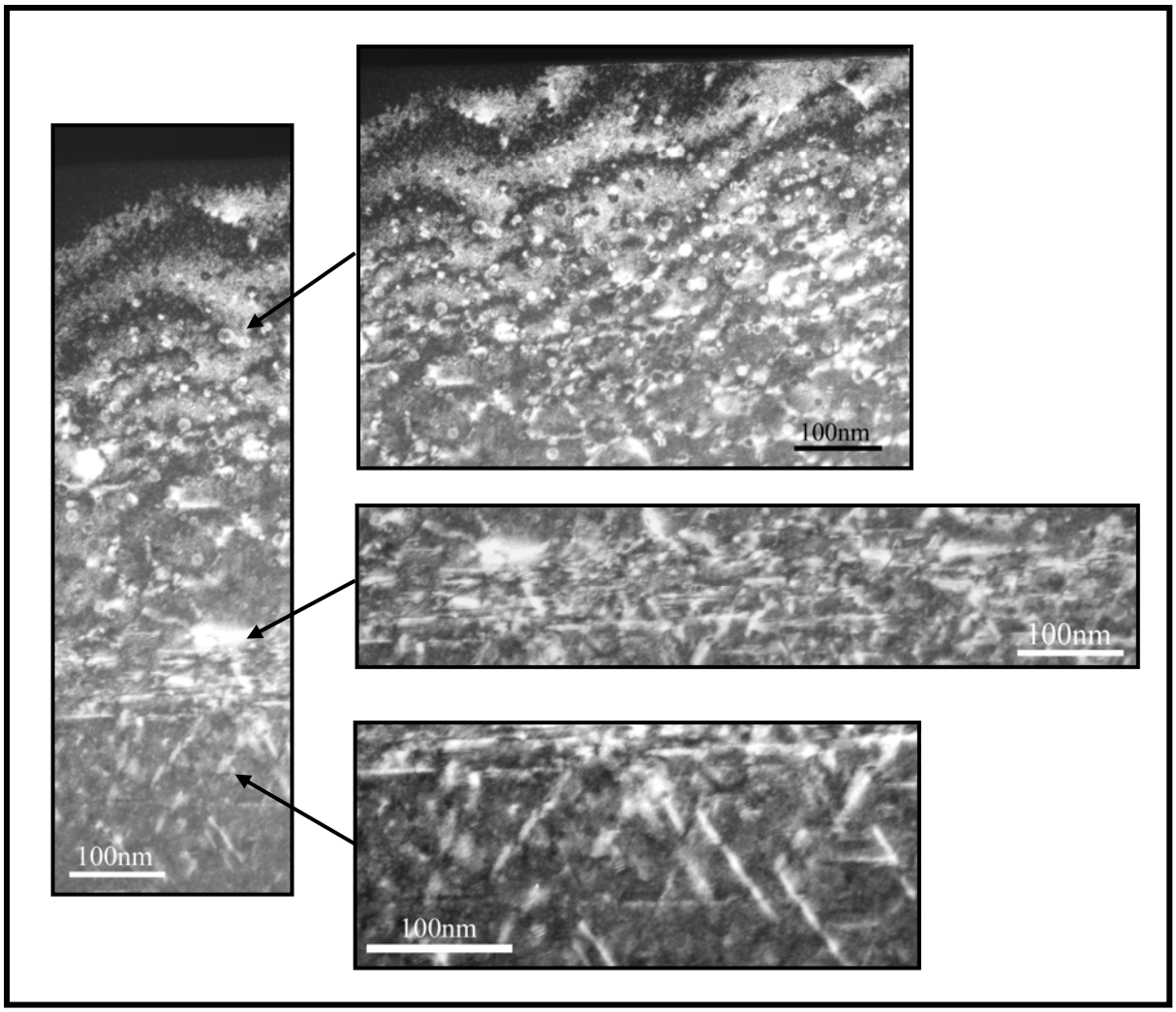

Figure 4.10: *[110] cross-section, WBDF TEM micrographs using 1g 7g [-111] of the damaged region formed in Si after 250keV Xe implantation with 1 x 10^{16} Xe ion/cm² at 350°C, followed by 800°C anneal. The three images on the right hand side are magnified views of the sample on the left hand side.*

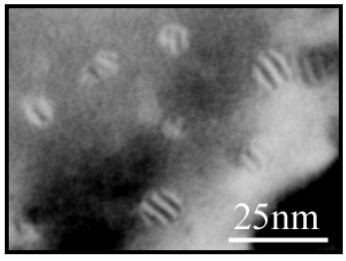

Figure 4.11: *2-beam using [-111] TEM micrograph showing defects containing Moiré fringes.*

Moiré fringes are produced when two crystallographic structures of differing lattice spacings overlap. Therefore, it was concluded that these defects must be crystallographic in nature; with the possibility of them being Xe precipitates. In order to investigate further this hypothesis, the defects defined by Moiré fringes

were analysed using Z-contrast imaging (Figure 4.12) and HRTEM (Figure 4.13) by D. Eyidi using a JEOL 2200FS. Defects comprising of atoms of different atomic mass to the surrounding matrix can be identified using Z-contrast imaging, and the crystallographic structure and lattice spacing of the defects can be deduced using HRTEM images. In the Z-contrast images, the defects were imaged as light particles on the darker surrounding Si matrix. This indicates that the defects are comprised of a material of higher atomic mass than Si.

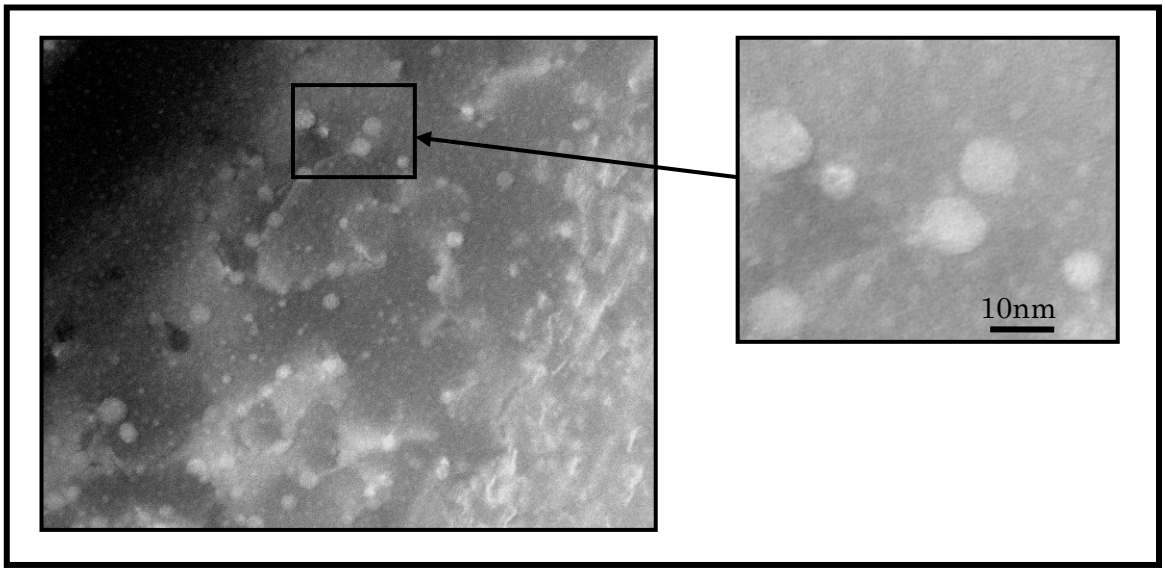

Figure 4.12: *Z-contrast images of the above sample. The light contrast indicates that these defects are comprised of an element of higher Z than Si.*

An HRTEM image of the defect is given in Figure 4.13. This image shows that defect is partially faceted, crystalline, and is epitaxially embedded in the Si matrix. The sizes of these defects range between 1 and 10nm. The Fourier transform of this imaged was produced which allowed the lattice spacing of the foreign material to be calculated, and found to be 6.1Å, corresponding to that of solid Xe. These defects, therefore, do not comprise of Cu.

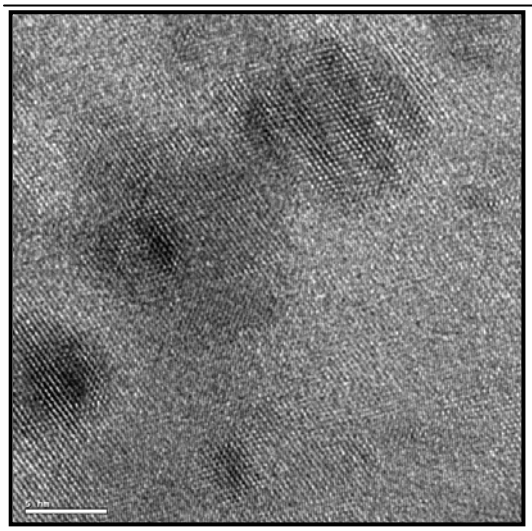

Figure 4.13: *High resolution TEM image showing the structure of the defects.*

Moiré patterns, {113} rod-like and ribbon-like defects are also observed in the samples implanted with $1x10^{16}$ Xe ions/cm^2 at the facility in Brazil and annealed at 800°C, as is shown in Figure 4.6. However, the sample implanted at the facility in Brazil contains a line of large bubbles of approximately 100nm in diameter, which is surrounded by small bubbles ranging in diameter from approximately 3 to 25nm; whereas the sample implanted at the facility in Poitiers contains an area about 300nm wide, relatively sparse with bubbles of approximately 10nm in diameter.

2 x 10^{16} Xe ions/cm^2(as-implanted)implanted in Brazil

Figure 4.14 is a bright field image showing the defect structure produced following implantation with $2x10^{16}$ Xe ions/cm^2 at the facility in Brazil. No corresponding samples implanted with Poitiers were produced. A crystalline layer containing bubbles extends from about 40nm from the surface to a depth of about 100nm. A buried a-layer, about 60nm wide exists beyond this layer. The c/a interfaces are irregular, and the contrast inside the layer is indicative of bubbles. Behind the a-layer an area of dark contrast, ascribed to point defects, is visible up to a depth of about 200nm. Inside this layer small bubbles are visible. The small bubbles in front of and behind the layer range in diameters from a few nanometres to about 20nm. This image was taken in underfocus, however many of these bubbles are dark in contrast. The total defect layer is about 360nm wide.

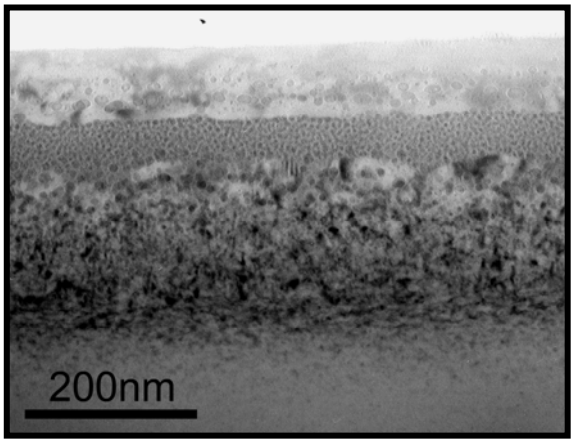

Figure 4.14: *[110] cross-section, underfocused, bright field TEM micrograph of the damaged region formed in Si after 250keV Xe implantation with 2 x 10^{16} Xe ion/cm^2 at 350°C. The sample was tilted slightly off the Bragg condition.*

2 x 10^{16} Xe ions/cm^2 (800°C anneal) implanted in Brazil

The image in Figure 4.15 shows the defect morphology following an 800°C anneal for 30 minutes.

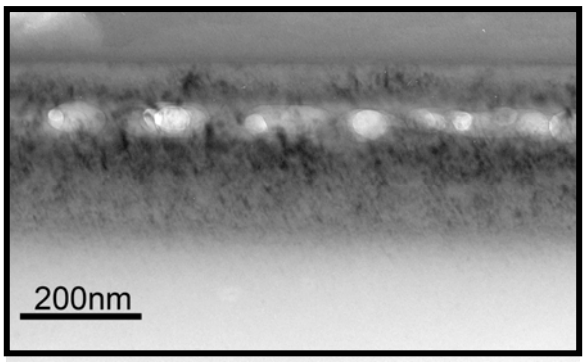

Figure 4.15: *[110] cross-section, bright-field TEM micrograph of the damaged region formed in Si after 250keV Xe implantation with 2 x 10^{16} Xe ion/cm^2 at 350°C and following an 800°C anneal. The sample was tilted slightly off the Bragg condition.*

Due to the artefacts produced during specimen preparation, a detailed analysis of the defect structures of this sample was not possible. Further, due to time constraints and equipment availability it was not possible to repeat the experiments in order for such an analysis to be carried out for use in this study. Therefore, the images are merely shown in this thesis in order to gain an idea of the width of the total defected area and to show that bubbles were produced in this sample.

The total width of the defect band visible is about 340nm. A large band of bubbles resides about 75nm from the surface and is about 55nm wide. Some of the bubbles in this band are elongated in the [100] direction, parallel to the surface.

Figure 4.16 shows bright field TEM images of samples implanted in Brazil and in Poitiers with 5 x 10^{16} Xe ions/cm^2, which are either in their as-implanted state, or have been annealed at either 600°C or 800°C for 30 minutes. Next to each image is a schematic showing the damage observed using TEM. The dashed red line indicates the surface of the samples.

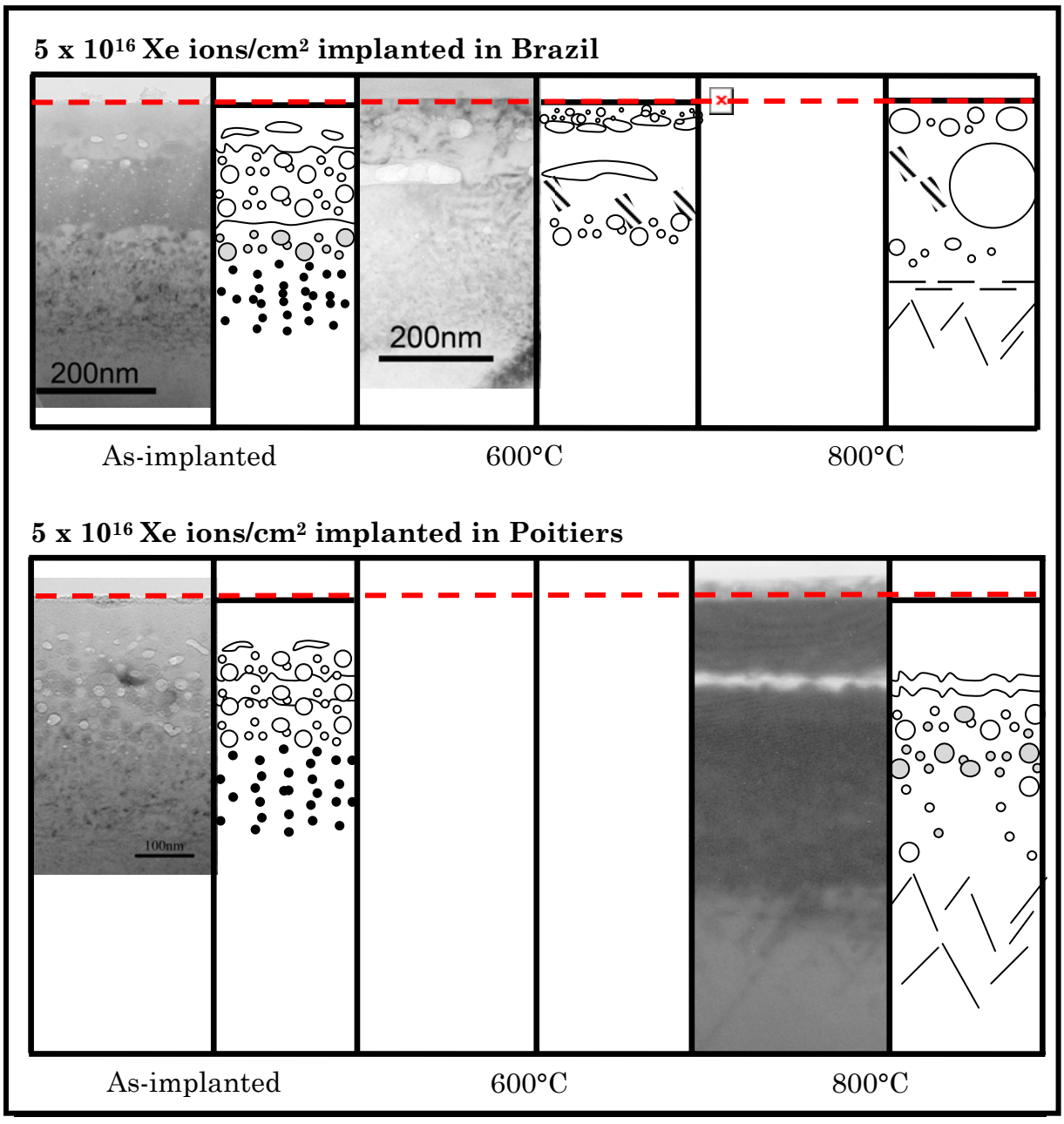

Figure 4.16: *Bright field TEM images and corresponding schematics of samples implanted in Brazil and in Poitiers with a fluence of 5 x 10^{16} Xe ions/cm^2. The figure shows the as-implanted samples and those annealed at either 600°C or 800°C for 30 minutes.*

By comparing the images in Figure 4.16, it can be seen that an a-layer is produced in both as-implanted samples, but the width of the layer in the sample implanted in Poitiers is much smaller and the interfaces between the amorphous layer and surrounding crystalline matrix is considerably more irregular compared to the interfaces in the sample implanted in Brazil.

All of the defect structures identified in Figure 4.16 are described and discussed in more detail below.

5 x 10^{16} Xe ions/cm^2(as-implanted) implanted in Brazil

Figures 4.17 and 4.18 show the defect structures produced following implantation with 5x10^{16} Xe ions/cm^2. The left hand image in Figure 4.17 is a [110] bright field image taken in underfocus, and tilted slightly off the Bragg condition. Under these conditions bubbles should appear dark with a light fringe, however many light bubbles are clearly visible, indicating that they are Xe precipitates. Bubbles of light contrast in the a-layer are also clearly visible. In this sample, the a-layer is about 120nm wide, and extends from about 90 nm below the surface. The defect layer behind the a-layer is about 190nm wide. The total defect area extends to about 400nm below the surface.

The bubbles in front of and behind the defect layer range in diameter from about 2nm to 30nm. In addition the shapes of these bubbles vary considerably, from small spherical bubbles to irregular, elongated bubbles. The c/a interface of the a-layer is irregular.

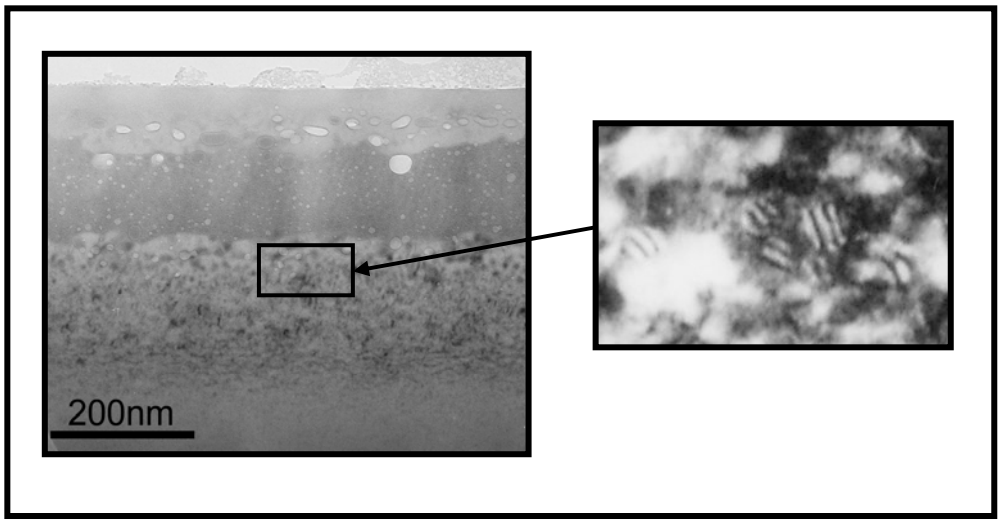

Figure 4.17: *[110] cross-section, bright-field TEM micrographs of the damaged region formed in Si after 250keV Xe implantation with 5 x 10^{16} Xe ion/cm² at 350°C. The image on the left was taken in underfocus with the sample tilted slightly off the Bragg condition. The image on the right is a WBDF image using 1g 7g [-111], magnified to show the area indicated. Moiré fringes are visible, indicating the presence of Xe precipitates.*

The right hand image in Figure 4.17 is a WBDF image of the area specified by the small box, produced using 1g 7g [-111]. Under these conditions, Moiré fringes are clearly visible.

Figure 4.18 is an overfocused image. The contrast of the majority of bubbles in the a-layer is greatly enhanced under these conditions.

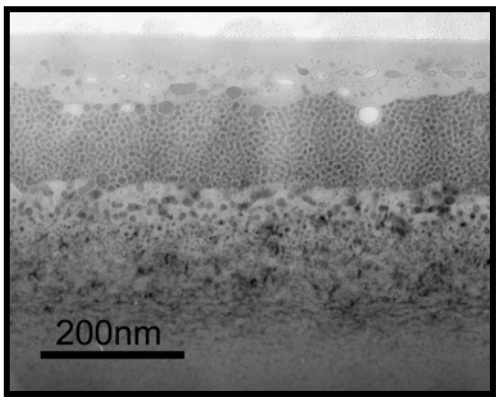

Figure 4.18: *[110] cross-section, bright field TEM micrograph of the damaged region formed in Si after 250keV Xe implantation with 5 x 10^{16} Xe ion/cm² at 350°C. Sample was tilted slightly off the Bragg condition.*

5 x 10^{16} Xe ions/cm^2 (600°C anneal) implanted in Brazil

The defect structures produced following a 600°C anneal of the above sample are given in Figures 4.19 and 4.20.

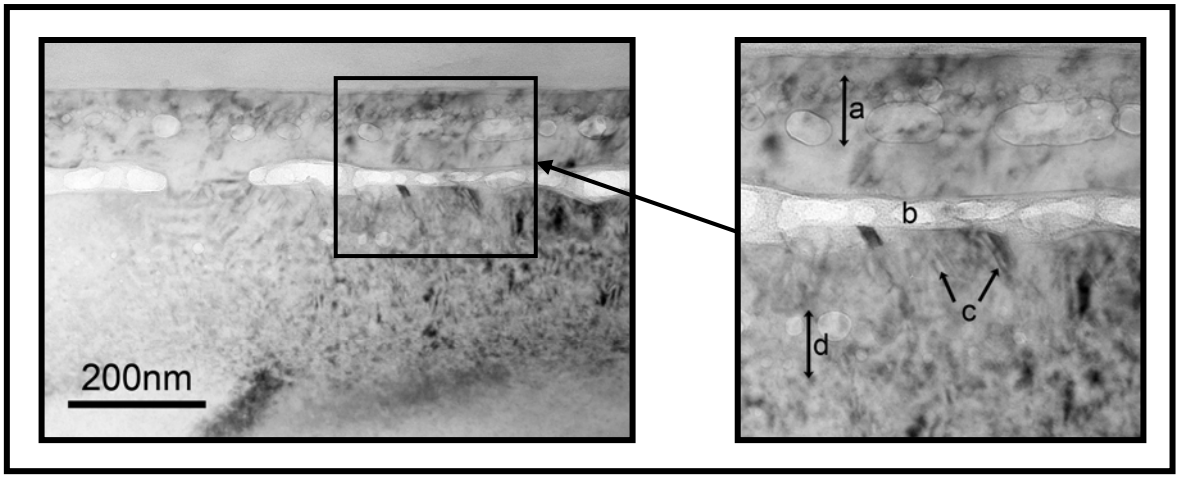

Figure 4.19: *[110] cross-section, bright-field TEM micrographs of the damaged region formed in Si after 250keV Xe implantation with 5 x 10^{16} Xe ion/cm^2 at 350°C, following a 600°C anneal for 30 minutes. The image on the right is a magnified view of the area indicated. The sample was tilted slightly off the Bragg condition*

Three distinct regions are visible in this image. A layer of various sized bubbles, about 50nm wide exists a few nanometres below the surface, denoted by **a** in the right hand image. These bubbles range in size from about 15nm to larger elongated bubbles. The elongated bubbles have dimensions of about 100nm x 35nm, the length extending in the [100] direction, parallel to the surface.

About 100nm below the surface a line of highly elongated bubbles exists, denoted by **b**. The width of this line is about 50nm, though is highly irregular, and, as the left hand image shows, terminates intermittently throughout the sample.

Another band of bubbles exists about 200nm from the surface, denoted by **d**. This layer is about 45nm wide and contains mainly near spherical-looking bubbles.

The contrast in **c** is attributed to microtwins.

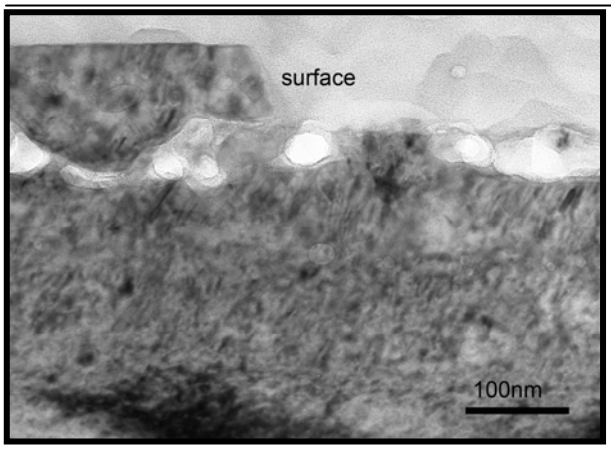

Figure 4.20: *[110] cross-section, bright field TEM micrograph of the damaged region formed in Si after 250keV Xe implantation with 5 x 10^{16} Xe ion/cm² at 350°C following a 600°C anneal for 30 minutes. The sample was tilted slightly off the Bragg condition.*

The result of the long, elongated line of bubbles can be seen in Figure 4.20, where the surface has been exfoliated.

5 x 10^{16} Xe ions/cm² (800°C anneal) implanted in Brazil

Figures 4.14 shows the defect structure following an anneal at 800°C for 30 minutes.

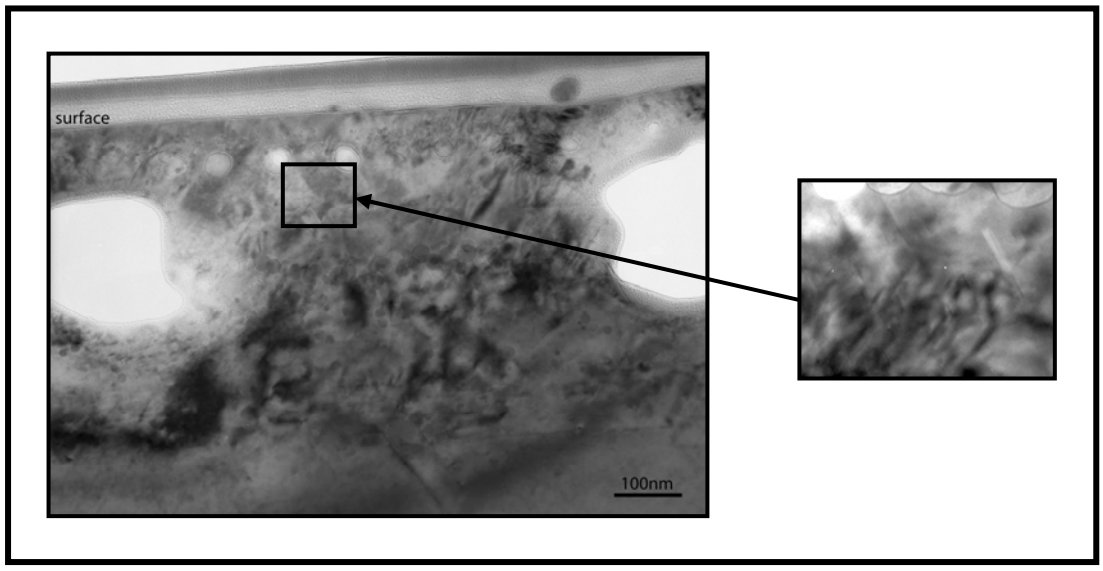

Figure 4.21: *[110] cross-section, bright-field TEM micrographs of the damaged region formed in Si after 250keV Xe implantation with 5 x 10^{16} Xe ion/cm² at 350°C, following a 800°C anneal for 30 minutes. The image on the right is a magnified view of the area indicated. The sample was tilted slightly off the Bragg condition*

In this image, very large voids of several hundred nanometres in size can be seen as well as many large holes where the bubbles have intersected one or both of the

surfaces created during the cross-sectioning process. This layer begins about 100nm below the surface and extends for about 200nm. Just in front of this layer another distribution of bubbles has been formed. These bubbles range in size from a few nanometres up to about 60nm in diameter.

The contrast in the magnified image in Figure 4.21 is attributed to microtwins Contrast from microtwins is discussed in more detail in the next chapter [6].

5 x 10^{16} Xe ions/cm^2(as-implanted) implanted in Poitiers

Figure 4.22 shows the defect structures produced following implantation with 5x10^{16} Xe ions/cm^2.

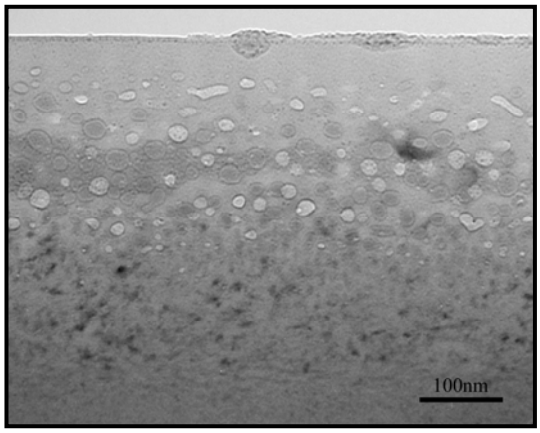

Figure 4.22: *[110] cross-section, bright field micrograph of the damaged region formed in Si after 250keV Xe implantation with 5 x 10^{16} Xe ion/cm^2 at 350°C. The sample was tilted slightly off the Bragg condition.*

The image in Figure 4.22 is a bright field image taken in underfocus. A band of irregular shaped bubbles is visible in an area extending from about 50nm from the surface up to a depth of about 270nm. There are small bubbles towards the deep end of this area, of a few nanometres in diameter. An a-layer extends from about 130nm to 200nm below the surface. This a-layer is very irregular in shape, even compared to the a-layers reported for the previous implantations. The total width of the defected material is about 500nm.

5 x 10^{16} Xe ions/cm^2(800°C anneal) implanted in Poitiers

The defect structure produced following an 800°C anneal for 30 minutes of the above sample is given in Figures 4.23 to 4.25.

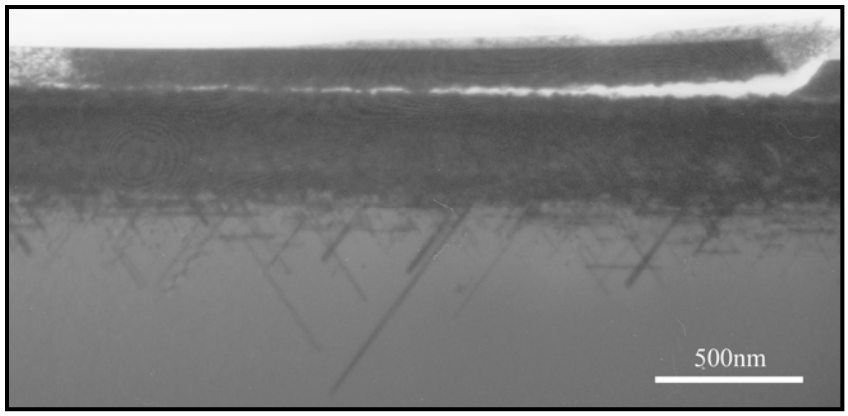

Figure 4.23: *[110] cross-section, low magnification TEM micrograph of the damaged region formed in Si after 250keV Xe implantation with 5 x 10^{16} Xe ion/cm^2 at 350°C, followed by an 800°C anneal for 30 minutes.*

The low magnification image in Figure 4.23 shows the total extent of the defected region. The surface has exfoliated along certain sections. An area of dark contrast about 600nm wide extends from the surface. {113} defects extend from this area to a depth of over 1200nm.

In Figure 4.24, the surface of the sample has exfoliated at a depth corresponding to where the buried a-layer was situated in the as-implanted sample. Circular defects of dark contrast, now attributed to solid Xe, resides in a band about 200nm wide. Behind this area {113} defects and ribbon-like defects have formed. This image was taken in overfocus conditions.

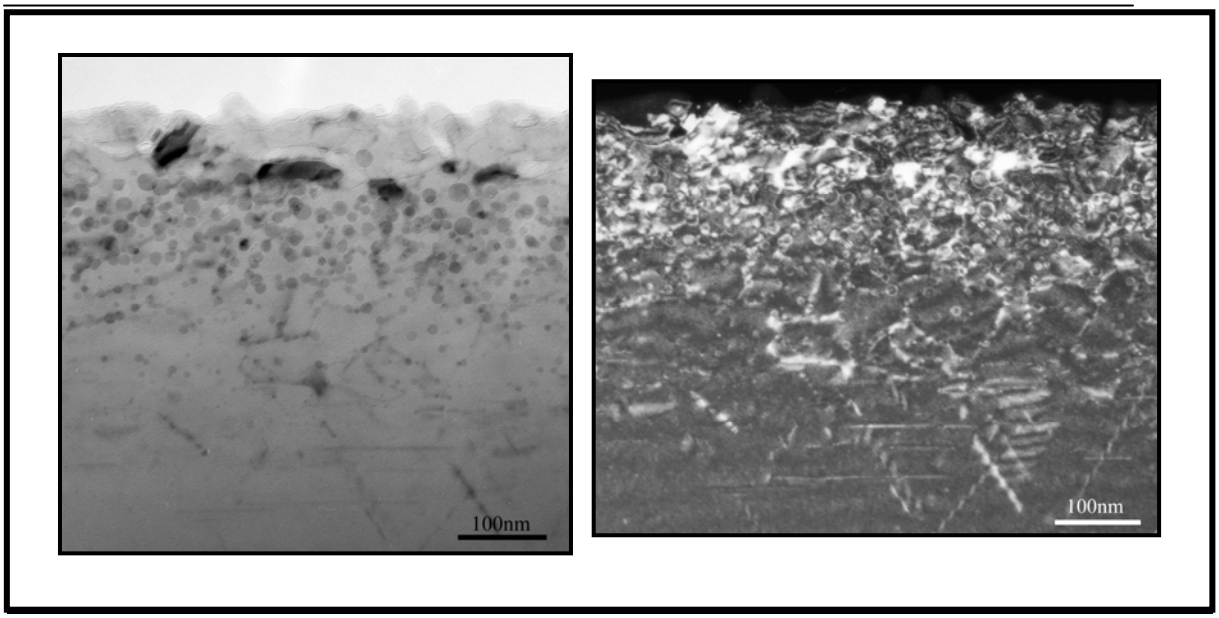

Figure 4.24: *[110] cross-section, micrographs of the damaged region formed in Si after 250keV Xe implantation with 5 x 10^{16} Xe ion/cm^2 at 350°C, followed by an 800°C anneal for 30 minutes. The picture on the left hand side is a bright field image where the sample had been tilted slightly off the Bragg conditions. The image on the right hand side is the corresponding WBDF image, produced using 1g 7g [-111].*

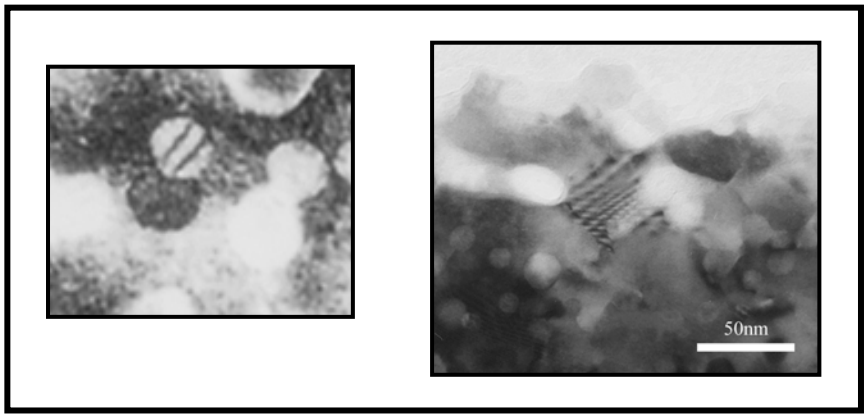

Figure 4.25: *The left hand image is a WBDF image, produced using 1g 7g [-111], showing the moiré fringes indicative of solid Xe precipitates. The right hand picture is a 2-beam image, produced using [-111], of the area containing these precipitates. This lattice-type contrast is visible in many samples.*

Initial inspection revealed that the defect structures of the corresponding samples implanted at the facility in Brazil were different from those implanted in Poitiers to a nominally identical fluence. However a more detailed comparison showed that this may have been due to a discrepancy in the implantation fluence measurements in one or other of the facilities. For example, the defect structures of the sample implanted with a measured $5x10^{15}$ Xe ions/cm^2 in Brazil are similar to those in the specimen implanted with a measured $1x10^{16}$ Xe ions/cm^2 at the facility in Poitiers.

For Ne implantations in Si in the Brazilian facility, quantitative measurements have been made of the amount of Ne in the Si following implantation to different fluences [5] and good agreement was found with the measured implanted fluence. This leads to the tentative conclusion that the dosimetry in the Brazilian facility was accurate indicating that it would appear to be the fluence measurements in Poitiers that are in error. However, other discrepancies may have occurred. The c/a interfaces in the samples implanted in Poitiers are considerably more irregular than the c/a interfaces in the samples implanted in Brazil, particularly at the lower amorphising fluence. This suggests that some dynamical annealing may have been taking place, which leads to a second conclusion that the implantation temperature during the Poitiers implantations was higher than during the implantations conducted in Brazil. In addition, the flux also has an effect on damage accumulation and annihilation. A discrepancy in the implantation flux could, therefore, also be a reason for the differences in defect morphology. These theories are under investigation.

The fact that the damage morphology of the samples implanted in the two facilities is similar (provided that one assumes an error of a factor of two in the fluence measured in Poitiers, or that the temperature or fluence of the implantations at the two facilities are different) leads to the conclusion that, the copper has little or no effect on the evolution of the defects during thermal annealing (other than the fact that it fills or part-fills some of the cavities). It is thought that the Cu was introduced during implantation as it was sputtered from the sample holder, and therefore, may have been recoil implanted. Cu is known

to be a fast diffuser, therefore, the deep damage imaged using TEM could have been produced by Cu diffusing a considerable depth into the sample during annealing, relative to the distance travelled by the defects which were produced by Xe implantation alone.

Summary of results – Brazilian implantations

Tables 4.1, 4.2 and 4.3 summarize some of the results obtained in this investigation.

as-implanted	Width of a-layer (nm)	Depth of layer from surface (nm)	Bubble sizes (diameters in nm)	Width of back defect band (nm)	Total width of defect layer (nm)
$5x10^{15}$	none	none	none	none	300
$1x10^{16}$	30	80	≤ 20	220	350
$2x10^{16}$	60	100	≤ 20	200	360
$5x10^{16}$	120	90	2 - 30	190	400

Table 4.1: *Summary of results obtained from TEM images of as-implanted samples*

600°C	Width of large bubble layer (nm)	Depth from surface (nm)	Bubble sizes (diameters in nm)	Width of back defect band (nm)	Total width of defect layer (nm)
$1x10^{16}$	130	40	< 50	\	\
$5x10^{16}$	50	100	15 - 100 [110]	\	\

Table 4.2: *Summary of results obtained from TEM images of 600°C annealed samples*

800°C	Width of large bubble layer (nm)	Depth from surface (nm)	Bubble sizes (diameters in nm)	Width of back defect band (nm)	Total width of defect layer (nm)
$5x10^{15}$	none	0	< 10	250	600
$1x10^{16}$	100	80	3 - 25	240	600
$5x10^{16}$	200	100	< 60	\	600

Table 4.3: *Summary of results obtained from TEM images of 800°C annealed samples*

Finally, Figure 4.26 gives a schematic overview (and provides the most easily comprehensible summary) of the complex damage morphology observed under

the different conditions. Clear trends can be seen in this representation as anneal temperature and fluence are varied and these will be discussed in the next section. This schematic was created using the TEM images of the samples implanted in Brazil. Note that, in this figure, the fluences measured at the Brazilian facility are assumed to be correct.

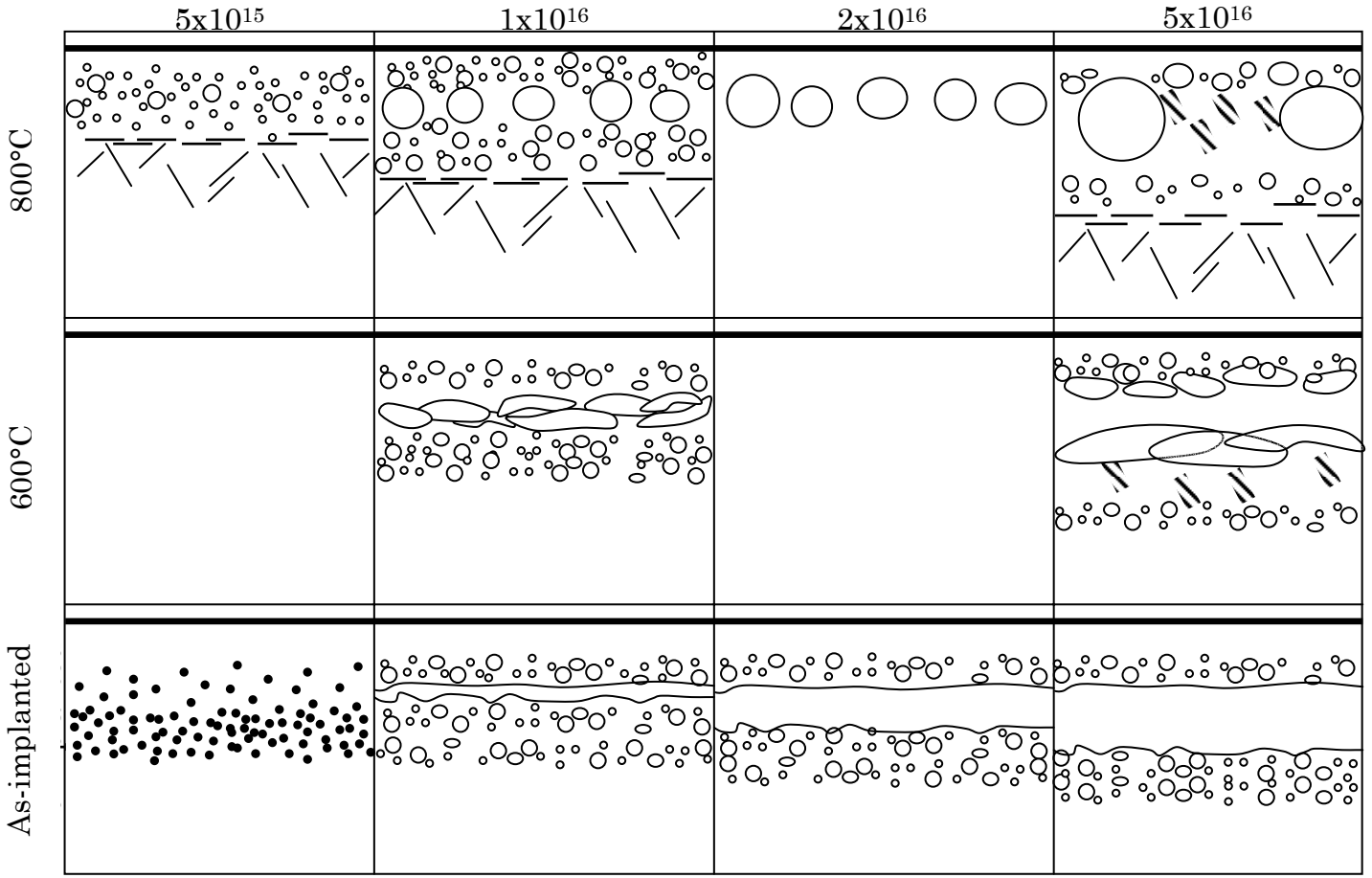

Figure 4.26: *Schematic showing the defect morphologies produced by 250keV Xe ions implanted into Si with an implantation temperature of 350°C and a range of fluences and annealing temperatures.*

4.4 Discussion

Amorphisation of Si occurs during implantations with Xe ions at 350°C only if the fluence is $1x10^{16}$ Xe ions/cm^2 or greater. Lower fluence implantations lead to a defected region extended from the surface to a depth of about 300nm. This region contains non-crystallographic defects and small defect clusters. Bubbles were not visible in the as-implanted sample, however they were produced following sufficient annealing, as is seen in Fig 4.3. This is in contrast to what occurs during He implantation at low fluences. If He bubbles are not produced in the as-implanted sample, then cavities will not be present in the annealed samples. As He has a high permeability in Si and therefore diffuses out through the material during annealing, small clusters of He bubbles must be formed in the as-implanted sample in order for He to form stable bubbles and evolve into cavities. These clusters are more stable than individual He atoms, therefore require greater thermal energy in order for the He to escape. The formation of clusters can be thought of as a competition between the arrival of the gas in the sample and permeation of the gas out of the material. For a given inert gas there will be an increased probability of cluster formation on annealing upon increasing the fluence of implanted gas. All of the heavier inert gases have a lower permeability in Si than He. Xe atoms can, therefore, not escape from the Si during annealing, allowing bubble precursors (presumably in the form of small, submicroscopic clusters) to form during implantation. On annealing the agglomeration of these precursors by Ostwald ripening or by migration and coalescence results in the formation of Xe filled bubbles in the annealed sample. Although much of the Xe is retained (within the bubbles) during annealing, Scanning Electron Microscope (SEM) images show flaking at the surfaces of samples implanted with $2x10^{16}$ and $5x10^{16}$ Xe ions/cm^2 following annealing at temperatures greater than 600°C, as shown in Figure 4.27. This flaking, which is undoubtedly caused by the presence of the Xe, will result in some of the gas escaping.

At fluences greater than $5x10^{15}$ Xe ions/cm^2, bubbles are visible in the as-implanted samples. These bubbles extend throughout the entire Xe distribution. This suggests that, whereas for He where the critical local concentration required for bubble formation exists around the maximum of the distribution profile, resulting in a line of bubbles being formed, the critical concentration required for Xe bubble formation is much less. This is unsurprising as (for a given bubble pressure – e.g. equilibrium pressure) the much greater size of Xe compared with He means that fewer of the former are required to form a bubble of a given size. The radiation enhanced diffusion of Xe, which occurs during implantation, results in the local concentration required for visible bubble formation being achieved over a wider area.

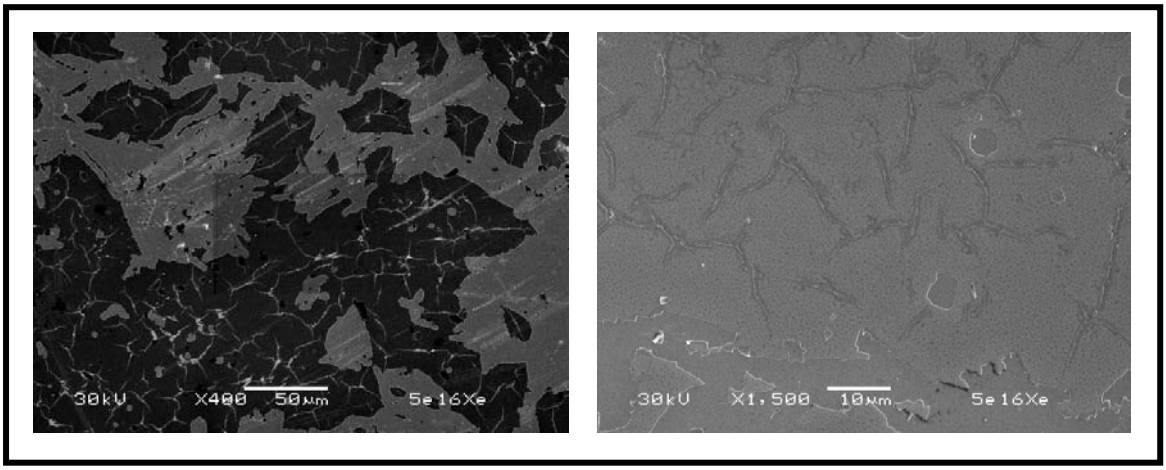

Figure 4.27: *Scanning electron microscope (SEM) images of the surfaces of samples annealed at 800°C for 30 minutes. The left hand image shows the extensive blistering and exfoliation of the surface of the sample implanted with 5 x 10^{16}Xe ions/cm^2. The right hand image is the blistering following implantation with 2 x 10^{16}Xe ions/cm^2.*

Xe precipitates, of sizes ranging from 1 to 10 nm have been found. These precipitates are formed when the pressure inside the bubble exceeds a threshold value, purported to be approximately 10Gp.

Buried a-layers are produced in the samples implanted with fluences of greater or equal to $1x10^{16}$ Xe ions/cm^2. The centre of the layer produced following $1x10^{16}$ Xe ions/cm^2 implantation corresponds to the mean projected Xe ion range R_p. Increasing fluence results in an increase in width of the layers. However the increase is towards the bulk of the material, and the position of the front a/c interface remains constant. This indicates that damage accumulation is slightly skewed towards the end of the Xe distribution profile, i.e. towards the end of range of the ion range.

The c/a interfaces of these layers are irregular, unlike those produced during room temperature implantations. Amorphisation occurs once a critical defect concentration is reached. This amorphous region grows layer by layer, leading to the sharp interfaces observed for low temperature implantations. One possible explanation for the irregularity of the interfaces may be the presence of bubbles inside the layer. These bubbles are visible on all the TEM images produced of the as-implanted samples. Their associated strain fields distort the lattice and so perturb the layer-by-layer growth. Another explanation could be dynamical annealing. During implantation there is a competition between damage accumulation and dynamical annealing, therefore greater flux is required for amorphisation at high temperatures. Comparing the buried a-layers to the layer produced during room temperature implantation shows that the overall width of the layers is greatly reduced. This is because diffusion of defects produced during implantation occurs such that they do not combine with other defects and from more stable defects near the ion track, therefore the critical concentration is not reached. However, because this diffusion is random, one could envisage a situation where in some areas the critical concentration is reached whereas in adjacent areas it is not, leading to the irregular interfaces observed. Low temperatures inhibit this diffusion, therefore implantations carried out at low temperatures result in sharp interfaces.

SPEG occurs at temperature upwards of 550°C, therefore in the TEM images of the samples annealed at 600 and 800°C, complete re-crystallisation of the buried layers has occurred. This recrystallisation also occurs in a layer by layer motion**.** In the 600°C samples, the position of the resultant bubble band coincides with the position of the a-layer in the as-implanted samples. The width of the bubble layer in the sample implanted with $5x10^{16}$ Xe ions/cm^2 is much smaller than that of the a-layer, and the bubbles are highly elongated along the [110] direction, parallel to the surface. This result suggests that the gas was swept by the two a/c interfaces during recrystallisation. A slightly different result is observed in the sample implanted with $1x10^{16}$Xe ions/cm^2, however, no inferences have been drawn from this as the artefacts produced during preparation of this specimen means that detailed analysis of the bubbles' position and shape were unable to be carried out. After annealing at 800°C, the elongated bubbles have coalesced into relatively large circular bubbles. This structure arises because the Xe has a very low permeability and therefore remains inside the bubbles even at 800°C, allowing for migration and coalescence. The apparent sweeping of the bubbles had been inferred in previous work [7] and the work reported in this chapter seems to provide strong confirmation that some such process is indeed occurring. As this could potentially give rise to technological applications, it was decided to carry out an investigation on this specific effect. This will be reported in detail in the next chapter.

Behind the buried a-layers there is a region containing bubbles, precipitates and (towards the back of this layer) interstitial defect clusters. These interstitial defects are formed during high temperature implantation when Si atoms are displaced from their lattice positions and travel deeper into the sample. This results in the vacancy profile being towards the surface, the maximum of the Xe distribution behind this and the interstitial distribution being at the greatest distance into the sample. Because of this separation of vacancies and interstitials, recombination and annihilation is limited.

Therefore, during annealing at 800°C, these defect clusters can evolve into a number of extended interstitial-type defects, in particular {113} defects, which are abundant in all the samples investigated.

4.5 Conclusion

High temperature implantations of Xe at fluences greater than or equal to $1x10^{16}$ Xe ions/cm^2 result in the production of buried a-layers. The width of these layers increases towards the bulk with increasing fluence. Xe bubbles are formed inside the layers and the bubbles appear to be swept by the c/a interfaces during SPEG. Because the Xe is retained during annealing, higher annealing temperature results in the migration and coalescence of the bubbles into large spherical bubbles, the sizes of which increase with increasing fluence.

Conversely to the case of He implantation, Xe bubbles are formed all along the Xe distribution profile, indicating that the critical local Xe concentration required for bubble formation is less than for He in Si and radiation-enhanced diffusion may allow the local concentration required to be achieved over a wider area. It has been shown that bubbles are produced in the annealed samples even though they are not formed in the as-implanted sample. This is due to the retention of Xe in the Si.

Solid Xe precipitates are formed in all the as-implanted and annealed samples studied.

4.6 References

1. Cullis, A.G., Seidel, T.E., and Meek, R.L. *Comparative-Study of Annealed Neon-Ion, Argon-Ion, and Krypton-Ion Implantation Damage in Silicon.* Journal of Applied Physics, 1978. **49**(10): p.5188-5198.
2. Wittmer, M., Roth, J., Revesz, P., and Mayer, J.W. *Epitaxial Regrowth of Ne-Implanted and Kr-Implanted Amorphous Silicon.* Journal of Applied Physics, 1978. **49**(10): p.5207-5212.
3. Revesz, P., Wittmer, M., Roth, J., and Mayer, J.W. *Epitaxial Regrowth of Ar-Implanted Amorphous Silicon.* Journal of Applied Physics, 1978. **49**(10): p.5199-5206.
4. Kennedy, E.F., Csepregi, L., Mayer, J.W., and Sigmon, T.W. *Influence of O-16, C-12, N-14, and Noble-Gases on Crystallization of Amorphous Si Layers.* Journal of Applied Physics, 1977. **48**(10): p.4241-4246.
5. Oliviero, E., Peripolli, S., Fichtner, P.F.P., and Amaral, L. *Characterization of neon implantation damage in silicon.* Materials Science and Engineering B, 2004. **112**(2-3): p.111-115.
6. Beaufort, M.F., Pizzagalli, L., Gandy, A.S., Oliviero, E., Fichtner, P.F.P., and Donnelly, S.E. *Solid-phase epitaxial regrowth of amorphous silicon containing helium bubbles* Journal of Applied Physics, 2008. **104**: p.094905.
7. Vishnyakov, V.M., Donnelly, S.E., and Carter, G. *The influence of impurities on the growth of helium-induced cavities in silicon.* Journal of Applied Physics, 2003: p.238.

Chapter 5

SPEG of He implanted buried amorphous layers in Si

5.1 Introduction

Results presented in Chapter 4 indicated that, during SPEG of buried amorphous layers, the c/a interfaces pushed the gaseous Xe into large elongated bubbles. In order to investigate further this "sweeping" effect further experiments were conducted and are detailed, with their results, in this chapter.

Apart from the lack of long range order, a-Si is considered to be similar in nature to c-Si; the atoms in both states are covalently bonded with four-fold co-ordination; under ion irradiation it is assumed that point defects, will be produced in a similar manner in both phases; the density of a-Si produced by ion implantation is only a few percent less than c-Si; the c/a interface is defined by bonding defects where thermal re-crystallisation is assumed to occur via a bond breaking and re-orientation mechanism. As at temperatures where SPEG begins, the mobility of inert gas bubbles in c-Si is minimal and where the behaviour of the bubbles in a-Si and c-Si is assumed to be the same, one would envisage a situation where the a-layer re-crystallises around the gas bubbles. However, the experiments presented in this chapter will show that this is clearly not the case, therefore other processes must be at work. This chapter is concerned with the investigation of these processes.

Because of the highly defected structures produced after Xe implantation at high temperatures (and not just a well-defined amorphous layer), exclusive investigation of the interaction between the c/a interfaces and the gas inside the layer is difficult. Results from TRIM calculations and previous TEM experiments [1-4] confirm that the same highly defected structures are produced in Si after Ne, Kr and Ar implantation. Ideally, a buried a-layer with sharp planar a/c interfaces and with the gas residing solely inside the layer is required for such an investigation, therefore another method must be employed to produce an a-layer containing ion-implanted inert gas. One possibility is to initially implant the Si with a non-gaseous ion species in order to produce a suitable "clean" buried a-layer, then to re-implant this layer with an inert gas with a well defined spatial distribution which lies entirely inside the layer. This chapter details such a

study and discusses the results obtained.

5.2 Results

This study involved multiple stages, where the resultant defect structures from each stage required investigation by cross-sectional transmission electron microscopy (XTEM) in order to determine the implantation and annealing conditions necessary to proceed with the subsequent steps. Each of the stages and its results are therefore detailed in this section.

All experiments were carried out on n-type, single crystal Si wafers of (100) orientation and with 1-2 Ω/cm. All He implantations were carried out at the Laboratoire de Métallurgie Physique in Poitiers, France; whereas the Li implantations were conducted at the Universidade Federal do Rio Grande do Sul in Brazil**.** Recovery of the implanted damage in the bulk samples was achieved using conventional tube furnaces with a vacuum of about 10^{-7} mbar.

All of the samples at the various stages of analysis were prepared for XTEM using the tripod polishing technique, followed by ion milling with low energy Ar ions in either a Gatan Precision Ion Polishing System (PIPS) or Gata duo mill (DM) in order to achieve electron transparency (as discussed in Chapter 3). Analysis of the samples was carried out using either a JEOL 200CX or JEOL 3010 transmission electron microscope operating at 200keV and 300keV respectively.

5.2.1 Li implantation

5.2.1.1 Experiment

Previous studies which utilised RBS techniques [5] showed that it was possible to produce a buried a-layer in Si by means of implantation with $7x10^{15}$ Li ions/cm^2 at LN_2 temperature and with an energy of 150keV. These findings were corroborated by results from TRIM calculations which gave the mean projected ion range R_p of the Li ions to be about 800nm. Wafers were therefore implanted

with Li under these conditions.

5.2.1.2 As-implanted Results

TEM analysis of the as-implanted sample shows the formation of a continuous disordered region from the surface up to a depth of 900nm, as shown in Figure 5.1. This damaged layer encompasses three regions, marked A, B and C. The central region, denoted B, is a 500nm wide amorphous layer, as can be deduced from the corresponding diffraction pattern shown inset. The regions denoted A and C are crystalline with area A beginning from the surface to a depth of 400nm, whilst C is 40nm wide. Both these regions are described by a black contrast that are ascribed to a high density of small defects which can not be individually resolved by TEM.

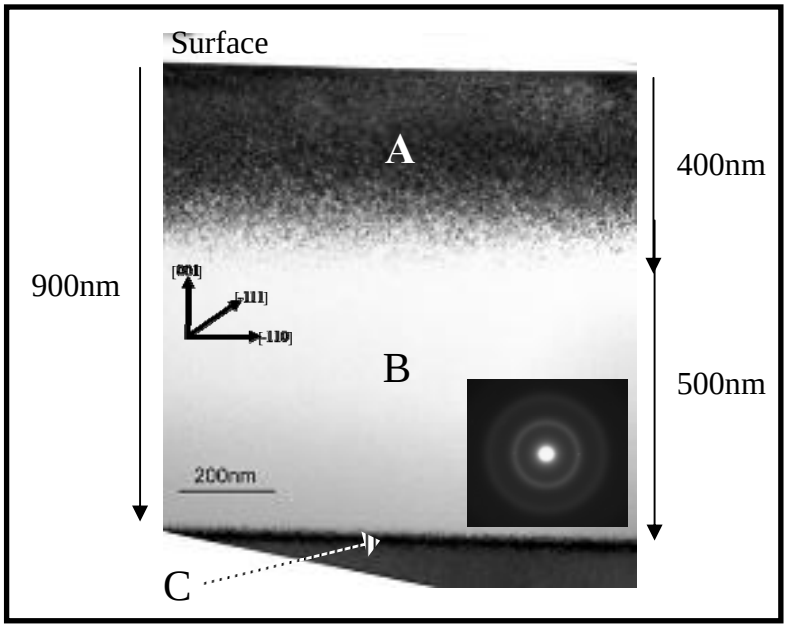

Figure 5.2: *[011] cross-section, bright field TEM micrograph of the damaged region formed in Si after 150keV Li implantation with 7x10^{15} Li ion/cm^2 at LN$_2$.*

Note that in contrast to the a-layers produced by Xe implantation at elevated temperatures, the a-layer appears to be free from TEM-resolvable defects and with a relatively sharp back a/c interface.

In order to remove the defects in region A and therefore produce the

desired sharp near-surface a/c interface, the samples were annealed at 400°C for 30mins under vacuum. This annealing step leads to the formation of a discrete line of defects 400nm below the surface and 50nm wide, as well as a sharpening of region C to a width of 20nm, as shown in Figure 5.2. These two lines of defects, shown as dark contrast, correspond to the two c/a interfaces, and are more regular than those formed following Xe implantation. The roughness visible at the a/c interface located nearest the surface is likely to be due to small crystallites within the layer which were formed during implantation and annealing.

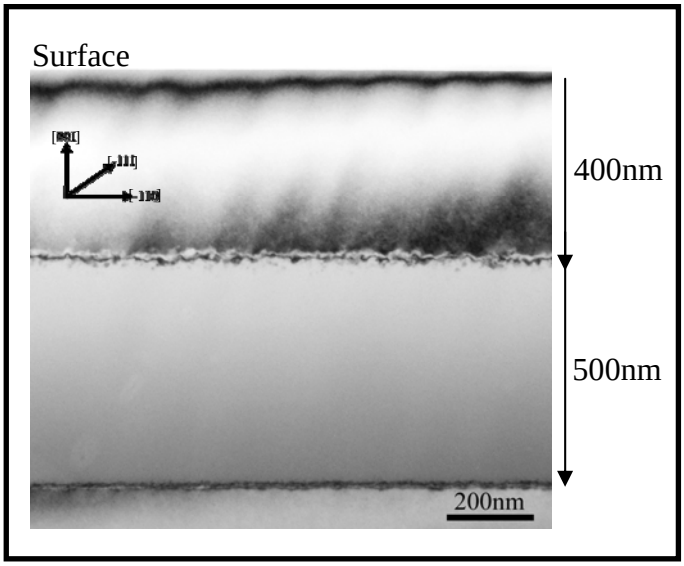

Figure 5.2: *[110] cross-section, bright field TEM micrograph of the damaged region formed in Si after 150keV Li implantation with 7x10^{15} Li ion/cm^2 at LN$_2$ temperature, and subsequent annealing at 400°C for 30mins.*

5.2.1.3 Results after annealing

Recovery of the a-layer shown in Figure 5.2 was achieved by a furnace anneal under vacuum at 600°C for 30mins. This was done without the presence of any gas in order to establish what, if any, defects are created during SPEG of such a layer. Three discrete lines of point defects are found at 400nm, 600nm and 900nm below the surface. The defects at 400nm and 900 nm correspond to the initial position of the two c/a interfaces, before annealing. The line observed at 600nm indicates where the two interfaces combined during re-

crystallisation and consists of point defect clusters. Re-crystallisation of a layer without the initial 400°C anneal, produced the same resultant structures as shown in Figure 5.3.

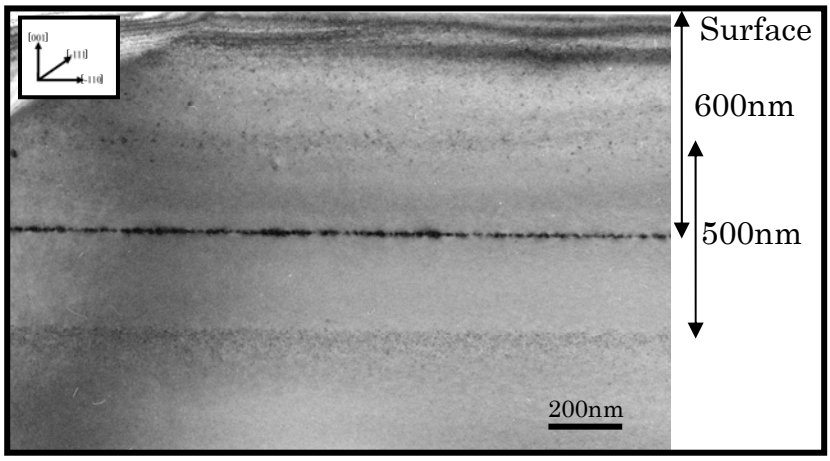

Figure 5.3: *[110] cross-section, bright field TEM micrograph of the damaged formed in Si after 150keV Li implantation with 7x10¹⁵ Li ion/cm² at LN_2 temperature and annealing at 600°C for 30mins.*

It was concluded that no appreciable damage resulted after re-crystallisation. The defects which were produced, i.e. point defects and defect clusters, are well understood and have been extensively discussed in section 2. Therefore, buried a-layers formed in this manner were deemed suitable to use in this investigation.

5.2.2 He implantation

He implantation into Si has been extensively studied, with a review given in Section 2.7. He implantation with energies in the keV energy range yield a He distribution which is well defined and close to Gaussian in nature. He is also chemically inert. It diffuses through the material, leaving at the surface, during thermal annealing at temperatures above approximately 700°C. All these facts suggest that He is a suitable candidate for use as the gas to implant into the a-layer in order to gain an insight into the interaction between bubbles and a moving a/c interface.

5.2.2.1 Experiment

The buried a-layers were implanted at RT with 2.5 x10^{16} He ions/cm^2 at 80keV. This energy was determined from TRIM calculations which indicated that the R_p of He was 600nm, corresponding to the centre of the amorphous layer. Bubbles are known to be formed in Si at RT with a minimum fluence of 2.5 x 10^{16} He ions/cm^2.

5.2.2.2 Results

Implantation of a buried a-layer with 80keV He results in the production of a bubble distribution with a peak at 600nm below the surface. This layer is 100nm wide in the [001] direction and consists of irregular shaped bubbles of varying sizes, all less than 15nm in diameter, as shown in Figure 5.4. The sample in this TEM image was pre-annealed at 400ºC for 30mins.

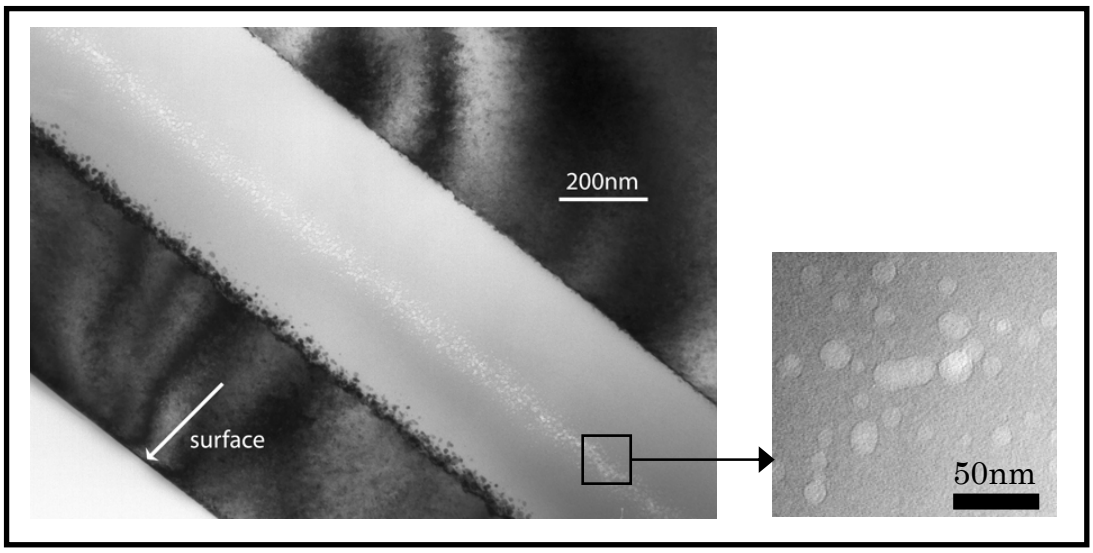

Figure 5.4: *[110] cross-section, bright field TEM image depicting the plane of bubbles formed inside a buried amorphous layer in Si after 80keV He implantation with 2.5x10^{16}He ions/cm^2 at RT .Kinematical diffraction condition; Underfocus.*

Figure 5.5 shows the bubbles in the a-layer (a and b) and those produced under the same implantation conditions but in c-Si (c). The bubbles in a-Si are significantly larger than those in c-Si.

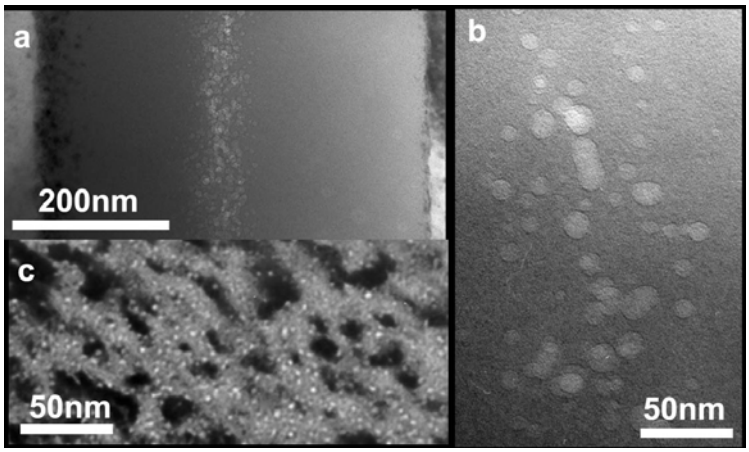

Figure 5.5: *Bright field TEM images of bubbles in a-layer (a and b) and a comparative image of bubbles formed under identical conditions in crystalline Si (c).*

5.2.2.3 Results after annealing

SPEG of the sample in Figure 5.4 was achieved after annealing in the bulk at 600°C for 30mins. The resultant defect structure is shown in Figure 5.6, which clearly illustrates that re-crystallisation of the amorphous layer results in a crystalline region containing defects. The resultant structure is greatly perturbed compared to that produced after the recovery of the He free layers.

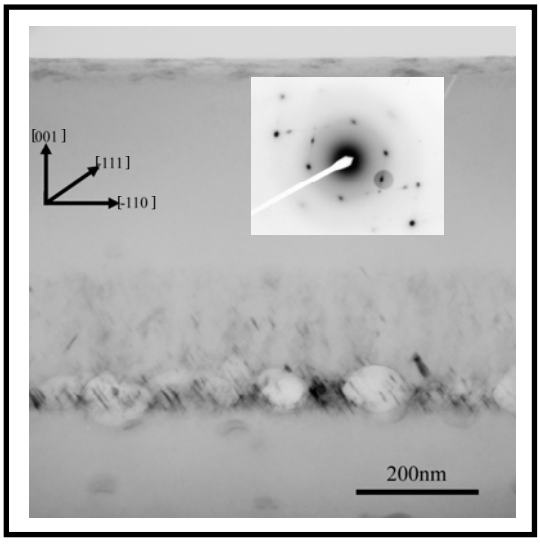

Figure 5.6: *[110] cross-section, bright field TEM micrograph of the resultant defect structure in Si following implantation with $7x10^{15}$ Li ion/cm² at LN_2, post-implantation with $2.5x10^{16}$ He ions/cm² at RT and annealing at 600°C for 30mins. Kinematical diffraction condition; underfocus.*

A band of dark contrast 250nm wide is observed 400nm below the surface. A distribution of bubbles 100nm wide is located 600nm below the surface. The

bubbles are slightly elongated in the [-110] direction and are on average about 100nm in length taken along that direction.

Similar dark contrast was found by Revez *et al* who amorphized Si by implanting with He at LN_2 temperature. They attributed it to point defects and defect clusters. However, the diffraction pattern of this area, shown inset, contains extra spots. Figure 5.7 is a dark field image, produced using one of these extra spots. It reveals that this contrast is due to microtwins, as was discussed in Chapters 2 and 3.

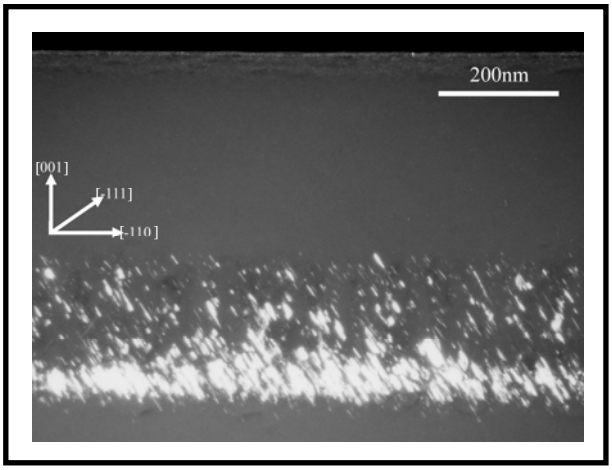

Figure 5.7: *[110] cross-section, dark field TEM micrograph depicting microtwins located in the (111) plane imaged with the extra diffraction spot.*

These microtwins are located in the (111) plane and increase in density in a layer around 600nm below the surface, corresponding to the location of the bubble and damage distribution. No microtwins exist behind the layer of bubbles, i.e. at a greater depth.

5.2.3 Discussion

Figure 5.8 shows the as-implanted and annealed samples together, in order to illustrate more clearly the morphology of these samples when they are annealed in the bulk. The peak in the cavity distribution has moved by approximately 60nm towards the surface following annealing. It is clear to see that the amorphous material at the back of the layer re-crystallises perfectly until it reaches the distribution of visible bubbles. The front section of the a-layer, however, contains a high density of microtwins beginning at a depth of

400nm below the surface, illustrating that imperfect re-growth occurred immediately on the onset of SPEG. One possible explanation for this a-symmetric re-growth can be realised upon closer inspection of the two a/c interfaces. The back interface is relatively planar with few point defects denoting the boundary between amorphousness and crystallinity. The front interface is rougher with what appears to be small crystallites in the amorphous material. Referring back to Chapter 2 and the work of Csepregi and Narayan, the undulating interface results in the formation of {111} facets, onto which microtwins form. Also, as the crystallites in the amorphous material are likely to be misorientated compared to the rest of the crystal, re-crystallisation will therefore also occur in different orientations.

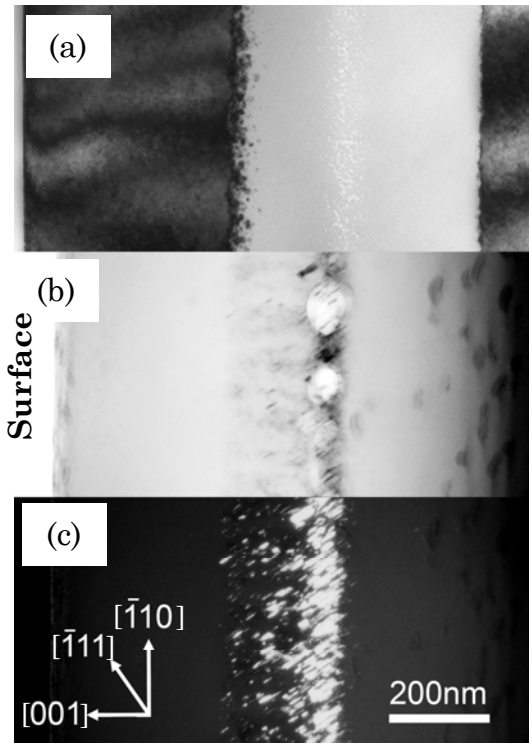

Figure 5.8: [110] cross-section, TEM images, where a) bright field image of the as-implanted sample, b) bright field image of the bulk annealed sample and c) dark field image of the bulk annealed sample, produced using one of the extra spots.

However, these statements alone cannot explain the formation of microtwins in these samples. The same a/c interface structures are present in the samples which have not been implanted with He and yet no microtwins are produced following SPEG in these cases. Narayan described the formation of microtwins in [100] Si when impurity concentrations reached a critical value. Results from TRIM calculations suggest that the interstitial defects produced during He

implantation reside in the front section of the a-layer, as illustrated by the green curve in Figure 5.9 (TRIM curves). If defect concentrations in this area exceeded the critical value as described by Narayan, this could explain the observed microtwin formation. By comparing Figure 5.9 to 5.8, it can be seen that microtwins are indeed formed in regions where the defect concentrations are above a certain threshold value.

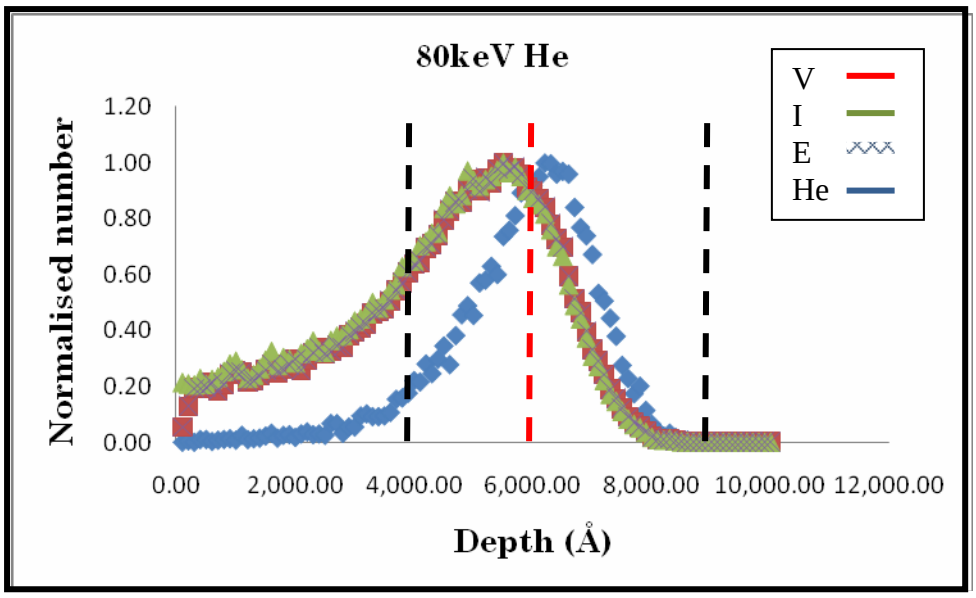

Figure 5.9: *Results from TRIM calculations of 80keV He implantation, presented as a composite graph. The vacancy and interstitial profiles are denoted red and green respectively and are produced during He implantation. The hatched blue line represents the energy imparted to the Si per He ion. The solid blue line represents the He distribution. The dashed black lines represent the c/a interfaces and the red dashed line represents the centre of the bubble band in Figure 5.4*

It is important to note that interstitial clusters are imaged using diffraction contrast and that this contrast mechanism is not available in a-Si. In previous studies [6] TEM images of c-Si implanted with He have shown the existence of interstitial clusters which evolve into extended defects such as {311} rod-like and ribbon-like defects or dislocation loops during annealing. Therefore, it can be assumed that interstitial-clusters may also be present inside the a-layer, although not visible on the TEM images presented here. The presence of interstitial defects in the amorphous layer may also explain the irregular

nature of the bubbles. An interstitial cluster in a-Si can be thought of as a local variation in density, which, consequently, will produce local variations in elastic moduli giving rise to localised variations to the curvature of the bubbles.

One conclusion which can made unequivocally is that the microtwins do not nucleate exclusively on the gas bubbles, contrary to the model proposed by Revesz *et al*. These previous studies of the epitaxial re-growth of inert-gas-implanted amorphous Si also indicated the presence of microtwins in the re-crystallised layer. A model was proposed in which large gas bubbles act as nucleation sites for microtwins, with perfect re-growth occurring until interaction with these bubbles. However, the XTEM micrographs produced during the current research show, undeniably, the existence of microtwins in a region where re-crystallisation occurred well before the interface interacted with the He bubbles as shown in Figures 5.6, 5.7 and 5.8.

The elongated nature (bubbles elongated in the direction parallel to the a/c interfaces) and huge increase in size of the bubbles in the annealed sample (indicating increased coalescence of bubbles compared to in samples solely containing He bubbles which have been annealed), leads to the conclusion that the gas has been swept somehow by the interfaces, as for the Xe implanted Si. No mention of this sweeping effect is included in the Revesz model.

Following on from these results, another wafer, implanted with Li to produce a buried a-layer, was implanted with a lower He fluence, namely $5x10^{15}$ He ions/cm^2. No bubbles were resolvable by the TEM in the as-implanted sample, however a similar structure to that previously observed was observed in the re-grown layer, again after a bulk anneal under vacuum at 600°C for 30mins. In the bright field micrograph of Figure 5.10a, misshapen bubbles surrounded by a dark contrast are observed. The diffraction pattern of this area contained the extra spots we now associate with microtwins. Indeed, a dark field image produced using one of these extra spots, shown in Figure 5.10b, yields the existence of microtwins in this sample. In this case however, the microtwins are only

observed on and about 100 nm in front of the bubble distribution.

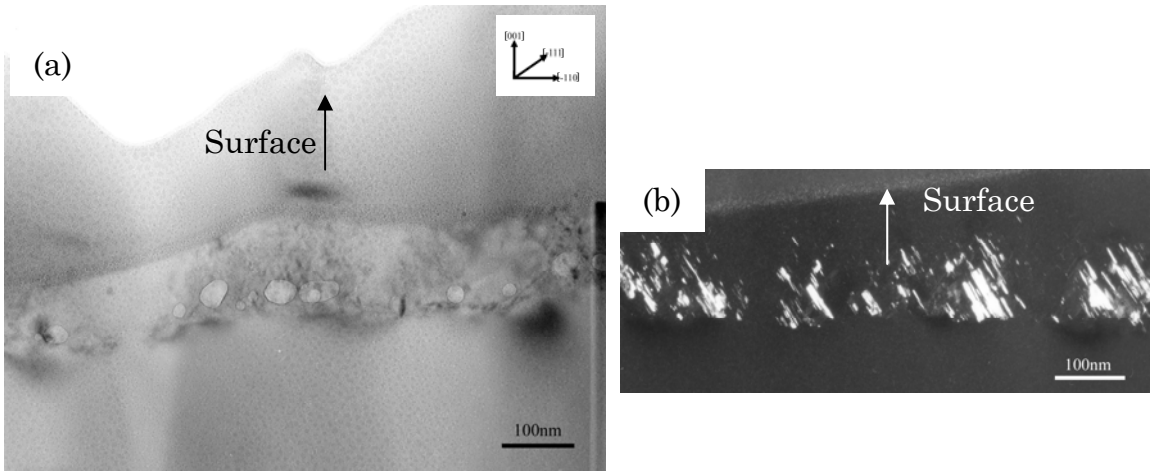

Figure 5.10: *(a) is a [110] cross-section, bright field TEM micrograph of the resultant defect structure in Si following implantation with 7x10^{15} Li ion/cm^2 at LN$_2$, post-implantation with 5x10^{15} He ions/cm^2 at RT and annealing at 600°C for 30mins. Kinematical diffraction condition; underfocus. (b) shows a dark field image produced using one of the extra spots which were visible in the diffraction pattern.*

Even though bubbles are not observed in the as-implanted sample, microtwins are still produced, again at a depth where the interstitial concentration due to the He implantation is a maximum.

The line of bubbles shown in Figure 5.10 appears to be bent. It is believed that this is due to the irregular re-growth of the amorphous layer as was observed during *in-situ* experiments, the results of which are presented later in this chapter.

5.2.4 Re-crystallisation without the influence of excess interstitials

In order to investigate whether a boundary created by large defects such as a bubble or cavity, or an excess of interstitials, leads to the stacking sequence mistakes necessary for microtwin formation, further experiments were

devised. The experimental procedure and results are described in the following section.

5.2.4.1 Experiment

A wafer of [100], n-type single-crystal Si was implanted with 80 keV He to a fluence of $2.5x10^{16}$ ions/cm^2 at RT. The sample was then annealed in a conventional furnace at 1000ºC for an hour in order to remove the He to produce cavities and to recover the interstitial damage produced during implantation. This sample was then implanted with $1.5x10^{17}$ Li ions/cm^2 at cryogenic temperatures and an energy of 150keV. This resulted in a buried amorphous layer with cavities in the centre, without the excess interstitials assumed in the previous samples. Finally, the layer was re-crystallised with a furnace anneal of 600ºC for 30mins.

5.2.4.1 Results

Figure 5.11a shows the wafer following the procedures described above. The cavities are faceted, with average diameter about 60nm. Figure 5.11b is a bright field image after the layer has been re-grown with Figure 5.11c being the corresponding weak-beam dark-field image. As these last two images show, microtwins are not observed in this sample, instead a dense band of non-crystallographic defects are produced centred on the cavity distribution.

These results indicate that the microtwins are not formed when the a/c interface comes into contact with the cavities as was shown in the previous results. A reasonable conclusion therefore is that microtwin lamellae nucleation requires a critical density of interstitials within the amorphous layer. Where the excess interstitials produced after He implantation are removed prior to the production of the a-layer no microtwins are formed.

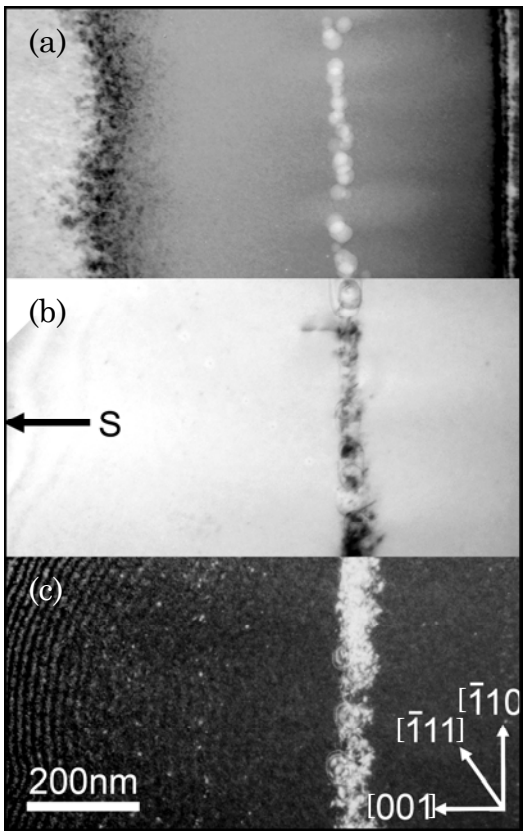

Figure 5.11: *All images are [110] cross-sections.*

Image a: Bright field image showing sample containing cavities which has been re-implanted with 1.5x10^{17} Li ions/cm^2.

Image b: Bright field image following 600°C anneal for 30 minutes.

Image c: Weak beam dark field image corresponding to image b.

S indicates the surface

5.2.5 In-situ investigations

The results obtained after annealing samples in the bulk, allowed for an investigation of the situation after complete re-crystallisation had occurred. From this it has been deduced that microtwin formation is in fact a consequence of the excess interstitial concentration, produced after He implantation, and not due to the presence of large bubbles in the a-layer. The final structure contained large, elongated bubbles, extended in a plane parallel to the surface and original a/c interfaces. This leads to the conclusion that, as for the Xe implanted samples detailed in Chapter 4, the He was swept by the interfaces during SPEG. These results however do not give an insight into the processes through which the gas is pushed by the interfaces. One possibility is that in a-Si, the thermal mobility of bubbles via a surface diffusion mechanism, is greater than in c-Si and therefore bubbles are mobile at a lower temperature in a-Si to in c-Si. One can therefore envisage a situation where the bubbles, mobile in the a-Si, would not cross the a/c interface into c-Si where they would not be mobile, hence being apparently swept

by the interface during re-crystallisation by a ratchet type of process.
In order to achieve a more detailed understanding of the excess interstitial induced microtwin nucleation, and forced gas bubble migration due to c/a interface interaction, two *in-situ* XTEM experiments were devised. The intention of the first experiment was to simply observe the motion of the interfaces during SPEG. The second was designed to simultaneously observe bubble motion in the a-layer at SPEG temperatures, interaction of the bubbles with the a/c interfaces, and the nucleation of microtwins. Details of the experiments and the results obtained are given below.

5.2.5.1 *In-situ* XTEM experiment 1 – re-crystallisation of a buried a-layer

A sample which had been subjected to Li implantation at cryogenic temperatures, and subsequent implantation with 2.5×10^{16} He ions/cm^2 at RT as described previously, was prepared for XTEM analysis and attached to a molybdenum support grid.

During this experiment it was noted that the two a/c interfaces did not start moving at the same time. In fact, the interface nearest the surface moves initially, then, once about half of the amorphous layer has been re-crystallised, the deeper a/c interface begins to move. This is the inverse of what has been found to occur in the bulk annealed samples where the peak of the bubble distribution following re-crystallisation indicates that they were swept towards the surface. Other studies using results obtained from bulk annealed samples have also reported that the back a/c interface moves before the interface closest to the surface. [7] A possible explanation of this reversal may be stress relief in the thin TEM samples.

A bright field XTEM image is given in Figure 5.12. The most striking feature of this image is the dark contrast which exists in a band of width corresponding to that of the original a-layer. Closer analysis of this area using selected area diffraction (SAD), produced a diffraction pattern containing extra spots, corresponding to the presence of microtwins. This pattern was produced

over the entire width of dark contrast. This is in contrast with previous results where microtwins were only formed on and in front of the initial bubble distribution.

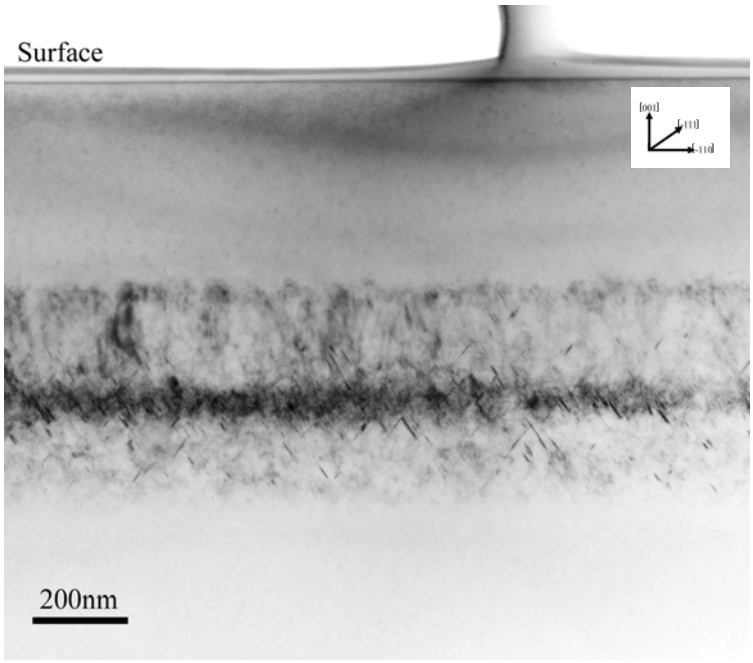

Figure 5.12: *[110] bright field image of sample following in-situ annealing experiment. Sample was tilted slightly off the Bragg condition.*

Another feature of this sample is the absence of large elongated bubbles. Of course, an *in-situ* annealing experiment provides a rather different environment to that which exists in bulk annealed samples. In particular there are extra surfaces to consider, which can act as sinks or sources for defects. Helium that is free to diffuse, either atomistically or as a bubble, will be able to escape through these extra surfaces during annealing whereas in a bulk specimen they may be confined to the buried amorphous layer. Another consideration is the effect that the specimen preparation method used has on the material. Energetic Ar ions are used to sputter the Si samples until they are electron transparent. It is known that a small quantity of the Ar is retained in the samples' surface. It has also been found that small, He filled surface bubbles appear to migrate further into the sample during Ar bombardment [8]. If the concentration of interstitials associated with the Ar reaches a maximum, as described by Narayan

[9], then this may serve as an explanation for the observed anomalous microtwin distribution.

5.2.5.2 *In-situ* XTEM experiment 2 – bubble mobility, sweeping of gas by the c/a interfaces and microtwin nucleation during SPEG

5.2.5.3 Bubble mobility

One hypothesis is that the bubbles are swept by the c/a interfaces because their thermal mobility is higher in a-Si compared to c-Si. In c-Si, He bubbles migrate and coalesce during thermal treatments of upwards of 650˚C due to the diffusion of atoms on the internal surface of the bubbles. In the temperature range where SPEG initiates, 550 – 600˚C, TEM resolvable He bubbles are not expected to be mobile. The purpose of the first part of this experiment was to observe the bubbles in the a-layer in this temperature range. Subsequent processing of the captured video, where the frame rate is increased, will allow for the observation of bubble motion (which is slow in real time), if any should occur.

5.2.5.4 Microtwin Formation

Figure 5.13 depicts 6 <110> cross-sectional, bright field TEM images, which have been captured from the video during analysis. The temperature of the sample during this stage of the experiment was 620°C, and the frames were taken 200s apart. The growth of a microtwin is observed to occur at the interface.

Figure 5.14 shows a high-resolution phase contrast image of microtwins produced during this experiment. The arrow indicates the region where nucleation occurred. It can be seen from this image that the microtwin nucleated in a very small volume of crystal and that its width increased as it grew. This is indicative of all the microtwins imaged at high-resolution.

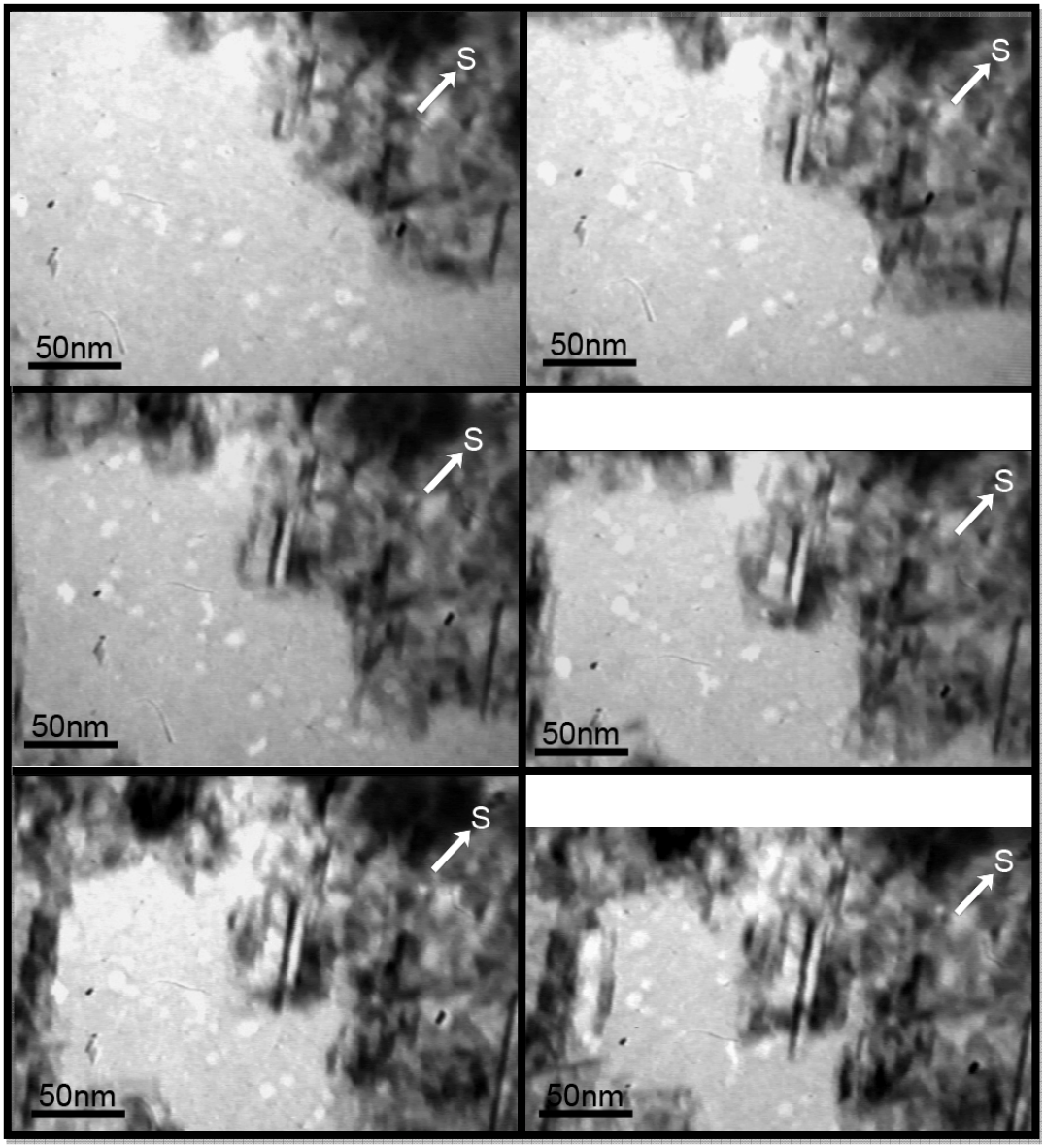

Figure 5.13: *6 screen shots, taken 200 seconds apart, showing the formation of a microtwin. No bubbles are present at the nucleation site, however, contrast which is ascribed to non-crystallographic defects, is clearly visible.*

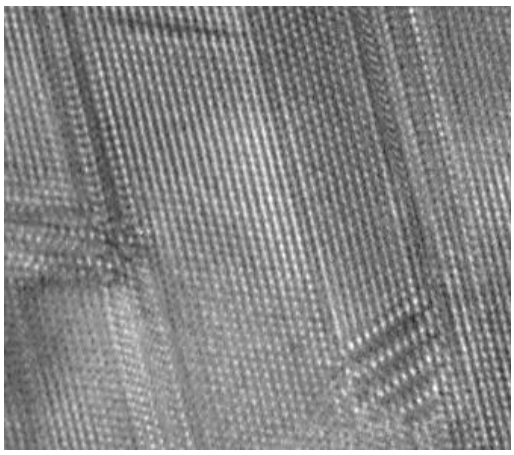

Figure 5.14: *High-resolution phase contrast image of microtwins. The change in direction of the 111 planes is clearly visible.*

Molecular Dynamics simulations conducted by Dr Laurent Pizzagali

The results presented so far indicate that microtwin nucleation under these conditions occurs due to an excess of interstitials, produced by He implantation. In order to confirm this theory, molecular dynamics (MD) simulations of the SPEG were carried out by Dr Laurent Pizzagali. In these simulations, Si was described with the EDIP potential [10,11] which has been previously used in the investigation of SPEG in Si and which gives good agreement with experiments. [12] The simulations were performed in a similar way to Bernstein *et al* [12] in that the initial systems, with dimensions $5a_o$ (X=[100]), $5a_o$ (Y=[010]), and $10a_o$ (Z=[001]), were formed by joining a crystalline slab $5a_o$ x $5a_o$ x $4a_o$ with a disordered structure $5a_o$ x $5a_o$ x $6a_o$ along the Z direction. Periodic boundary conditions were applied only along X and Y, leaving two free surfaces and a single a/c interface. In order to investigate whether the presence of defects would induce microtwin formation four models of disordered structures were built, with density increased by 5% and 10% compared to c-Si. The initial samples were created using liquid Si with the same density as c-Si which was slowly quenched. These samples showed the characteristic features of a-Si. In model I, interstitials were randomly introduced into the disordered structures and then relaxed. In model II, small clusters containing 10 interstitials were randomly introduced and then the structure was relaxed. Model III was produced in a similar way to model II with the exception that several annealing and quenching cycles were

performed in order to optimize the relaxation of the interstitial clusters. Model IV was produced by quenching liquid Si prepared with the desired density. For each model, 6 different samples were built giving a total of 24 samples for a given density. Simulations of SPEG were carried out using MD runs of 10ns (10^7 time steps) and a constant temperature of 1100K obtained by velocity rescaling, followed by a final relaxation.

In almost all of the simulations describing the SPEG process for a-Si with the same density as c-Si, complete and perfect recrystallisation of the disordered structure was achieved. In one of the simulations stacking faults were found to form during the process. The simulations describing the a-Si systems with increasing interstitial densities (Models I to IV) gave results showing that many of the systems recrystallised with the extra interstitial atoms having migrated towards the surface. However, in several of the systems, either incomplete recrystallisation or formation of stacking faults or grain boundaries was obtained. These results have been classified into three categories:

(i) complete re-crystallisation with the formation of one or several stacking faults;
(ii) stacking faults bordering a small disordered region; and
(iii) amorphous nuclei leading to the formation of a grain boundary, with a possible change of growth orientation and the presence of stacking faults.

The result classified in category (iii) is given in Figure 5.15.

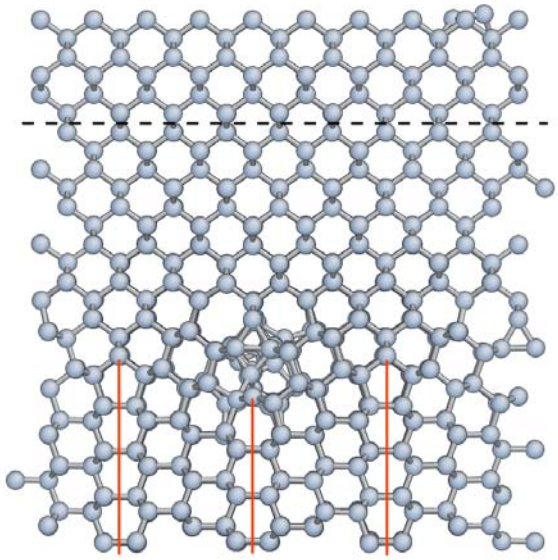

Figure 5.15: *Ball-stick representation, projected on (110), of a selected final configuration after SPEG (edges are not shown for clarity). Recrystallization occured from top to bottom, starting from the initial c-a interface (dashed line), with the formation of a grain boundary and a change of growth direction from <110> to <112>. Stacking faults, present in the <112> region, are also marked in the picture [14].*

It was found that, overall, the occurrence of such events, categorised (i), (ii) and (iii) above, increases with the density of the disordered structure, with the number of events for 10% being twice that for 5%. Few differences were found amongst the different models, although there appeared to be slightly more events in the case of models I and IV than for models II and III. These observations suggest that the probability of formation of structural defects increases with the concentration of interstitials in the initial amorphous material. It is thought that interstitials or interstitial clusters form locally metastable structures, which then act as nuclei for defects which form during re-crystallisation, or alternatively that they increase the migrations barrier for Si atoms in a-Si, thus hindering re-crystallisation.

The formation of stacking faults or thin grain boundaries during SPEG simulations is associated with a change of growth orientation. Microtwins are achieved during this process and are shown as a perfect crystal slab

bordered by two stacking faults with similar orientations. These calculations have therefore provided further evidence to support the theory that microtwins require interstitials at the a/c interface in order to nucleate.

5.2.5.5 Sweeping of bubbles by the a/c interfaces

The final part of this experiment was intended to observe processes occurring at an a/c interface when a He filled bubble comes into contact with it during SPEG. Figure 5.16 show <110> cross-sectional bright field TEM images of this situation. The temperature of the sample was again measured to be 600°C, with the frames taken 70s apart. The imaging conditions were chosen in order to observe the interface and bubbles simultaneously and thus are not ideal for either type of defect. These images clearly show a bubble apparently being pushed by the advancing interface, whilst those surrounding it and not in contact with the interface remain stationary. During the period illustrated, the bubble has been pushed 10nm by the advancing interface.

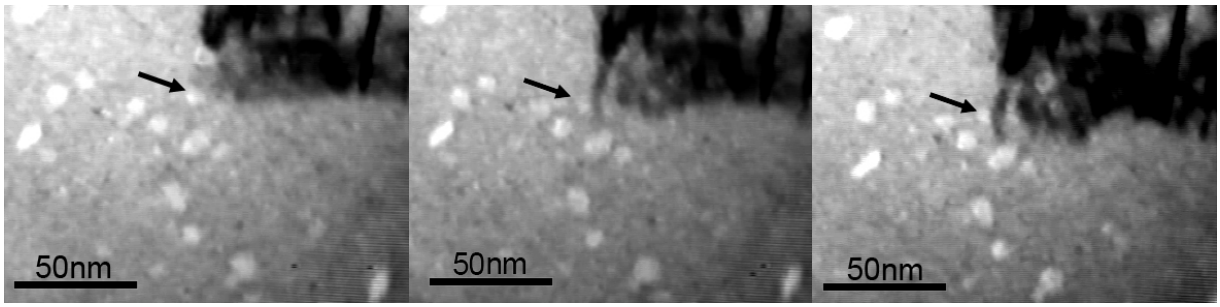

Figure 5.16: *3 screen shots taken 70 seconds apart to show the effect of interaction between an a/c interface and He bubble. The bubble can be seen to be pushed by the interface.*

Figure 5.17 shows screen shots from a separate experiment [13] where, at the temperature where bubbles in c-Si are not mobile, bubbles in the a-Si can be seen to be moving. Further analysis of the video showed that the bubbles were confined by the a/c interfaces in the a-Si. The temperature during this period of the experiments was kept constant at approximately 620°C. By using a series of video frames at 5 second intervals, measurements of the projected 2-D movement of a small number of bubbles with radii in the range of approximately 4-6 nm were made. From these measurements, the bubbles were found

to have velocities along their 2-D projected trajectories of between 2.5 and 1.5nm/s.

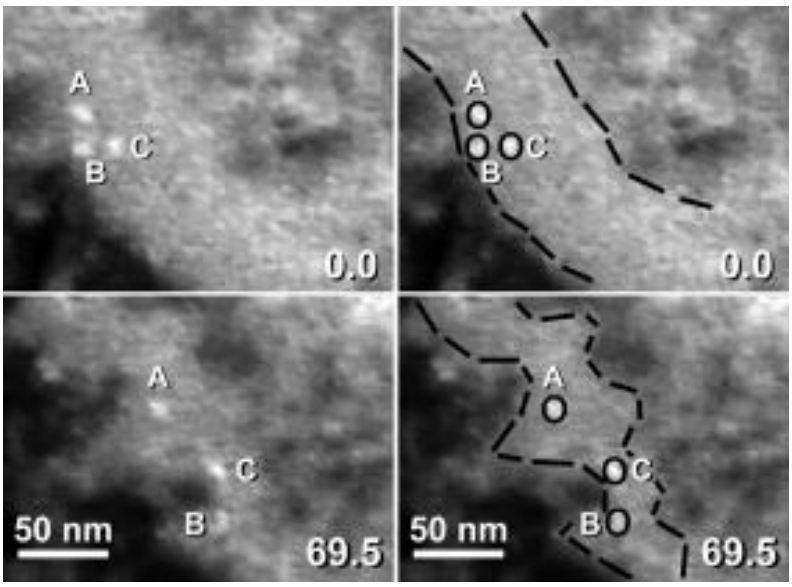

Figure 5.17: *Screen shots clearly showing bubble mobility in the a-layer*

As has already been described in Chapter 2, bubble mobility generally occurs due to surface migration processes, where substrate atoms at the surface of the bubble move around the bubble's surface altering the bubble's centre of mass and resulting in Brownian motion of the bubble. Smaller bubbles move more rapidly than larger bubbles during this process. The process of re-crystallisation by SPEG has also been described in detail in Chapter 2. For SPEG to occur, atoms at the a/c interface must be mobile such that they are able to move to a lattice position in the crystal. The observed bubble motion in amorphous silicon implies that surface diffusion within bubbles in amorphous silicon takes place at the temperature at which SPEG occurs, which is a significantly lower temperature than surface diffusion in c-Si. This is a new and potentially important observation as surface diffusion on clean a-Si has not been measured as such surfaces (even in UHV) are normally hydrogenated.

In order to determine whether there is an enhanced surface diffusion within bubbles in amorphous layers, the value for the activation energy for surface diffusion was calculated. This was done by using an expression, derived

in a previous paper [15], for cavity velocity (v_c), along the projected path, observed from successive video frames recorded with a frame rate of $1/\lambda t$, given by:

$$v_c = 2(\lambda/N)\sqrt{\frac{\lambda_0(\exp(-E_s/kT))}{t}} \qquad [5.1]$$

where λ is the atomic jump distance, N is the number of vacancies in the cavity, E_s is the activation energy for surface diffusion, λ_0 is the jump attempt rate, T is temperature and *k* is Boltzmann's constant.

By assuming that $\lambda_0 = 10^{13}$ s^{-1} and using the values previously stated for bubble size and velocity, the activation energy for surface diffusion is calculate to be 0.35 – 0.45 eV. Measurements of the diffusion process in c-Si have determined an activation energy of 1.3 eV [16]. This results, therefore, leads to the conclusion that small bubbles in a-Si are mobile at temperatures lower than in c-Si, as observed.

5.2.6 Conclusion

During the course of this investigation, it was shown using TEM analysis that $1.5x10^{17}$ Li ions/cm^2, implanted at cryogenic temperatures with 150keV leads to the formation of a buried a-layer in Si. A conventional furnace anneal of 400°C for 30mins resulted in the removal of point defects produced in front of the layer up to the surface, as well as a sharpening of both interfaces. In both samples, small crystallites were observed in the a-layer near the front interface. An anneal of 600°C in a conventional furnace anneal under vacuum resulted in the complete recovery of these a-layers, with the only remaining defects being interstitial defect clusters, indicating the initial positions of the a/c interfaces and where the interfaces combined at the end of re-crystallisation.

Implantation of both samples with 80 keV He to a fluence of $2.5x10^{16}$ ions/cm^2 at RT resulted in the production of a band of irregular shaped bubbles,

approximately 10nm in diameter, in the centre of the a-layer. Furnace annealing of this sample under vacuum, at 600°C for 30mins resulted in the SPEG of the layer. The bubbles were apparently pushed by the a/c interfaces. This occurred at a temperature below that which is required for bubble mobility in c-Si, indicating that bubbles in a-Si are mobile at a lower temperatures compared to in c-Si. This enhanced mobility results in the bubbles moving into the amorphous layer upon coming into contact with the a/c interfaces via a ratchet effect. Results from *in-situ* experiments showed bubble motion (of bubbles of approximately 2nm in diameter) in the amorphous layer at 620°C, which is below the temperature required for bubble mobility of bubbles of this size in c-Si. This pushing effect resulted in the formation of large bubbles averaging about 100nm in diameter and slightly elongated in the [001] direction, residing just in front of the original distribution. Microtwins were formed during SPEG, situated on and in front of the original bubble distribution, finishing at the original position of the front a/c interface. Microtwin formation in this case has been concluded to be caused by the excess interstitials produced during He implantation, which TRIM calculations indicate are distributed in the region containing microtwins. An increase in the local concentration of these interstitials at the a/c interface may be sufficient to cause stacking sequence mistakes indicative of microtwin formation. This theory was further corroborated by *in-situ* TEM results which showed an increase in density of contrast attributed to point defects immediately before nucleation of a microtwin occurred, and by MD simulations. In addition to this, TEM images of experiments where no excess interstitials existed inside the layer did not yield the existence of microtwins.

5.3 References

1. Revesz, P., Wittmer, M., Roth, J., and Mayer, J.W. *Epitaxial Regrowth of Ar-Implanted Amorphous Silicon.* Journal of Applied Physics, 1978. **49**(10): p.5199-5206.
2. Kennedy, E.F., Csepregi, L., Mayer, J.W., and Sigmon, T.W. *Influence of O-16, C-12, N-14, and Noble-Gases on Crystallization of Amorphous Si Layers.* Journal of Applied Physics, 1977. **48**(10): p.4241-4246.
3. Cullis, A.G., Seidel, T.E., and Meek, R.L. *Comparative-Study of Annealed Neon-Ion, Argon-Ion, and Krypton-Ion Implantation Damage in Silicon.* Journal of Applied Physics, 1978. **49**(10): p.5188-5198.
4. Wittmer, M., Roth, J., Revesz, P., and Mayer, J.W. *Epitaxial Regrowth of Ne-Implanted and Kr-Implanted Amorphous Silicon.* Journal of Applied Physics, 1978. **49**(10): p.5207-5212.
5. Oliviero, E., *Personal Communication*. 2005.
6. Beaufort, M.F., Donnelly, S.E., Rousselet, S., David, M.L., and Barbot, J.F. *Extended-type defects created by high temperature helium implantation into silicon.* Nuclear Instruments and Methods in Physics Research Section B: Beam Interactions with Materials and Atoms, 2006. **242**(1-2): p.565-567.
7. Giewont, K., Ashok, S., and Mogro-Campero, A. *Thermal anneal recovery of silicon surface barriers from argon ion implantation damage.* Thin Solid Films, 1986. **142**(1): p.13-20.
8. Gandy, A.S., Donnelly, S.E., Beaufort, M.F., Vishnyakov, V.M., and Barbot, J.F. *The effect of ion-beam specimen preparation techniques on vacancy-type defects in silicon.* Nuclear Instruments and Methods in Physics Research Section B: Beam Interactions with Materials and Atoms, 2006. **242**(1-2): p.610-613.
9. Narayan, J. *Interface Structures during Solid-Phase-Epitaxial Growth in Ion-Implanted Semiconductors and a Crystallization Model.* Journal of Applied Physics, 1982. **53**(12): p.8607-8614.

10. M. Z. Bazant, E. Kaxiras, and Justo, J.F. *Environment-dependent interatomic potential for bulk silicon.* Physical Review B, 1997. **56**: p.8542.
11. J. F. Justo, M. Z. Bazant, E. Kaxiras, V. V. Bulatov, and S. Yip *Interatomic potential for silicon defects and disordered phases.* Physical Review B, 1998. **58**: p.2539.
12. N. Bernstein, M. J. Aziz, and Kaxiras, E. *Atomistic simulations of solid-phase epitaxial growth in silicon.* Physical Review B, 2000. **61**: p.6696.
13. Donnelly, S.E. 2008.
14. Beaufort, M.F, Pizzagalli, L, Oliviero. E, Gandy, A.S, Eyidi, D., Donnelly, S.E., Journal of Applied Physics, **104** 094905 (2008)
15. Donnelly, S.E, Vishnyakov, V.M, Birtcher, R.C, and Carter, G, Nucl. Instrum. & Meth. in Phys. Res. B, 2001,**132**
16. Swartzentruber, B.S., and Schacht, M., Surface Science 1995, **322** p83

Chapter 6

Summary and Conclusions

6.1 Summary

High temperature (350°C) implantations of Xe into Si were studied using XTEM, and the results of the experiments were given in Section 4 of this report. Samples implanted with various fluences, $5x10^{15}$, $1x10^{16}$, $2x10^{16}$ and $5x10^{16}$ Xe ions/cm^2, and subjected to different annealing temperatures (as-implanted, 400°C, 600°C and 800°C) were investigated. Results from the annealing experiments showed that the Xe gas was apparently swept by both crystalline/amorphous interfaces during re-crystallisation of the buried amorphous layer that was formed by Xe implantation. In order to investigate further this sweeping effect, another set of experiments was devised, the results of which are given in Section 5 of this report. These experiments consisted of producing a buried a-layer in Si by implanting Li at LN_2 temperature and annealing it at 400°C for 30 minutes to recover the damage produced in front of the amorphous layer extending to the surface. This layer exhibited relatively sharp, defect free c/a interfaces with. He was then implanted at room temperature, producing a linear band of bubbles in the centre of the layer. Both *in-situ* annealing and bulk annealing experiments confirmed that the He gas was swept by the moving c/a interfaces. The main findings from both these sets of experiments are detailed below.

6.1.1 Characterisation of Xe Implantation damage in Si

Implantation of Xe ions into Si at 350°C and at fluences of $1x10^{16}$ Xe ions/cm^2 or greater resulted in amorphisation of the samples. The ions were implanted with 250keV, resulting in the production of buried amorphous layers. The width of the layer increased with increasing fluence. In all cases, the layer contained defects which, using a through-focal series, were determined to be cavities. The c/a interfaces were irregular with many undulations, in contrast to interfaces of a-layers produced during room temperature implantations. This difference may be attributed to strain fields of the bubbles present in the high implantation temperature regime or to dynamical annealing effects.

In the amorphised samples annealed at 600°C, re-crystallisation of the layers was achieved and the bubble layers were much smaller than the width of the original a-layers. The bubbles were highly elongated along a direction parallel to

the original c/a interfaces, and were centred on a line corresponding to the centre of the original a-layers. These results suggest that the Xe bubbles were swept by the c/a interfaces during re-crystallisation. After annealing the samples at 800°C, the elongated bubbles appeared to have coalesced into relatively large circular bubbles.

Xe bubbles were found to form along the entire Xe distribution profile (in front of, inside and behind the a-layers), indicating that the critical local Xe concentration required for bubble formation is much less than for He in Si, and that radiation-enhanced diffusion may allow the local concentration required to be achieved over a wider area. Bubbles were produced in annealed samples even though they were not formed in the as-implanted samples, due to the retention of Xe in Si.

In all the samples studied, {113} rod-like defects were formed in a region corresponding to the end of range of the Xe ion-track. In addition, Xe precipitates were also formed in all samples and microtwins appeared to have been formed in the amorphised and annealed samples.

6.1.2 SPEG of He implanted buried amorphous layers in Si

Implantation of 2.5×10^{16} He ions/cm^2 into a buried a-layer, produced during 1.5×10^{7} Li ions/cm^2, resulted in a band of approximately 10nm diameter, irregular shaped bubbles, located at the centre of the a-layer. The sample was annealed at 600°C in order to re-crystallise the layer. At this temperature, the migration of He bubbles in c-Si does not occur. Results from *in-situ* TEM experiments showed the bubbles in a-Si are in fact mobile at the temperature where SPEG occurs, and that are confined to the a-layer during re-crystallisation due to a ratchet effect. The resultant bubble structures, from samples annealed in the bulk, were similar to those found following 600°C anneals of the Xe implanted samples, in that they were larger than the bubbles in the as-implanted sample and elongated along a direction parallel to the original a/c interfaces. These bubbles were situated just in front of the original bubble distribution.

Microtwins were formed during SPEG and were situated on and in front of the original bubble distribution. The microtwin distribution finished at the original position of the front c/a interface. Results from *in-situ* TEM experiments showed that the microtwins did not form on bubbles, as was proposed by Revesz *et al*. TRIM calculations indicated an excess of interstitials in the region containing the microtwins, and TEM images of experiments where there was no interstitial excess inside the a-layer did not show the existence of microtwins. These results lead to the conclusion that it is an excess of interstitials which gives rise to the formation of microtwins during SPEG of a-layers in Si. The excess interstitials may cause stacking sequence mistakes which result in microtwin formation.

6.2 Conclusions

The results from both sets of experiments show that inert gas bubbles can be formed inside buried amorphous layers, and that they are mobile at the temperatures when SPEG of the a-layers occurs. Microtwins are formed in an area corresponding to an area of excess interstitials, and do not appear to form on bubbles as has been proposed in previous studies. It has been deduced, using the results in this report, that the interstitial excess results in stacking sequence mistakes of the a-layer during SPEG. These stacking sequence mistakes have been reported by other authors (Drosd and Washburn) as being the precursor to microtwin formation.

The defect structures in Xe implanted Si have been shown to be different to those in Li and He implanted Si. Bubbles are formed in the Xe samples along the entirety of the Xe distribution, and bubbles are formed in the annealed samples even though they were not formed in the as-implanted samples. It is known that He bubbles must be formed in the as-implanted samples for them to be present in annealed samples. Further, He bubbles are never formed across the whole of the He distribution, as the critical He concentration required is not achieved along the entirety of the distribution. Solid Xe precipitates and {311} defects were only formed in the Xe implanted samples.

6.3 Further Work

The effect of Li during SPEG is unknown. Therefore, proposed further work would be to produce a surface a-layer by implanting with Si, then carry out the same experiments involving He in order to investigate whether the Li is playing a role in the enhanced mobility of He in a-Si.